

BOSTON UNIVERSITY
COLLEGE OF ENGINEERING

Dissertation

**LONGITUDINAL MONITORING OF CHEMOTHERAPY RESPONSE IN
PRECLINICAL ONCOLOGY MODELS USING SPATIAL FREQUENCY
DOMAIN IMAGING (SFDI)**

by

SYEDA MAHABUBA TABASSUM

B.S., University of Dhaka, 2010
M.S., University of Dhaka, 2012
M.S., Boston University, 2017

Submitted in partial fulfillment of the
requirements for the degree of
Doctor of Philosophy

2020

Approved by

First Reader

Darren Roblyer, Ph.D.
Associate Professor of Biomedical Engineering

Second Reader

Irving J. Bigio, Ph.D.
Professor of Biomedical Engineering
Professor of Electrical and Computer Engineering
Professor of Physics
Professor of Medicine

Third Reader

M. Selim Ünlü, Ph.D.
Professor of Electrical and Computer Engineering
Professor of Biomedical Engineering
Professor of Materials Science and Engineering
Professor of Physics

Fourth Reader

David J. Waxman, Ph.D.
Professor of Biology
Professor of Medicine
Professor of Biomedical Engineering

Fifth Reader

Joyce Y. Wong, Ph.D.
Professor of Biomedical Engineering
Professor of Materials Science and Engineering

Sixth Reader

Michelle Sander, Ph.D.
Assistant Professor of Electrical and Computer Engineering
Assistant Professor of Materials Science and Engineering

DEDICATION

I would like to dedicate this work to my father Syed Raquibul Hussain and father-in-law
Habibur Rahman Khan.

ACKNOWLEDGMENTS

I would like to acknowledge my advisor, Darren Roblyer, and co-advisor Irving Bigio for their guidance and support throughout this journey. I would like to acknowledge all members of the BOTLab, past and present, especially those who have had direct contributions to this body of research. I am also grateful to my committee members, Selim Unlu, David Waxman, Joyce Wong, and Michelle Sander for guiding this project and me.

I am grateful for funding from the American Cancer Society, Department of Defense, and Boston University Cross-Disciplinary Training in nanotechnology for Cancer. I am also grateful for the travel awards from the Department of Electrical and Computer Engineering and the Boston University Photonics Center.

**LONGITUDINAL MONITORING OF CHEMOTHERAPY RESPONSE IN
PRECLINICAL ONCOLOGY MODELS USING SPATIAL FREQUENCY**

DOMAIN IMAGING (SFDI)

SYEDA MAHABUBA TABASSUM

Boston University College of Engineering, 2020

Major Professor: Darren Roblyer, Ph.D., Associate Professor of Biomedical
Engineering

ABSTRACT

Methods for frequent non-invasive surveillance of the *in-vivo* tumor state may assist in detecting whether a patient is responding or developing resistance at an early stage of treatment. This would allow physicians to adapt and personalize treatment strategies in real-time. Multiple studies have demonstrated that clinical diffuse optical imaging (DOI), which can provide structural and hemodynamic profile of tumor, can reveal treatment induced changes that correlate strongly with patient response determined by pathology. While encouraging, there are many unknowns as to how DOI optical markers manifest for different treatment regimens and dosing. Additionally, a deeper understanding of the underlying cellular and molecular changes that contribute to DOI markers is needed to provide a mechanistic context to these clinical observations. This project addresses these issues at the preclinical level with Spatial Frequency Domain Imaging (SFDI). SFDI is a wide-field and non-invasive DOI modality that provides the same optical and hemodynamic information as the clinical tools and is more suitable for preclinical imaging, and so is the right tool for such exploratory study. To this end, the work presented in this dissertation was focused on establishing SFDI as a new preclinical monitoring tool for

cancer. For the first time, the feasibility of using SFDI for frequent longitudinal monitoring of chemotherapy and targeted therapy efficacy in small animal oncology models was established. The SFDI optical property extraction accuracy was then improved in subcutaneous tumors by the development of a new two-layer Monte Carlo based inversion model. SFDI optical and functional metrics were then validated in the context of cellular and molecular correlates using immunohistochemistry. The treatment prediction ability of SFDI was also compared to simple tumor volume measurements in multiple tumor models. Finally, a custom-made LED-based SFDI system was developed to measure tissue water content in addition to hemodynamic features. Overall, this body of work helps to establish SFDI in the field of preclinical cancer treatment monitoring. Knowledge gained from this work may assist in the clinical translation of DOI tools as important feedback methods in the applications of treatment monitoring, drug testing, and personalization of treatment strategies.

TABLE OF CONTENTS

DEDICATION	iv
ACKNOWLEDGMENTS	v
ABSTRACT	vi
TABLE OF CONTENTS.....	viii
LIST OF TABLES	xiv
LIST OF FIGURES	xv
LIST OF ABBREVIATIONS.....	xxii
CHAPTER ONE: Background and Significance.....	1
1.1 Chemotherapy response monitoring	1
1.1.1 Chemotherapy: an important treatment option for cancer	1
1.1.2 Importance of early and long-term monitoring of chemotherapy response....	2
1.2 Current methods are inadequate for early and long-term monitoring.....	3
1.2.1 Potential of Diffuse Optical Imaging for therapy monitoring	4
1.2.2 Diffuse Optical Imaging (DOI).....	4
1.2.3 Clinical DOI tools for monitoring treatment response	5
1.2.4 Spatial Frequency Domain Imaging (SFDI): A potential pre-clinical chemotherapy monitoring tool.....	6
1.3 Goal of this dissertation.....	7

CHAPTER TWO: Feasibility of Spatial Frequency Domain Imaging (SFDI) for optically characterizing a preclinical oncology model	8
2.1 Introduction.....	8
2.2 Materials and methods.....	9
2.2.1 Spatial frequency domain imaging (SFDI): Image acquisition, processing and analysis.....	9
2.2.2 Selection of spatial frequencies	13
2.2.3 Spectral chromophore fitting	14
2.2.4 Average tumor values and intratumor heterogeneity.....	15
2.2.5 Repeatability	16
2.2.6 Mouse tumor xenograft.....	17
2.2.7 Longitudinal monitoring of tumor xenograft.....	19
2.3 Results.....	20
2.3.1 Selection of spatial frequencies	20
2.3.2 Spectral fitting.....	23
2.3.3 Average tumor values and intratumor heterogeneity	24
2.3.4 Repeatability	25
2.3.5 Longitudinal monitoring of tumor xenografts	27
2.4 Discussion.....	30
2.5 Conclusions.....	33
CHAPTER THREE: Two-layer inverse model for improved longitudinal preclinical tumor imaging in the Spatial Frequency Domain Imaging (SFDI)	35

3.1	Introduction.....	35
3.2	Materials and methods	36
3.2.1	Monte Carlo simulations for the generation of LUT-based inverse models..	36
3.2.1.1	Prior work and the implementation of the Gardner method for estimating R _d in the spatial frequency domain.....	36
3.2.1.2	Monte-Carlo simulation parameters for generating homogeneous and two- layer LUTs	39
3.2.1.3	Monte Carlo simulations at Boston University Shared Computer Cluster (SCC).....	41
3.2.2	Two-layer tissue-simulating optical phantoms	42
3.2.3	Longitudinal monitoring of a mouse tumor xenograft during cancer treatment	44
3.3	Results.....	44
3.3.1	Comparison between MC simulation results and LUT inversion algorithms: R _d	44
3.3.2	Comparison between LUT inversion algorithms: optical property extraction.....	48
3.3.3	The two-layer LUT improves the accuracy of tumor layer optical property extractions using SFDI.....	49
3.3.4	Sensitivity analysis of the two-layer LUT	52

3.3.5	The Gardner two-layer LUT reveals larger therapy-induced optical scattering dynamics and a more hypoxic tumor environment during longitudinal monitoring of tumor xenografts	55
3.4	Discussion	57
3.5	Conclusions	61
CHAPTER FOUR: Early chemotherapy and antiangiogenic response revealed by tumor optical scattering using label-free Spatial Frequency Domain Imaging		
4.1	Introduction	62
4.2	Materials and Methods	64
4.2.1	SFDI data acquisition and processing	64
4.2.2	Cell lines, animals, and treatment details	65
4.2.3	Longitudinal Monitoring with SFDI	66
4.2.4	Immunohistochemistry (IHC)	67
4.2.5	IHC Image Analysis	69
4.2.6	Statistical analysis	72
4.3	Results	73
4.3.1	SFDI reveals dynamic changes in optical scattering in control and treated tumors	73
4.3.2	SFDI scattering parameters correlate with apoptosis and proliferation	78
4.3.3	SFDI hemodynamic parameters correlate with patency and vessel density	82

4.3.4	Optical scattering provides high contrast between treated and control tumors.....	88
4.3.5	The combination of the SFDI scattering parameter a and tumor volume provides a superior early response prediction than either parameter alone	91
4.4	Discussion.....	95
4.5	Conclusions.....	99
CHAPTER FIVE: Early chemotherapy and antiangiogenic response revealed by tumor optical scattering using label-free Spatial Frequency Domain Imaging.....		101
5.1	Introduction.....	101
5.2	Materials and methods	103
5.2.1	IR-SFDI Hardware.....	103
5.2.2	IR-SFDI software: Image acquisition.....	106
5.2.3	IR-SFDI data processing.....	106
5.3	Results.....	107
5.3.1	LED power stability	107
5.3.2	Reflected intensity	109
5.3.3	Demodulation.....	110
5.4.4	Optical properties.....	111
5.4.5	In vitro intralipid testing	111
5.5	Discussion.....	113
5.6	Conclusions.....	114
CHAPTER SIX: Conclusions.....		115

6.1 Discussion.....	115
6.2 Future directions	116
7 BIBLIOGRAPHY.....	118
8 CURRICULUM VITAE.....	130

LIST OF TABLES

Table 2.1. Average SFDI parameters for tumors.....	24
Table 2.2. Intratumor heterogeneity.....	25
Table 2.3. Repeatability (Precision).....	27
Table 3.1: Accuracy of optical property extractions in four two-layer tissue simulating optical phantoms. Each two-layer phantom is designated as tumor 1 - 4.....	52
Table 4.1: Exploratory correlations between SFDI optical parameters and IHC biomarker	79

LIST OF FIGURES

Figure 2.1: A, Mouse imaging set up with OxImager RS SFDI system (Modulim Inc., Irvine, CA). B, SFDI schematic. C, SFDI image processing pipeline using a single representative PC3/2G7 tumor measurements at baseline timepoint. The intensity images (I) and Rd maps are shown at $\lambda=731\text{nm}$ for two spatial frequencies (f_x : 0 mm^{-1} (DC) and 0.1 mm^{-1} (AC)). The absorption and scattering maps are shown at $\lambda=731\text{nm}$. Edge artifact is clear around tumor margin in the absorption image, which is addressed through several automated and/or manual segmentation steps. The oxyhemoglobin image shows HbO_2 map from the final tumor area of interest superimposed on a DC intensity image. The scattering amplitude image shows a map from the final tumor area of interest superimposed on the same DC intensity image. 12

Figure 2.2: A, Schematic of tilt measurement. B, Example of a tilt measurement. 17

Figure 2.3: Two- f_x -LUT's using 10 evenly distributed μ_a values ($0.003 - 0.055\text{ mm}^{-1}$) and 10 evenly distributed μ'_s values ($0.5 - 3\text{ mm}^{-1}$) for DC and 0.025 mm^{-1} (A), DC and 0.1 mm^{-1} (B), DC and 0.2 mm^{-1} (C), DC and 0.5 mm^{-1} (D) f_x pairs. 21

Figure 2.4: Extraction error of μ_a (A) and μ'_s (B), where low $\mu_a = 0.005\text{ mm}^{-1}$, low $\mu'_s = 0.73\text{ mm}^{-1}$, high $\mu_a = 0.035\text{ mm}^{-1}$, and high $\mu'_s = 1.89\text{ mm}^{-1}$ 22

Figure 2.5: Locations of pixels on a DC101-treated tumor at pretreatment (A) and posttreatment (C) timepoints. Broadband fitting of absorption (B) and scattering (D) for pre- and posttreatment timepoints..... 24

Figure 2.6: Absorption (left axis) and scattering (right axis) at 851nm for a representative tumor over 10 stationary (A), 10 move & replace (B), and 11 tilt (C) repeat measurements..... 26

Figure 2.7. μ'_s (left axis) and tumor volume (right axis) over days of DC101 treated tumor (A), μ'_s colormaps overlaid on the DC101 treated planar mouse image at day 0 and day 24 (B), StO_2 (left axis) and tumor volume (right axis) over days for CPA treated tumor (C), StO_2 colormaps overlaid on the CPA treated planar mouse image at day 0 and day 24(D)..... 29

Figure 3.1: A, Schematic of tissue model for the homogeneous case. B, schematic of the tissue model for the two-layer case. C, an example of a custom-made two-layer silicone phantom used to validate the accuracy of the resulting two-layer inverse algorithm..... 42

Figure 3.2: Comparison of Monte Carlo simulation results from the Martinelli homogeneous, the Gardner homogeneous and the Gardner two-layer methods. Diffuse reflectance (R_d) is shown as a function of spatial frequency (f_x) for varying values of l^* at a constant ratio of $\mu'_s/\mu_a = 100$. The Martinelli homogeneous and Gardner homogeneous results are nearly identical, while the introduction of the top (skin) layer introduces significant shifts in R_d that are dependent on f_x and the l^* of the bottom (tumor) layer.....46

Figure 3.3: Comparison of LUT inversion algorithms based on Gardner homogeneous and Gardner two-layer methods. R_d values are shown both in the color dimension and as labeled isolines for the entire range of simulated μ_a and μ'_s values. A and B show optical properties versus DC R_d for the homogeneous and two-layer LUTs respectively. C and D show optical properties versus AC R_d for the homogeneous and two-layer LUTs respectively.....47

Figure 3.4: The impact on optical property extractions of the Gardner two-layer LUT inversion algorithm shown as absolute and % differences compared to the Gardner homogeneous case. A, Absolute and B, percent differences in μ_a extractions. C, Absolute and D, percent difference in μ'_s extractions.....49

Figure 3.5: Comparisons in bottom (tumor) layer optical property extraction errors for the Gardner homogeneous and Gardner two-layer LUT inversion algorithms. Diffuse reflectance measurements of four two-layer tissue simulating optical phantoms were made with SFDI, and both inversion models were used to extract the bottom (tumor) layer optical properties (labeled as tumor 1 - 4). A shows the absolute extraction error compared with the known tumor layer μ_a . B shows the same data but with a zoomed-in y-axis so that small extraction errors can be visualized. C shows absolute errors in tumor layer μ'_s extractions and D shows the same data with a zoomed-in y-axis. Optical properties were measured at 659 nm.....51

Figure 3.6: Results from a sensitivity analysis for the two-layer Gardner LUT inversion algorithm. Errors in tumor layer μ_a and μ'_s extractions are shown for various skin layer property mismatches A-F. In F, the inset image has a zoomed in y-axis. Optical

properties were measured at 659 nm.....	54
Figure 3.7: An example of the Gardner homogeneous and the Gardner two-layer LUT inversion algorithms applied to SFDI data collected during a longitudinal treatment monitoring study of PC3/2G7 prostate tumor xenografts. A, μ'_s extractions from both LUTs are shown during and after DC101-treatment. B, μ'_s colormaps overlaid on DC101-treated planar mouse images at day 0 and day 30. A, B plot mean with standard deviation over tumor ROI. C, StO ₂ values determined using four wavelength optical property extractions from both LUTs for a CPA-treated tumor. D, StO ₂ colormaps overlaid on CPA-treated planar mouse images at day 0 and day 30.	56
Figure 4.1: Representative images of 5 IHC markers and Hoechst in a single PC3/2G7 tumor.....	71
Figure 4.2: Image processing steps shown for a representative PC3/2G7 tumor. A. The tumor cross section was imaged in a snaking pattern with ~10% overlap, and then combined using the ‘stitching’ plugin in FIJI software to produce the stitched image. The dotted region shows a single image and the inset shows a 20X magnification of a small represented area within the tumor, showing individual cells. Green dye indicates top surface and yellow dye indicates bottom surface of the tumor. B. The solid yellow line shows manually segmented region for the tumor cross-section obtained with the help of the ‘Region of Interest (ROI) manager’ tool in FIJI. C. Binarized image obtained with the application of an intensity threshold. The percent of pixels above the threshold and within the ROI was defined as positive staining area (%). This tumor sample was stained for the PCNA marker (proliferation) and resulted a 15% positive	

staining area.....72

Figure 4.3: Tumor volume normalized to baseline for PC3/2G7 tumors for CPA, DC101, and no treatment (control) groups. The shaded region represents the 18 days of treatment period, and the arrows represent treatment cycles. The n values in the legend shows tumor population for each group at baseline, which reduced with days as mice were sacrificed for IHC. Each point represents group mean with standard error (SE). Tumor volume group mean and SE at baseline was $915 \pm 76 \text{ mm}^3$ for control, $805 \pm 86 \text{ mm}^3$, and $871 \pm 116 \text{ mm}^3$ for DC101.....75

Figure 4.4: Longitudinal changes in reduced scattering maps at $\lambda=659 \text{ nm}$ for representative control, CPA, and DC101 treated PC3/2G7 tumors at days 0, 1, 9, 18 and 27..... 76

Figure 4.5: Videos of scattering amplitude a parameter μ'_s ($\lambda=800 \text{ nm}$) for three representative PC3/2G7 tumors. Days, along with study periods, can be observed at the bottom of each image in the video. In the control tumor, tumor volume increased but a decreased continually until the mouse was euthanized on day 27. In contrast, in both CPA and DC101 treated tumors, a continued to increase before these mice were euthanized on day..... 77

Figure 4.6: Longitudinal changes in the SFDI parameters (A, D, G, J) paired with immunohistochemical results (B, E, H, K) at representative days in PC3/2G7 tumors and tumor volume in M. N presents a simple timeline of the study. Data in the bar plots represent mean and standard error in each group. Mann-Whitney Wilcoxon rank sum test was used to test if longitudinal SFDI and IHC metrics were statistically

different from their baseline (day 0) values. Relationships between SFDI and IHC metrics are shown in C, F, I, L using daily group means from the bar plots. The linear best fit and 95% confidence intervals are indicated. The Pearson's ρ (ρ_p) is reported for each plot, along with significance range using both unadjusted and TCH adjusted P values. *Denotes significance range with unadjusted, and † denotes significance range with TCH adjusted P values. Here, *, $P < 0.05$; **, $P < 0.01$; ***, $P < 0.001$; ****, $P < 0.0001$; †, $P < 0.0085$; ††††, $P < 0.0000166$ 80

Figure 4.7: A. The number of tumors in each group at specific timepoints used for plotting and statistical tests with SFDI parameters and TV. Number of tumors from each group used in the Wilcoxon One-Sample Signed Rank test are the same as those shown above except for TV at day 1 for which number of tumors were n(control)=17, n(CPA)=21, n(DC101)=25. The number of tumors from each group used in the classification test are the same as those shown above except for day 1, where the number of tumors were n(control)=17, n(CPA)=21, n(DC101)=25 for both SFDI and TV. B. The number of tumors in each group at specific timepoints used for plotting of IHC markers.....81

Figure 4.8: Longitudinal changes in the SFDI parameters (HbO₂ in A, Hb in C) and immunohistochemical results (Glut-1 in B, Mac-1 in D) at representative days in PC3/2G7 tumors. Data in the bar plots represent mean and standard error in each group. Mann-Whitney Wilcoxon rank sum tests were conducted to test if longitudinal SFDI and IHC metrics were statistically different from their baseline (day 0) values.

The relationships between SFDI and IHC metrics are shown in E, F and G using daily group means from the bar plots. The linear best fit and 95% confidence intervals are indicated. The Pearson's ρ (ρ_p) is reported for each plot, along with significance range using both unadjusted and TCH adjusted P values. *Denotes significance range with unadjusted, and † denotes significance range with TCH adjusted P values. Here, *, $P < 0.05$; **, $P < 0.01$; ***, $P < 0.001$; ****, $P < 0.0001$; †, $P < 0.0085$; ††††, $P < 0.0000166$85

Figure 4.9: Longitudinal changes in the SFDI parameters (a , b) and TV in E0771 tumors in response to CPA and DC101. Data in the bar plots represent group mean along with individual tumor values. C and D both plot tumor volume but in different formats. Arrows represent treatment cycles. Mann-Whitney Wilcoxon rank sum test was used to test if longitudinal SFDI and TV metrics were statistically different from their baseline (day 0) values. *, $P < 0.05$86

Figure 4.10: Pearson's ρ (ρ_p) values for each SFDI and IHC marker. † Denotes significance range using TCH adjusted P values. Here, †, $P < 0.0085$; ††, $P < 0.0017$; †††, $P < 0.000167$; ††††, $P < 0.0000166$87

Figure 4.11: A. Log_2 ratios of CPA treated versus control for TV, a and b . B. Log_2 ratio of DC101 treated versus control. Mean and standard errors are indicated. The Wilcoxon One-Sample Signed Rank Test with a hypothetical median of 0 was used to test if the contrast (Log_2 ratio) was different from 0 at each time point. The resultant P values were adjusted with the TCH procedure to account for multiple comparisons. † denotes

significance range using TCH adjusted P values. Here, †, $P < 0.0104$; ††, $P < 0.002$; †††, $P < 0.0002$89

Figure 4.12: A. Log₂ ratio of CPA treated tumor and control group average for TV and SFDI parameters (HbO₂, Hb, THb and StO₂) over the duration of the study. B. Log₂ ratio of DC101 treated tumor and control group average for TV and SFDI parameters. Mean and standard errors are shown. The Wilcoxon One-Sample Signed Rank Test with a hypothetical median of 0 was conducted to test if the contrast (Log₂ ratio) was different from 0 at each time point. The resultant P values were adjusted with the TCH procedure to account for multiple comparisons. † denotes significance range using TCH adjusted P values. Here, †, $P < 0.0081$; ††, $P < 0.0016$; †††, $P < 0.000158$90

Figure 4.13: Multivariate discriminant classification analysis for discrimination of treated versus control tumors. The AUC of the well performing stand-alone and dual features along with the best performing features are shown in A for CPA and in B for DC101. Corresponding ROC curves for CPA are shown in C for day 1 and in D for day 3. ROC curves for DC101 are shown in E for day 1 and in F for day 3.....94

Figure 4.14: A and B plots actual AUC values up to day 7 and the linear regression lines for CPA and DC101 respectively. In C and D, the TV regression equation from A and B was used to calculate how many days it will take for TV to reach the same AUC value obtained with a (or b) parameter on a certain day, and their difference is plotted on y axis for CPA and DC101 respectively.....95

Figure 5.1: Schematic of the IR-SFDI system. CL: collimating lens, DCM: Dichroic mirror, AL: Achromatic lens, LP: Linear polarizers, M: Mirror, L: Lens, C: Camera.....104

Figure 5.2: Water, lipid, oxyhemoglobin (HbO ₂) and deoxyhemoglobin (Hb) absorption peaks in the VIS-NIR region.....	105
Figure 5.3: IR-SFDI labview code for image acquisition and storage ¹ . The figure measured raw image of a 3D printed phantom in the field of view.....	107
Figure 5.4: Repeat power measurements every 10s for 10 mins for LEDs used in the system.....	108
Figure 5.5: A. Reflected intensity images for the 970nm LED acquired at the 3 phases. B, Line profile plots intensity vs. pixels.....	109
Figure 5.6: Demodulated images at two different wavelengths at two different spatial frequencies.....	110
Figure 5.7: Extracted optical properties (absorption and reduced scattering) for two LEDs, 865 and 970nm, measured from a 20% intralipid phantom.....	111
Figure 5.8: Measured and fits of absorption and scattering LEDs.....	112

LIST OF ABBREVIATIONS

AUC.....	Area under the curve
CC3.....	Cleaved Caspase-3
CCD.....	Charged coupled device
CPA.....	Cyclophosphamide
CT.....	Computed Tomography
DAB.....	3,3'-Diaminobenzidine
DCE-MRI.....	Dynamic Contrast Enhanced MRI
DCS.....	Diffuse Correlation Spectroscopy
DMD.....	Digital Micromirror Device
DOI.....	Diffuse Optical Imaging
DOS.....	Diffuse Optical Spectroscopy
DOSI.....	Diffuse Optical Spectroscopic Imaging
DOT.....	Diffuse Optical Tomography
DRS.....	Diffuse Reflectance Spectroscopy
¹⁸ F-FDG-PET.....	¹⁸ F-Fluorodeoxyglucose-PET
¹⁸ F-FLT-PET.....	¹⁸ F-Fluorothymidine-PET
fMRI.....	functional MRI
FOV.....	Field of View
Hb.....	Hemoglobin
IHC.....	Immunohistochemistry
IR-SFDI.....	Infrared Spatial Frequency Domain Imaging

LED.....	Light Emitting Diode
LUT.....	Look-up-table
MC.....	Monte-Carlo
MLC.....	Modified Lambertian Correction
MRI.....	Magnetic Resonance Imaging
MRS.....	Magnetic Resonance Spectroscopy
NAC.....	Neoadjuvant chemotherapy
NIR.....	Near-infrared
OP.....	Optical Property
pCR.....	Pathological Complete Response
PET-CT.....	Positron Emission Tomography
R_d	Diffuse Reflectance
ROC.....	Receiver Operating Characteristic
ROI.....	Region of Interest
RTE.....	Radiative Transport Equation
SCID.....	Severe combined immunodeficiency
SD.....	Standard deviation
SEM.....	Standard error
SFD.....	Spatial Frequency Domain
SFDI.....	Spatial Frequency Domain Imaging
SPECT.....	Single-Photon Emission Computed Tomography
StO ₂	Oxygen saturation

SWIR.....	Shortwave Infrared
TCH.....	Tukey-Ciminera-Heyse
THb.....	Total hemoglobin
US.....	Ultrasonography

CHAPTER ONE

Background and Significance

1. 1 Chemotherapy response monitoring

1.1.1 Chemotherapy: an important treatment option for cancer

Despite considerable progress in diagnosis and treatment strategies, cancer remains among the leading causes of morbidity and mortality worldwide. According to the American Cancer Society, it is the second most common cause of death in the US, exceeded only by heart disease in the US². Approximately 39.3 percent of men and women will be diagnosed with cancer of any site at some point during their lifetime, based on 2014–2016 data³. Although the 5-year relative survival rate for all cancer sites combined has increased substantially from 49% (1975-77) to 69% (2008–14) for all races in the US, there are substantial differences in survival based on tumor site, race, and most importantly tumor stage at diagnosis². Unfortunately, treatment outcome is worse for patients diagnosed with distant metastasis, for which the 5-year relative survival rate (%) can be as low as 2–5% in liver, lung, pancreas, stomach and urinary bladder cancers².

In terms of treatment, cytotoxic chemotherapy continues to be the primary weapon for combating the death toll, and is used against local and advanced cancers from almost all organ sites^{4,5}. Cytotoxic regimens are often accompanied by other available therapies, (i.e., hormonal, antiangiogenic, targeted, radiation, etc.) as well as surgery in order to improve patient response and prevent future relapse. For instance, in 2011 more than 30% of the all early- and late-staged breast cancer patients underwent surgeries followed by radiation and chemotherapy to combat clinical remission⁶. More recently, combining

cytotoxic therapy with various other treatment regimes, i.e., antiangiogenic, targeted or immunotherapy, has also gained significant interest in clinical settings ^{4,7,8}. Also, novel mechanisms are currently under investigation to improve chemotherapeutic efficacy, in the context of optimal dosing, better tumor targeting and improved delivery to the tumor location ^{9,10}.

1.1.2 Importance of early and long-term monitoring of chemotherapy response

Although chemotherapeutics has led to improved survival and quality of life for cancer patients, therapy failures are still common due to numerous reasons. First of all, chemotherapy is associated with serious side effects resulting from cytotoxicity, which limits the amount of drug administered systemically and thus causing a narrow therapeutic window ¹¹. Added to that is the absence of specific tumor targeting mechanisms in most cytotoxic drugs, which may lead to insufficient drug delivery. Additionally, therapeutic failure may be caused by multiple other factors including drug resistance, Cancer Stem Cells (CSCs), and intra-tumor heterogeneity ^{5,11,12}.

All these factors collectively lead to limited treatment response with clinical benefits only affecting a subset of patients. In consequence, patients who do not show a positive response may undergo lengthy drug regimens that in turn burden them with substantial treatment side effects while providing little or no curative benefits. This problem is exacerbated by the fact that physicians have a limited toolset for determining when to continue or when to stop and alter treatment. Long-term *in vivo* surveillance of the tumor state is regarded as imperative for predicting patient response relatively early during treatment, eventually guiding adaptive treatment decisions, including when to continue or

when to stop and alter treatment. This knowledge can potentially improve overall treatment efficacy, while at the same time significantly reduce treatment cost and burden.

1.2 Current methods are inadequate for early and long-term monitoring

Despite the urgency, physicians lack an appropriate toolset for inspecting *in vivo* tumor status in order to address important therapeutic questions. Presently, there are few clinically viable, cost effective, non-invasive and non-harmful tools for anatomic and functional *in vivo* imaging. Current anatomic modalities include Magnetic Resonance Imaging (MRI), Computed Tomography (CT), Positron Emission Tomography-CT (PET-CT), and Ultrasonography (US). Though these modalities have the advantage of high spatial resolution, they suffer from high expense and safety issues from the use of radioactive tracers and ionizing radiation¹³⁻¹⁵. Most importantly, they rely on accurate assessment of tumor size and so remain ineffective in indicating any signs of response until significant tumor debulking occurs, usually after weeks or months for many cancers^{16,17}.

Recently, functional imaging modalities, such as functional MRI (fMRI), Magnetic Resonance Spectroscopy (MRS), Dynamic Contrast Enhanced MRI (DCE-MRI), ¹⁸F-Fluorodeoxyglucose-PET (¹⁸F-FDG-PET), ¹⁸F-Fluorothymidine-PET (¹⁸F-FLT-PET), Single-Photon Emission Computed Tomography (SPECT), are making their way in the clinic, although, mostly for diagnostic applications. In the context of therapy monitoring, DCE-MRI, MRS, ¹⁸F-FDG-PET, ¹⁸F-FLT-PET have successfully linked early changes in functional markers to long term treatment response¹⁸⁻²².

These findings highlight the potential of functional imaging modalities for surveillance of treatment response *in vivo*, but these tools have significant practical and

technical limitations when used at frequent time points longitudinally. Even if the issues of safety and cost, as mentioned earlier, can be overcome, practical and technical limitations such as poor portability and discomfort from the procedures, impair their ability to perform frequent and longitudinal patient monitoring throughout treatment^{13–15,23,24}.

1.2.1 Potential of Diffuse Optical Imaging for therapy monitoring

Diffuse Optical Imaging (DOI) techniques are ideally suited to the purpose of longitudinal therapy monitoring as they have favorable safety profiles, are relatively inexpensive, do not require dedicated infrastructure, and provide important metabolic and functional information related to the *in vivo* tumor state.

1.2.2 Diffuse Optical Imaging (DOI)

Clinical DOI tools, i.e., Diffuse Optical Tomography (DOT) and Diffuse Optical Spectroscopy (DOS), are receiving significant interest as emerging non-invasive functional imaging techniques to study biological tissues *in vivo* on macroscopic scale²⁵. DOI tools typically utilize red and near-infrared (NIR) light (~600 to 1000 nm) to extract optical properties (OP: absorption: μ_a and reduced scattering: μ'_s) in centimeter thick living tissue. Light encounters relatively low absorption in human tissue at this wavelength range, enabling deeper penetration into the tissue, up to several centimeters²⁶. At distances greater than 1 to 2 mm from a source, photons lose their directionality as they undergo multiple scattering events within the complex tissue structure, and hence described as a diffusive process^{25,27}. The photon diffusion process in tissue has been previously described using the Radiation Transport Equation (RTE) model which accounts for both photon absorption

and scattering. Since the RTE is difficult to solve analytically, an approximated diffusion equation is often used in practice. The diffusion equation can be easily solved for μ_a and μ'_s dependent on measurement conditions, boundary conditions, measurement domain (i.e. frequency versus time domain), forming the basis of a variety of DOI tools ^{25,26}. Absorption values, measured at multiple wavelengths, provide access to tissue hemodynamic status and metabolic properties ²⁵; whereas, scattering measurements relate to tissue structural properties and provides knowledge about cell and organelle density as well as the extracellular matrix ²⁶.

1.2.3 Clinical DOI tools for monitoring treatment response

A growing number of reports over the last decade demonstrate the utility of DOI methodologies for tracking changes in tumor functional and metabolic properties during chemotherapy in breast cancer patients ²⁸⁻³⁰. Several reports have shown that decreases in hemoglobin content, decreases in water, and/or increases in lipids correlate with pathologic complete response (pCR) in breast cancer patients receiving presurgical neoadjuvant chemotherapy (NAC) ³¹⁻³⁴. In 2011, it was reported that a rapid gain in tumor oxyhemoglobin (HbO₂) concentration within the first day of therapy is predictive of NAC outcome, suggesting frequent tumor monitoring may reveal important early markers of response ³⁵.

1.2.4 Spatial Frequency Domain Imaging (SFDI): A potential pre-clinical chemotherapy monitoring tool

While these clinical findings by DOI tools underline their tremendous potential for clinical therapy monitoring, there has been relatively little work to date in trying to better understand the cellular, molecular, and physiological origins of these clinical observations. A small number of recent studies have correlated DOI derived metrics to immunohistochemical markers of blood vessel density and metabolism measured from clinical biopsies or surgical specimens^{36,37}. By further exploring the underpinnings of response, it may be possible to not only track treatments more effectively and early, but better schedule multi-agent regimens, test new drugs or detect early signs of therapy resistance based on DOI feedback. This will require careful control over treatments and imaging, with regular access to tumor tissue for correlative measurements. The preclinical setting is ideal for testing these ideas, but it is necessary to track the same DOI-derived parameters in small animal models in order to translate potential findings to the clinical.

Here we investigate Spatial Frequency Domain Imaging (SFDI), a DOI technique more suitable for the preclinical set up, as a new tool to monitor the *in vivo* tumor state in small animal oncology models. SFDI provides equivalent information to many clinical DOI modalities at a relatively shallower tissue depth (typically mm's)³⁸, is non-contact, and provides wide-field spatial mapping of tumor OP. To date, SFDI has been explored for a number of preclinical and clinical applications including vascular occlusions, reconstructive tissue status, monitoring burn wounds, tracking the progression of Alzheimer's disease and imaging drug delivery to the brain³⁹⁻⁴⁷. However, there are only

a small number of reports in which SFDI has been used for applications in oncology. These include studies for diagnosing human skin carcinomas, mapping breast lumpectomy specimens, developing tomographic reconstruction of brain tumors in small animals, and PDT dosing monitoring ⁴⁸⁻⁵¹.

1.3 Goal of this dissertation

This work explores the feasibility of using SFDI for frequent longitudinal monitoring of cancer chemotherapy efficacy in small animal oncology models. Towards that goal, chapter 2 establishes the feasibility of SFDI for optically characterizing a subcutaneously planted preclinical oncology model ⁵², and chapter 3 improves SFDI accuracy in subcutaneous tumor by introducing a new inversion model ⁵³. Chapter 4 explores cellular and molecular correlates of the SFDI metrics, and test which SFDI optical parameters are able to predict treatment response earlier than tumor volume or improve predictability in combination with tumor volume. Lastly, in chapter 5, a light-emitting diode (LED) based SFDI system was custom built to improve on the scope of the system, by introducing the capability of the measuring tissue water content.

CHAPTER TWO

Feasibility of Spatial Frequency Domain Imaging (SFDI) for optically characterizing a preclinical oncology model

The work in Chapter Two is published in the journal of Biomedical Optics Express with the following contributing authors ⁵²:

Syeda Tabassum,¹ Yanyu Zhao,² Raef Istfan,² Junjie Wu,³ David J. Waxman,³ and Darren Roblyer²

¹Electrical and Computer Engineering, Boston University

²Biomedical Engineering, Boston University

³Division of Cell and Molecular Biology, Department of Biology and Bioinformatics Program, Boston University

2.1 Introduction

This section explores the feasibility of using SFDI for frequent longitudinal monitoring of chemotherapy efficacy in a small animal oncology model. A mouse tumor xenograft model based on the human prostate tumor cell line PC3/2G7 was used which produces highly vascularized tumors ⁵⁴, and responds strongly to the antiangiogenic DC101 and the cytotoxic agent cyclophosphamide (CPA). In order to validate SFDI as an appropriate modality for label-free in vivo longitudinal studies, first a range of spatial frequencies was tested for their ability to accurately extract tumor optical properties. Intratumor heterogeneity and average values of SFDI parameters were assessed on individual tumors prior to treatment. Repeatability of mouse tumor measurements was evaluated under three varying procedural conditions that mimic user induced variations in mouse positioning

from measurement-to-measurement. Finally, a proof-of-concept preclinical study was performed with frequent and long-term therapy monitoring on a small number of mice.

2.2 Materials and methods

2.2.1 Spatial frequency domain imaging (SFDI): Image acquisition, processing and analysis

Detailed descriptions of SFDI instrumentation and data analysis are reported in literature^{52,55}. Briefly, SFDI utilizes projections of spatially modulated visible and/or NIR light to extract intrinsic tissue optical properties, μ_a and μ'_s , over a wide field of view (FOV), in this case 15×20 cm. For this study, the OxImager RS SFDI system (Modulim Inc., Irvine, CA) was used for all measurements, and is shown in Fig. 1.1A. Digital micromirror device (DMD) or other spatial light modulator is used to project sinusoidal or more exotic patterns onto an object of interest (e.g. tissue, calibration phantom) and the reflected light is imaged with a camera, shown in Fig. 1.1B and 1.1C. Projections are typically made at multiple wavelengths (λ) and spatial frequencies (f_x) between 0 mm⁻¹ (DC) and 0.5 mm⁻¹. A generalized example of the SFDI image processing is shown in Fig. 1.1C. AC projections are captured at three offset phases (0°, 120°, and 240°) and demodulated to obtain a single AC image using established algorithms. In this work, the DC and AC demodulated images were corrected for height and angle of the object surface respectively using a previously developed height-correction algorithm and a modified Lambertian Correction (MLC) angle correction algorithm^{56,57}. The instrument response is then removed from the demodulated images (M_{ac}) using a calibration phantom with known OPs. A Monte-Carlo (MC) based

look-up-table (LUT) or analytical forward model is used to extract the diffuse reflectance (R_d) of the calibration phantom from known OPs at each measurement wavelength and f_x (shown in Fig. 1.1C). This allows sample R_d maps to be extracted using Eq. (2.1), where subscripts sample and phantom refer to the tissue and calibration phantom, respectively.

$$R_{d_sample}(f_x) = \frac{M_{ac_sample}(f_x)}{M_{ac_phantom}(f_x)} * R_{d_phantom}(f_x) \quad (2.1)$$

Tissue R_d maps are generated at each f_x and λ and represent the turbid media optical Modulation Transfer Function (MTF). The tissue MTF is used as input to an inverse model to extract OPs on a pixel-by-pixel basis. The μ_a values extracted at each measurement wavelength were used to determine tissue chromophore concentrations using the Beer-Lambert Law, as shown in Eq. (2.2). This equation utilizes the measured μ_a values as well as known chromophore extinction coefficients, $\varepsilon(\lambda)$, for oxyhemoglobin (HbO_2) and deoxyhemoglobin (Hb) and is generated for each measured wavelength and solved as a linear system of equations to yield tissue-level chromophore concentrations of HbO_2 and Hb . From these, total hemoglobin content (THb: $HbO_2 + Hb$) and oxygen saturation (StO₂: $HbO_2/THb \times 100$) are also determined²⁵. Wavelength dependent μ'_s data was fit to a power law using a least square fitting approach to extract scattering amplitude (a) and scattering slope (b) for each spatial location within the FOV, as shown in Eq. (2.3). A reference wavelength, λ_o , of 800 nm was used for the power law fitting. Upon completion of processing, maps of each SFDI parameter ($\mu_a(\lambda)$, $\mu'_s(\lambda)$, a, b, HbO_2 , Hb , THb and StO₂) is generated.

$$\mu_a(\lambda) = \varepsilon_{HbO_2}(\lambda) * C_{HbO_2} + \varepsilon_{Hb}(\lambda) * C_{Hb} \quad (2.2)$$

$$\mu'_s = a (\lambda/\lambda_o)^{-b} \quad (2.3)$$

The SFDI system used in this work typically accommodated up to 3 mice at a time. Mice were imaged on a diffuse silicone background phantom. For this section, five spatial frequencies ($f_x = 0, 0.05, 0.1, 0.15$ and 0.2 mm^{-1}), and four wavelengths (659, 691, 731 and 851 nm) were collected sequentially. Each SFDI measurement was repeated thrice and averaged to minimize breathing artifacts. Typical acquisition times were less than 1.25 minutes for this acquisition setup. Raw imaging data was processed using a custom Matlab code that performed demodulation, height and angle corrections, calibration, optical property extractions, and chromophore extractions. For this section, a two- f_x -look-up table (LUT) based homogeneous inverse model was used to extract maps of μ_a and μ'_s for each of the acquisition wavelength. Data processing took approximately two minutes for each measurement.

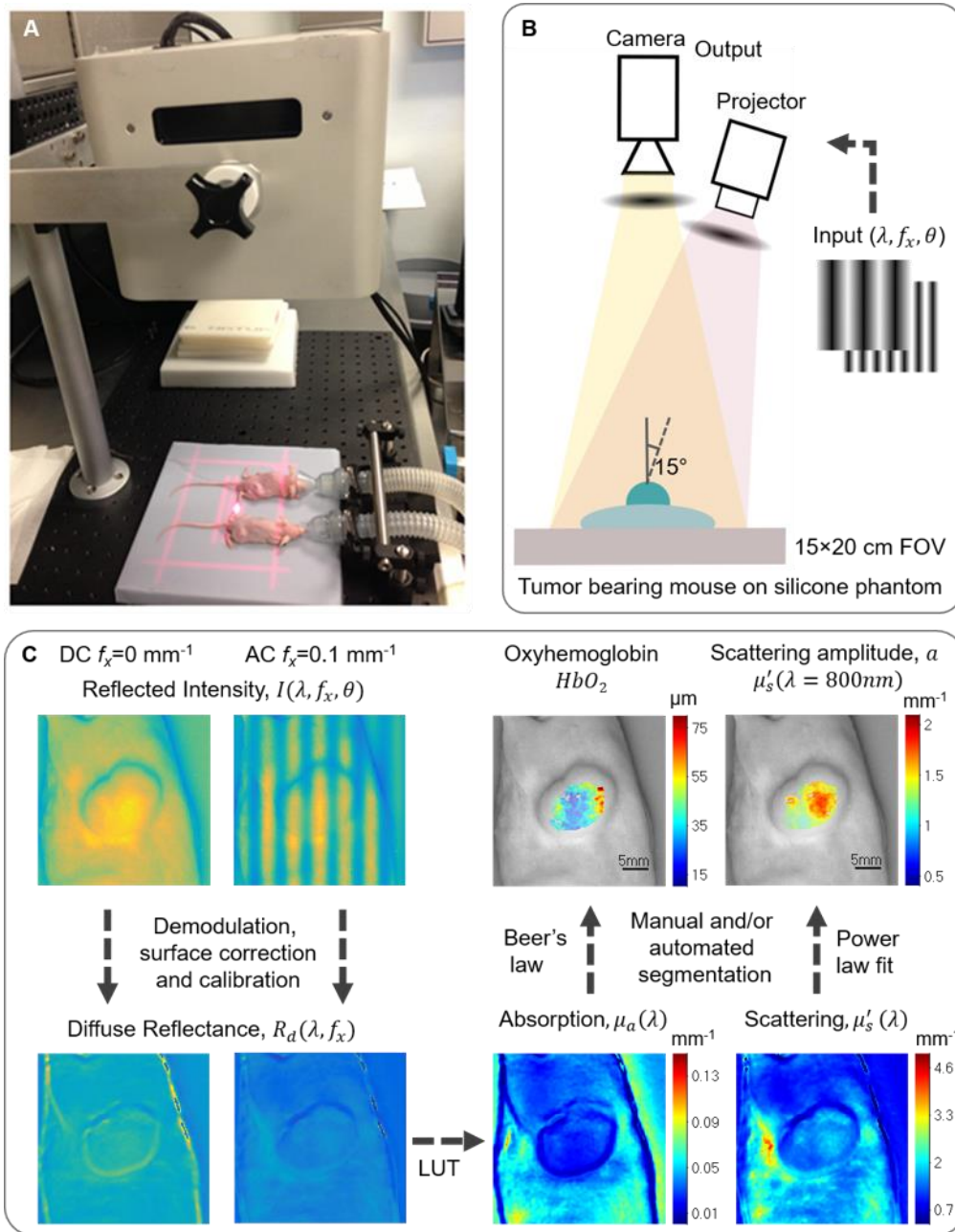


Figure 2.1: A, Mouse imaging set up with OxImager RS SFDI system (Modulim Inc., Irvine, CA). B, SFDI schematic. C, SFDI image processing pipeline using a single representative PC3/2G7 tumor measurements at baseline timepoint. The intensity images (I) and R_d maps are shown at $\lambda=731\text{nm}$ for two spatial frequencies (f_x : 0 mm^{-1} (DC) and 0.1 mm^{-1} (AC)). The absorption and scattering maps are shown at $\lambda=731\text{nm}$. Edge artifact is clear around tumor margin in the absorption image, which is addressed through several automated and/or manual segmentation steps. The oxyhemoglobin image shows HbO_2 map from the final tumor area of interest superimposed on a DC intensity image. The scattering amplitude image shows a map from the final tumor area of interest superimposed on the same DC intensity image.

2.2.2 Selection of spatial frequencies

The choice of SFDI spatial frequencies is important for accurate separation of absorption and scattering. Generally, DC and lower spatial frequencies are sensitive to both absorption and scattering, while higher spatial frequencies are preferentially sensitive to scattering. Additionally, the effective photon penetration depth is a function of spatial frequency, and higher spatial frequencies probe more shallow tissue depths⁵⁵. Loosely speaking, if both very low and very high spatial frequencies are used to extract optical properties, partial volume effects may cause errors in OP and chromophore extractions if the measured tissue is not homogeneous in depth. The methods outlined here were designed to determine a two frequency pair that balances accurate OP extractions while minimizing the difference between the two frequencies, and subsequently the difference in probing depth. A range of spatial frequencies was tested for their ability to accurately extract OPs using a two- f_x -LUT. For all tests, DC ($f_x = 0 \text{ mm}^{-1}$) was paired with a second, higher AC spatial frequency ($f_x = 0.025, 0.05, 0.1, 0.15, 0.2, 0.3, \text{ or } 0.5 \text{ mm}^{-1}$). Each combination of DC and AC spatial frequency was compared over a physiologically relevant range of OPs. First, a μ_a and μ'_s pair was chosen. Then, the forward LUT model was used to determine R_d values at the DC and AC spatial frequencies. Next, Gaussian noise was added to these R_d values to simulate experimental measurement noise. Then the two- f_x -LUT was used to back calculate the OP pair. Error was calculated between the original and the estimated OP pair. This process was iterated 1000 times for each OP pair (4 total) and each spatial frequency pair (7 total). The average OP error was calculated and compared for all of the f_x pairs tested and over the range of OPs.

The magnitude of the added Gaussian noise at each spatial frequency was determined by taking 10 repeat measurements on 3 different tumors from 3 different mice (using tumor model and mouse strain used in this work) and calculating the average standard deviation in R_d over the 4 measurement wavelengths. The noise levels from DC and four AC spatial frequencies (0.05, 0.1, 0.15, and 0.2 mm^{-1}) were fit to an exponential curve, and fit and extrapolated noise values were then used as estimates of noise for all eight spatial frequencies. OPs were chosen from 10 evenly distributed μ_a values (0.003 - 0.055 mm^{-1}) and 10 μ'_s values (0.5 - 3 mm^{-1}); this range in OPs was based on tumor OP measurements from 3 mice measured with SFDI at 47 longitudinal time points over 45 days.

2.2.3 Spectral chromophore fitting

The agreement in broadband spectral fits to the four extracted μ_a values was calculated for a set of pixels in several tumor measurements to confirm the ability to accurately fit HbO₂ and Hb. First, HbO₂ and Hb tissue concentrations were determined using the Beer-Lambert Law and the four μ_a values, as described in section 2.1. Then, these HbO₂ and Hb tissue concentrations were multiplied by their corresponding extinction spectra; this was done for every nm increment from 600 to 1000 nm. Tissue μ_a values at each of these wavelengths was determined by summing the μ_a contribution from both HbO₂ and Hb, providing a broadband tissue μ_a spectrum. This μ_a spectrum was plotted with the original four μ_a values, and the % difference between these values at the 4 wavelengths was determined. This same procedure was repeated for scattering, using the a and b scattering parameters

to generate the broadband μ'_s spectrum (see Eq. (3)). This procedure is useful for confirming chromophore fitting and for finding outliers in OP extractions.

2.2.4 Average tumor values and intratumor heterogeneity

For analysis of all mouse tumor data in this section, a region of interest (ROI) was manually chosen over the tumor. This ROI was chosen from the extracted μ_a map; pixels at the extreme edge of the tumor were excluded. A software mask was used to keep only pixels at or below a 70° angle relative to the camera axis. This angle mask typically rejected less than 10% of pixels within a tumor ROI. The 70° threshold was chosen based on the working range of the angle correction algorithm⁵⁷. Additionally, pixels with very low μ_a values ($\mu_a < 0.0001 \text{ mm}^{-1}$) were also masked. The average and standard deviation of all remaining pixels within a tumor ROI were calculated for all SFDI parameters. Average tumor values and intratumor heterogeneity in SFDI parameters were assessed using 25 tumor data from 13 different mice measured at baseline (prior to any treatment). For average values, first the mean parameter value over each tumor ROI was calculated. Then the average and standard deviation of these values was calculated over the 25 tumors to get typical values and ranges for this xenograft tumor model. For intratumor heterogeneity, first, the % standard deviation was determined for each tumor ROI. Then, the mean tumor heterogeneity was calculated over the 25 tumors. The average tumor values are useful for comparisons to other literature values, and the heterogeneity quantifies the variation in SFDI parameters within single tumors and provides a context for which longitudinal changes can be analyzed.

2.2.5 Repeatability

High measurement repeatability is essential for high quality longitudinal chemotherapy monitoring studies. Repeat measurements were taken on individual mouse tumors under a variety of conditions to assess device and user procedure repeatability. To evaluate device repeatability, 10 repeat measurements were taken on individual tumors without making any changes in the instrument or experimental setup between measurements. This condition will be referred to as stationary. User repeatability was assessed in two ways. First, 10 repeat measurements were taken with the mouse removed from the imaging FOV and replaced in similar manner after each measurement. This condition will be referred to as move & replace. Secondly, to assess the effects of angular changes in mouse position between measurements, similar to those which might unintentionally occur during the course of a longitudinal study, a custom made tilting platform was used to collect 11 repeat measurements on individual tumors tilted at 11 different angles ($0^\circ, \pm 3^\circ, \pm 6^\circ, \pm 9^\circ, \pm 12^\circ, \pm 15^\circ$) with respect to horizontal, as shown in Fig. 2.2A. The tumor was carefully placed at center of rotation of the tilting platform. Then, the platform was gradually tilted to higher angles, one side at a time. This condition will be referred to as tilt. In the case of stationary measurements, the tumor ROIs and all data analysis procedures were kept identical for all repeat measurements. For move & replace and tilt measurements, each repeat measurement was treated as a separate and unique measurement, and a separate ROI was manually chosen each time. The ROI area between repeat measurements were kept within approximately ± 150 total pixels of each other to ensure that variations over measurements were not dominated by different ROI selection sizes. For each of the repeat measurement

conditions, the variation in OPs was determined by evaluating the % standard deviation of the mean ROI values. This was done for $n = 12$ tumors for stationary, $n = 12$ tumors for move & replace and $n = 10$ tumors for tilt. The average % standard deviation was calculated over the four wavelengths for all tumors. For tilt measurements, average variations were determined over all tilt angles (up to $\pm 15^\circ$), over the first 7 angles (up to $\pm 9^\circ$), and over the first 5 angles (up to $\pm 6^\circ$).

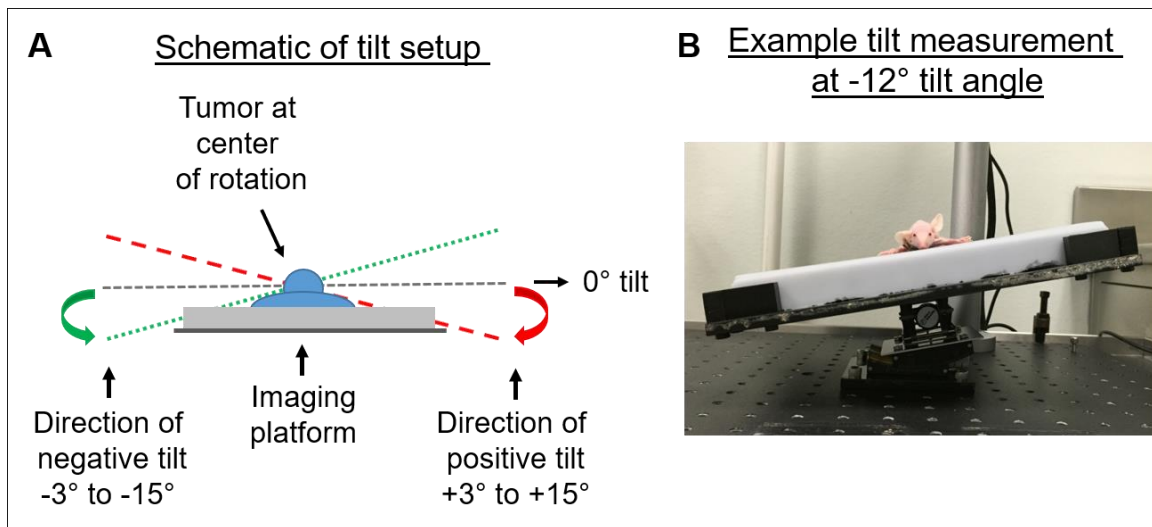


Figure 2.2: A, Schematic of tilt measurement. B, Example of a tilt measurement.

2.2.6 Mouse tumor xenograft

The PC3/2G7 prostate tumor xenograft model was used for all tumor experiments⁵⁴. PC3/2G7 cells were grown and expanded at 37°C in a humidified 5% CO₂ atmosphere in RPMI-1640 culture medium containing 7% fetal bovine serum, 100 Units/ml penicillin and 100 µg/ml streptomycin cells were split in 1:3 or 1:4 when cells reached 70-80% confluence to maintain holoclone-forming ability (approximately one passage every 3 days). Severe combined immunodeficient (SCID) hairless outbred mice (SHO MouseCrl:SHOPrkdscidHrhr), age 5 to 6 weeks old (21-23 gram), were purchased from

Charles River Laboratories, and housed in the Boston University Laboratory Animal Care Facility in accordance with an institutionally approved protocol (IACUC 16-003) and federal guidelines. Autoclaved cages containing food and water were changed once a week. Mouse body weight was measured every 3 to 4 days. On the day of tumor cell inoculation, 4×10^6 PC3/2G7 cells were injected on one or two posterior flanks subcutaneously in 0.2 ml serum-free RPMI using a U-100 insulin syringe with a 28.5 gauge needle. Tumor length (L) and width (W) was measured daily starting from 5 days before treatment, every 3 days during treatment, and twice weekly after treatment using digital calipers (VWR International). Tumor volume was calculated as $Vol = (\pi/6) \times (L \times W)^{3/2}$. When average tumor volume reached $\sim 500 \text{ mm}^3$, mice were treated with either the cytotoxic anticancer drug CPA or the antiangiogenic agent DC101, both given i.p. CPA interferes with DNA replication by forming DNA crosslinks, whereas DC101 is an antagonist monoclonal antibody to mouse VEGF receptor 2 (VEGFR-2). Mice were given CPA on a metronomic schedule at a dose of 140.3 mg/kg every 6 days for 3 cycles. DC101 was administered at a dose of 28.6 mg/kg every 3 days for 6 cycles. CPA was purchased from Sigma Chemical Co. (St. Louis, MO), and DC101 was a gift from Eli Lilly and Company, Indianapolis, Indiana. During SFDI measurements, mice were anesthetized using isoflurane by inhalation (5% induction); except for tilt measurements when mice were anesthetized using ketamine at 50-100 mg/kg + xylazine at 10-15 mg/kg. Mice were euthanized as they approached the tumor size limit using cervical dislocation according to the approved protocol.

2.2.7 Longitudinal monitoring of tumor xenograft

SFDI was used to measure tumors in two mice, one treated with CPA and one with DC101. Mice were treated longitudinally for a total of 57 days, including 5 timepoints during the 7 days of tumor growth. SFDI measurements were taken everyday during the 18 days of treatment, and every 2 days during the 22 days after treatment (tumor growth rebound period). In addition to general data processing steps as described in subsection 2.1, a fine tuning algorithm was applied to tissue R_d maps prior to OP extraction. This fine tuning algorithm was developed to correct for changes in system response during warm-up, which we found cause as much as a 5% change in OPs measured at 659 nm in the first 40 minutes the system was powered on. This algorithm relies on the fact that same background imaging phantom was used for all mouse measurements. The R_d of this phantom at all relevant wavelengths and spatial frequencies was determined by an SFDI measurement taken after the system stabilized over a 2-hour timeframe. These R_d values were then used as a gold standard to fine-tune R_d extractions with each imaging field for all mouse measurements. For each new measurement during a longitudinal study, the extracted R_d values at each wavelength and spatial frequency were compared to the gold standard R_d values, and small variations were corrected using Eq. (2.4).

$$R_{d_fine_tuned}(x, y, wv, fx) = R_d(x, y, wv, fx) \frac{R_{d_gold_standard}(wv, fx)}{R_d(wv, fx)_{ROI}} \quad (2.4)$$

Here, $R_{d_gold_standard}(wv, fx)$ are the average R_d values of the background phantom measured after 2 hours of instrument warmup over a 100×150 pixel ROI. $R_d(wv, fx)_{ROI}$ is the current measurement R_d , extracted from the average values over the same 100×150 pixel ROI on the background phantom. $R_d(x, y, wv, fx)$ is the uncorrected R_d values at each pixel

in the FOV, and $R_{d_fine\ tuned}(x, y, wv, fx)$ are the corrected, or *fine tuned*, R_d values at each pixel in the FOV. The fine-tuning algorithm was evaluated by taking 25 repeat phantom measurements over a 41-day period. Optical property precision values were calculated with and without fine tuning.

2.3 Results

2.3.1 Selection of spatial frequencies

In order to visualize how different choices of SFDI spatial frequencies affect the accuracy of optical property extractions, a range of spatial frequencies was tested using simulated data. Figure 2.3 shows visualizations of four different two- f_x -LUT's. For each, the horizontal axis represents R_d at DC ($f_x = 0\text{ mm}^{-1}$) and the vertical axis represents R_d at an AC frequency ($f_x = 0.025, 0.1, 0.2, \text{ or } 0.5\text{ mm}^{-1}$). R_d values are plotted for 10 evenly distributed μ_a values ($0.003 - 0.055\text{ mm}^{-1}$) and 10 evenly distributed μ'_s values ($0.5 - 3\text{ mm}^{-1}$). Differences in the orthogonality of the LUT's are visually apparent, and in some cases, there is significant coupling between μ_a and μ'_s (e.g. Fig. 2.3A). In cases where OP isolines collapse on each other the sensitivity to small errors in R_d measurements is likely to manifest as a large error in OP extractions.

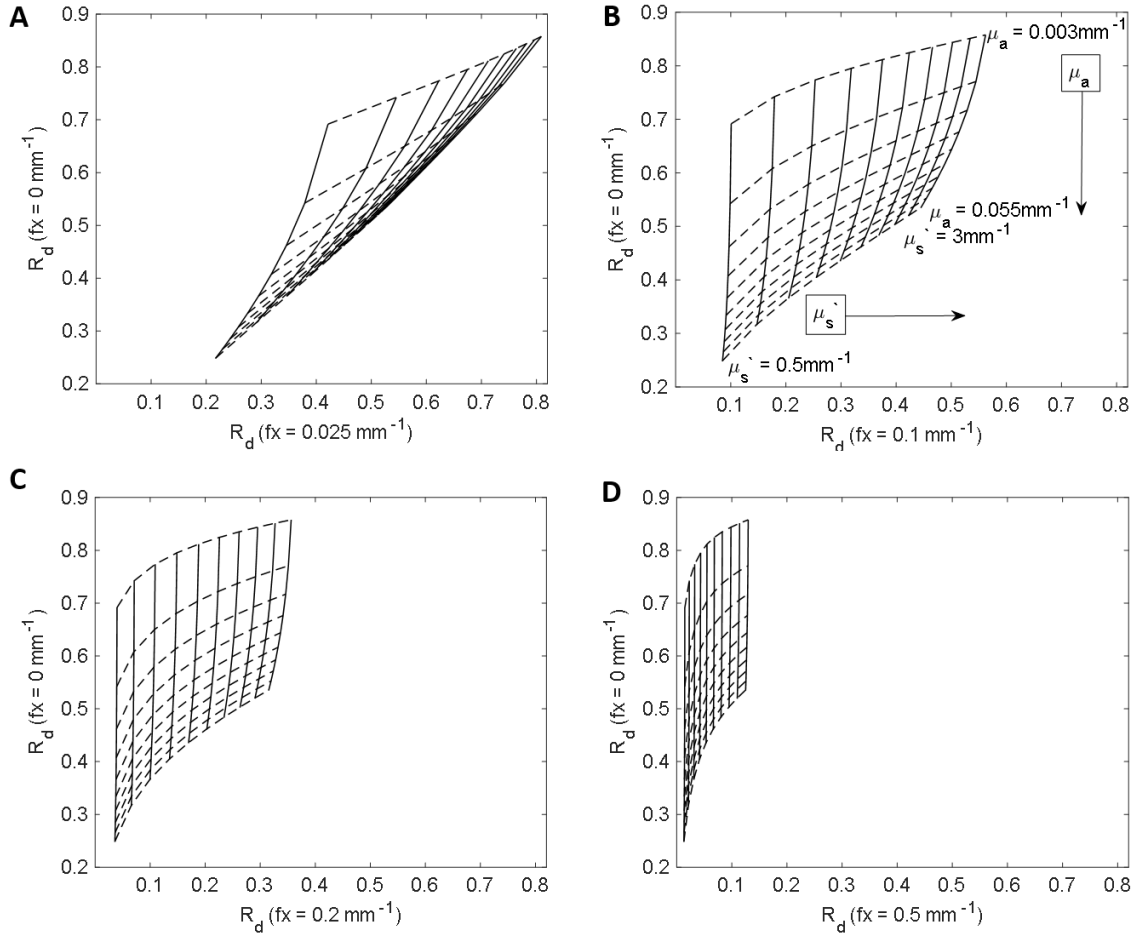


Figure 2.3: Two- f_x -LUT's using 10 evenly distributed μ_a values (0.003 – 0.055 mm^{-1}) and 10 evenly distributed μ_s values (0.5 - 3 mm^{-1}) for DC and 0.025 mm^{-1} (A), DC and 0.1 mm^{-1} (B), DC and 0.2 mm^{-1} (C), DC and 0.5 mm^{-1} (D) f_x pairs.

Figure 2.4 shows OP extraction errors induced by noise added to R_d values in simulation for seven different choices of SFDI spatial frequency pairs. Errors are shown for four different OP pairs representing the four quadrants of the LUT in Fig. 2.3. In all cases, relatively high OP extraction errors occurred when DC was paired with a low AC f_x (e.g. 0.025 mm^{-1} , 0.05 mm^{-1}). For this study, DC and 0.1 mm^{-1} were chosen for all subsequent OP extractions. OP extractions errors were low for this pair (< 2.4% for the range of OPs tested), and this pair minimized depth probe differences better than combinations that

included a higher AC f_x .

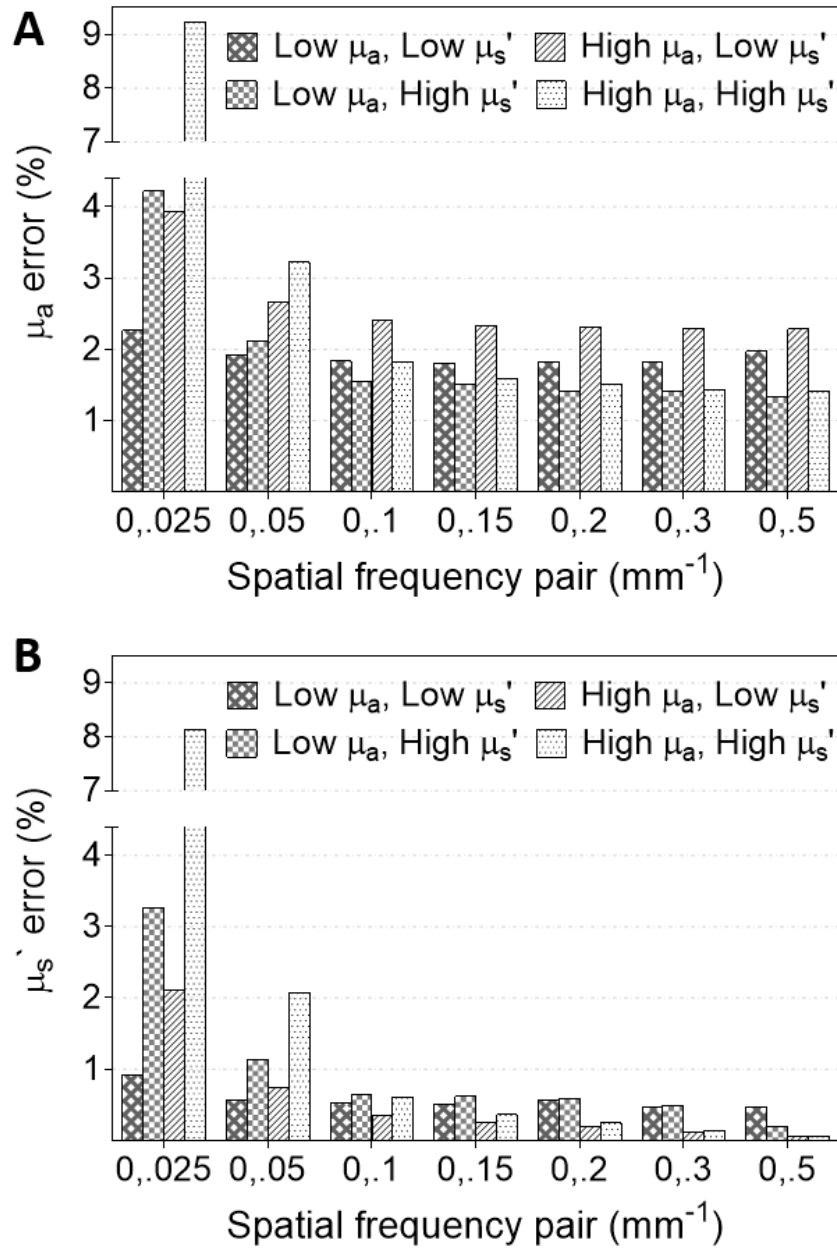


Figure 2.4: Extraction error of μ_a (A) and μ'_s (B), where low $\mu_a = 0.005 \text{ mm}^{-1}$, low $\mu'_s = 0.73 \text{ mm}^{-1}$, high $\mu_a = 0.035 \text{ mm}^{-1}$, and high $\mu'_s = 1.89 \text{ mm}^{-1}$.

2.3.2 Spectral fitting

Figure 2.5B,D shows μ_a and μ'_s values extracted at the four SFDI acquisition wavelengths as well as the broadband μ_a and μ'_s spectra after chromophore fitting and power law fitting, respectively. Data is shown for a single pixel located on the tumor of a mouse treated with the antiangiogenic agent DC101. Figure 2.5A and Fig. 2.5C displays the pixel location, on the same tumor, at a pretreatment (baseline) and a posttreatment timepoints (day 32 after initial DC101 injection, 17 days after the final DC101 injection). In general, there was good agreement between the extracted μ_a and μ'_s values and the broadband fits. Fitting errors were less than 5% for μ'_s in all tumors measured. Fitting errors for μ_a ranged between 5% up to 20%, with larger errors often observed at 731 nm. Overall absorption throughout the measured spectral range decreased by posttreatment compared to baseline, whereas scattering amplitude increased. This was a common trend for most measured tumors. It should be noted that lipids and water were not included as chromophores in this study, and therefore μ_a values are likely underreported in the 900–1000 nm range in Fig. 2.5.

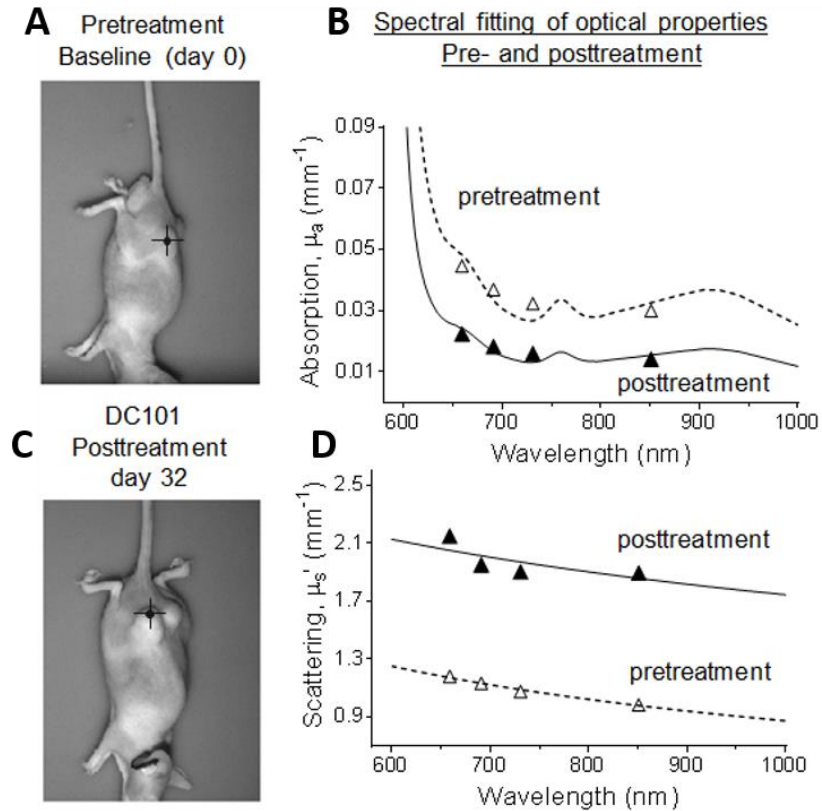


Figure 2.5: Locations of pixels on a DC101-treated tumor at pretreatment (A) and posttreatment (C) timepoints. Broadband fitting of absorption (B) and scattering (D) for pre- and posttreatment timepoints.

2.3.3 Average tumor values and intratumor heterogeneity

Table 1 shows the average tumor values measured over 25 tumors from 13 mice. All measurements were taken prior to any drug treatment. The average tumor volume for the 25 tumors was $801 \pm 785 \text{ mm}^3$.

SFDI acquired parameters	Tumor Average \pm std
a	$0.9 \pm 0.1 \text{ mm}^{-1}$
b	0.7 ± 0.1
HbO ₂	$69.8 \pm 18.7 \text{ }\mu\text{M}$
Hb	$45.1 \pm 5.3 \text{ }\mu\text{M}$
THb	$114.9 \pm 22.3 \text{ }\mu\text{M}$
StO ₂	$59.9 \pm 5.1 \%$

Table 2.1. Average SFDI parameters for tumors

Table 2 shows the percent intratumor heterogeneity in SFDI parameters measured over 25 tumors from 13 mice. Tumor heterogeneity was approximately 9–10% for OPs at all wavelengths. Heterogeneity was higher (15.1%) in the b parameter, and substantially lower (3.7%) in StO₂. In order to explore what effect tumor size has on heterogeneity, the largest five and smallest five tumors were analyzed separately. The largest five tumors had an average volume of $2023 \pm 722 \text{ mm}^3$ and the smallest five had an average volume of $181 \pm 76 \text{ mm}^3$. Heterogeneity in optical properties in the largest tumors was 11.0% on average compared to 8.4% for the smaller tumors. StO₂ heterogeneity was 4.3% in the largest tumors compared to 2.6% in the smallest tumors. These average and heterogeneity values can help provide context to any observed longitudinal changes in future studies.

SFDI acquired parameters		Average Tumor Heterogeneity	
μ_a	wavelength	659 nm	$9.0 \pm 2.7 \%$
		691 nm	$9.3 \pm 3.0 \%$
		731 nm	$9.6 \pm 3.3 \%$
		851 nm	$9.7 \pm 3.6 \%$
μ_s'	wavelength	659 nm	$9.2 \pm 2.9 \%$
		691 nm	$9.3 \pm 3.0 \%$
		731 nm	$9.3 \pm 3.0 \%$
		851 nm	$9.8 \pm 3.2 \%$
a		$9.5 \pm 3.1 \%$	
b		$15.1 \pm 4.6 \%$	
HbO ₂		$11.6 \pm 4.6 \%$	
Hb		$9.3 \pm 2.7 \%$	
THb		$9.6 \pm 3.6 \%$	
StO ₂		$3.7 \pm 1.9 \%$	

Table 2.2. Intratumor heterogeneity

2.3.4 Repeatability

Figure 2.6 shows example μ_a and μ_s' extractions at 851 nm for a representative tumor for

10 stationary, 10 move & replace, and 11 tilt repeat measurements. Small changes in OPs were observed during stationary repeat measurements; this example had a precision of 0.57% and 0.61% for μ_a and μ_s' respectively. There was slightly larger variability for the move & replace measurements, with precisions of 3.30% and 1.13%. For tilt measurements, the precision was 5.51% and 1.42%, but improved when only the first 7 tilt angles (0 to $\pm 9^\circ$), were analyzed (precision = 2.75% and 1.30%), or first 5 tilt angles (0 to $\pm 6^\circ$) were analyzed (precision = 2.61% and 1.49%).

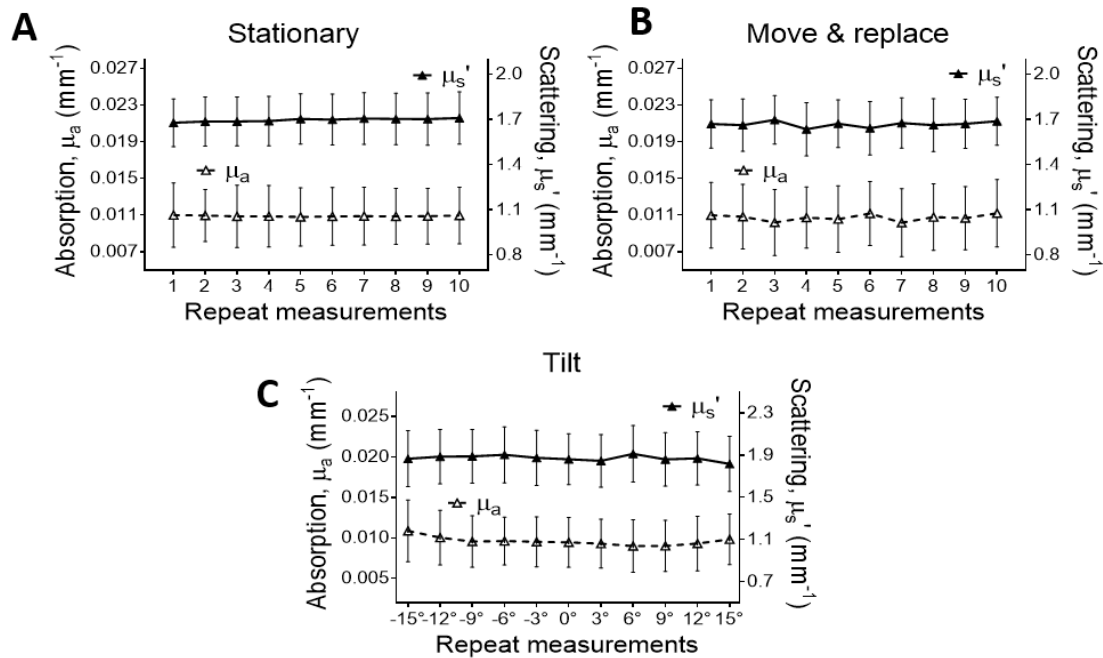


Figure 2.6: Absorption (left axis) and scattering (right axis) at 851nm for a representative tumor over 10 stationary (A), 10 move & replace (B), and 11 tilt (C) repeat measurements.

Table 2.3 shows average precision (repeatability) values from 8 mice for *stationary* ($n = 12$ tumors), *move & replace* ($n = 12$ tumors), and *tilt* conditions ($n = 10$ tumors). In general, high repeatability (precision $\leq 5.2\%$) was achieved for most repeat measurements except for those conducted at tilt angles larger than 9° . High repeatability for *stationary*

measurements helps to confirm instrument stability. High precision for *move & replace* measurements helps to confirm the repeatability of the user to position and image the mouse in a similar manner. High precision in the *tilt* measurements helps to confirm that even with small changes in the placement of the mouse, repeatable longitudinal measurements are possible. Taken together, these results suggest OP changes larger than a few percent observed over the course of a longitudinal study are likely to be from intrinsic changes in the tumor rather than from small changes in instrument or user procedures. The *tilt* results suggest that care should be taken to position the animal/tumor as consistently as possible during each imaging session.

Optical Properties	Average repeatability				
	Stationary n = 12	Move & replace n = 12	Tilt n = 10		
			0 to $\pm 15^\circ$	0 to $\pm 9^\circ$	0 to $\pm 6^\circ$
μ_a	1.88 %	3.52 %	10.14 %	5.22 %	4.44 %
μ'_s	0.98 %	2.30 %	3.70 %	2.43 %	2.13 %

Table 2.3. Repeatability (Precision)

2.3.5 Longitudinal monitoring of tumor xenografts

The fine-tuning algorithm improved measurement precision by as much as 17-fold. The measurement precision at 659 nm improved from 3.1% to 0.3% for μ_a , and from 1.7% to 0.1% for μ'_s with the use of the fine-tuning algorithm over 25 repeat phantom measurements. Fine tuning was used for all longitudinal mouse measurements.

Two mice were tracked longitudinally during the course of chemotherapy as a proof-of-principle demonstration of SFDI for treatment monitoring. Figure 2.7A shows

changes in tumor μ'_s at 659 nm from a single tumor over the course of 45 days. This mouse received the antiangiogenic DC101 (6 total injections; injections were given every 3 days, injection dates are indicated by the vertical dashed lines). The mean and standard deviation of μ'_s values extracted over a manually chosen ROI are shown. Tumor volume measurements are shown for reference. During treatment, the average tumor μ'_s increased by approximately 50%. This upward trend continued until treatment ~day 22, with a maximum increase of approximately 70% from baseline, followed by a substantial decrease. These trends do not appear to be related only to tumor volume changes, as μ'_s both increases and decreases during periods of tumor growth. It is plausible that the change from decreasing to increasing μ'_s at day 3 is predictive of treatment response, but this must be confirmed with additional studies. Figure 2.7B shows tumor μ'_s colormaps overlaid on a planar mouse image at day 0 and day 24. Substantial changes in μ'_s values are apparent throughout the tumor region at these timepoints.

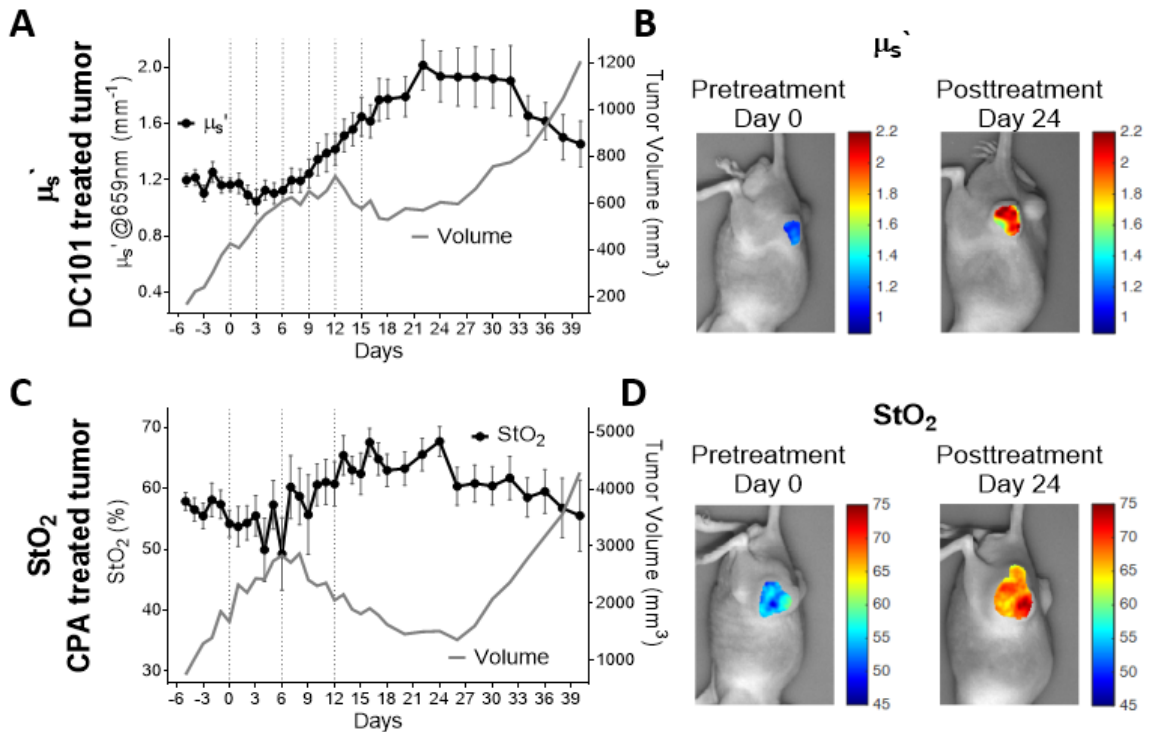


Figure 2.7. μ_s' (left axis) and tumor volume (right axis) over days of DC101 treated tumor (A), μ_s' colormaps overlaid on the DC101 treated planar mouse image at day 0 and day 24 (B), StO₂ (left axis) and tumor volume (right axis) over days for CPA treated tumor (C), StO₂ colormaps overlaid on the CPA treated planar mouse image at day 0 and day 24 (D).

Figure 2.7C shows tumor StO₂ changes during the course of treatment. This mouse was treated with CPA (3 total injections; injections were given every 6 days), followed by a rebound period. In this tumor, StO₂ initially appears to decrease during rapid tumor growth, but then increases by approximately 25% compared to baseline as CPA treatment takes effect. StO₂ decreases again during the treatment rebound stage correlating with rapid tumor growth. Figure 2.7D shows the substantial increase in StO₂ from day 0 to day 24. Again, these changes are apparent throughout the tumor area.

2.4 Discussion

Diffuse Optical Imaging is a promising *in vivo* technique for clinical tumor therapy monitoring in cancer patients. The development of complementary preclinical imaging modalities that can track the same optical markers may allow for the exploration of more advanced treatment regimens, multi-agent therapy scheduling, and a better understanding of the biological underpinnings of treatment effects. Towards this aim, this section demonstrated the feasibility of using SFDI to measure mouse tumor xenografts with high repeatability and to longitudinally monitor therapy efficacy⁵². High *in vivo* measurement precision was demonstrated using a two-frequency LUT inverse model. Average OP and chromophore values, as well as intratumor heterogeneity were reported for a highly vascularized subcutaneous xenograft prostate tumor model. A proof-of-concept longitudinal study demonstrated that SFDI was able to track changes during treatment and rebound with both the cytotoxic drug CPA and the antiangiogenic agent DC101. In general, tumor OP values showed contrast between pre- and posttreatment days, and the changes in optical parameters tracked were substantially larger than the variation expected from instrument precision, measurement-to-measurement differences in mouse positioning, and intratumor heterogeneity.

Several important SFDI acquisition parameters and measurement procedures were tested in this section, including the choice of spatial frequencies for OP extractions, and the effects of instrument and repositioning errors for repeat measurements. For spatial frequency comparisons, various f_x pairs were tested for accuracy in OP extractions. While all f_x pairs tested provided <10% OP extractions errors, it was found that combinations of

DC plus low (0.025 mm^{-1} and 0.05 mm^{-1}) AC f_x choices produced larger relative extraction errors. For this study, the DC plus 0.1 mm^{-1} pair was chosen for all data analysis based on small extraction errors ($\sim 2.4\%$) and the avoidance of partial volume probing effects likely to occur from the use of more disparate f_x pairs. While higher dimension LUTs could accommodate more spatial frequencies in the inversion process, the use of only a pair minimizes data acquisition time, which may reduce breathing motion artifacts, reduce the time mice are under anesthesia, and reduce user burden, which can be substantial for studies incorporating multiple treatment groups over long timescales (i.e. months).

Instrument and user placement repeatability were generally high (precision $\leq 5.2\%$) for all tested cases except for measurement at large tilt angles ($\pm 15^\circ$) where μ_a precision was as high as 10%. This is likely due to the capture of a different tumor field-of-view at large tilt angles. Tumor heterogeneity is a well-known phenomenon^{12,58} and intratumor heterogeneity was shown to be as high as 10% for optical properties extractions in this study. Measurement of a different region of the same tumor is likely to yield different results, suggesting that care must be employed when positioning mice for repeat measurements.

Broadband μ'_s power-law fitting errors were typically small ($< 5\%$) and broadband chromophore μ_a fits were also generally small, except at 731nm, where μ_a fitting errors typically ranged from 15% to 20%. These errors may occur in part due to spectral bandwidth of the LED source ($\sim 20\text{nm}$), which spans the dip in the Hb extinction coefficient near 731nm⁵⁹. Although the choice of acquisition wavelengths was not tested here, it was previously shown that 670 nm and 850 nm is an optimal two-wavelength choice for oxy-

and deoxyhemoglobin extraction using SFD⁶⁰. These wavelengths closely match two of the four wavelengths used in this study (i.e. 659, 691, 731, and 851 nm).

Despite expected variation in metabolism, vascular density, and tissue architecture between different murine tumor models, baseline optical property and chromophore values reported here are in agreement with several other small animal tumor values reported in the literature. For example, the average baseline μ'_s value at 630nm was found to be 1.064 mm^{-1} (this value was calculated using the average of the a and b values from Table 2.1 and Eq. (2.3)). This agrees well with the reported μ'_s value of 1.048 mm^{-1} at 630 nm in a radiation-induced fibrosarcoma tumor model in C3H mice measured with a fiber-optic probe-based continuous-wave Diffuse Reflectance Spectroscopy (DRS) system prior to any treatment⁶¹. Average tumor StO_2 values reported here (59.9 ± 5.1 %) were somewhat higher than StO_2 values (40% – 55%) reported in K1735 malignant mouse melanoma subcutaneous tumors measured before treatment by DRS⁶². The increasing trend in both μ'_s and StO_2 during treatment mimics those reported by Karthik *et. al.* who used a DRS point probe to monitor 4T1 flank tumors ($n = 25$) treated with a single maximum tolerated dose of doxorubicin over a 13 day treatment period⁶³. We hypothesize that changes in SFDI parameters during treatment may be related to a reduction in tumor vasculature and tissue remodeling, but this must be confirmed with future studies. Parameters such as tumor heterogeneity and average optical parameters are specific to the PC3/2G7 xenograft model tested here, and other tumor models are likely to have different properties.

While the results from this study are promising, there are several challenges and limitations to the use of SFDI for small animal imaging. Correction for height and surface

angle were essential for accurate optical property extractions due to the small mouse feature size and the large relative surface angles of the tumors; substantial edge artifacts occurred prior to the applications of appropriate corrections ^{56,57}. Depth penetration and partial volume effects are also important considerations. In this study, attempts were made to reduce differences in penetration depth by choosing a pair of spatial frequencies that accurately separated absorption and scattering effects while minimizing the difference in spatial frequency and thus depth penetration, but additional modeling studies are needed to better determine the implications of these effects. Tomographic reconstructions using SFDI have previously been demonstrated and would assist in providing depth resolved information for this application in the future ⁶⁴. An additional limitation was that only oxy- and deoxyhemoglobin were extracted in this study and there may be prognostically relevant information content in other chromophores including lipids and water. Finally, a better understanding of the biological origins of treatment-induced changes observed in SFDI is necessary to take full advantage of this technique.

2.5 Conclusions

In conclusion, SFDI is a promising technique for high precision, longitudinal non-contact and label free metabolic imaging of small animal tumor models. In comparison with intravital techniques including confocal and multiphoton microscopy, SFDI does not require invasive procedures such as skin-flap removal or window chamber implantation, and does not require exogenous agents, parameters which limit their suitability for long term therapy monitoring ⁶⁵. SFDI complements other non-invasive diffuse optical techniques such as DRS and Diffuse Correlation Spectroscopy (DCS), which are also under

investigation for monitoring hemodynamic response in a variety of preclinical models^{62,63,66,67}. Knowledge learnt from this section, in the long term, will help establish SFDI as important feedback methods during cancer treatment.

CHAPTER THREE

Two-layer inverse model for improved longitudinal preclinical tumor imaging in the Spatial Frequency Domain Imaging (SFDI)

The work in Chapter Three is published in the Journal of Biomedical Optics with the following contributing authors ⁵³:

Syeda Tabassum,¹ Vivian Pera,¹ Gage Greening,² Timothy J. Muldoon,² Darren Roblyer¹

¹Boston University, United States

²University of Arkansas, United States

3.1 Introduction

SFDI is a wide-field DOI modality, capable of tracking the same non-invasive and label-free metrics measured using clinical DOI modalities, and is well suited for preclinical oncology work given its shallower penetration depth (typically mm's) ⁶⁸. Much of the prior published works using SFDI for both small animal and clinical research have utilized the assumption of homogeneity in depth when extracting optical properties from tissue ^{40,41,43,48}. For example, in our prior preclinical monitoring study, we modelled mouse tumor tissue as a semi-infinite homogeneous medium, and used the results of a Monte Carlo (MC) simulation to create a look-up table (LUT) inversion algorithm to recover optical property estimates from SFDI measurements of diffuse reflectance ⁵². However, tissue geometry is complex, and in the case of subcutaneous tumors in mice, a thin skin layer is located above the tumor which remains unaccounted for in a homogeneous model. While there are several prior studies that have described inversion algorithms that utilize a layered-tissue structure

^{69–72} or utilize tomographic reconstructions with SFDI ^{49,64}, we describe in this work the first use of Monte Carlo simulations conducted natively in the spatial frequency domain to make a two-layer LUT inversion algorithm that closely matches the true physiology and optical characteristics of preclinical tumor models. First, we describe the Monte Carlo simulation parameters and methods used to generate a two-layer LUT. We then compare its performance to two different homogeneous LUTs. We then validate the two-layer LUT algorithm using experimental measurements made on custom two-layer tissue-simulating phantoms. Next, we conduct a sensitivity analysis to determine how sensitive the two-layer LUT is to imperfect knowledge of the top (skin) layer parameters, including optical properties and layer thickness. Then, we utilize the two-layer LUT to re-analyze an *in vivo* data set from a previously published longitudinal treatment monitoring study, and compare the results to those obtained with a homogeneous LUT ⁵². Finally, we conclude this section by discussing the advantages and limitations of the new two-layer methodology, and its potential for future applications in preclinical oncology.

3.2 Materials and methods

3.2.1 Monte Carlo simulations for the generation of LUT-based inverse models

3.2.1.1 Prior work and the implementation of the Gardner method for estimating R_d in the spatial frequency domain

Several prior publications from our group and others have utilized a two-frequency LUT inversion algorithm to extract optical properties from SFDI-derived R_d values ^{42,52,57,73}. At the core of this LUT algorithm is a single conventional MC simulation for a semi-infinite

homogeneous medium. The simulation results are post-processed to provide R_d values for arbitrary μ_a and μ'_s combinations using the methods described in Martinelli et al. ⁷⁴. A discrete Hankel transform is then used to transform the spatially resolved R_d values to the spatial frequency domain. A LUT is constructed by scaling (i.e., post-processing) the MC results for a desired range and step size of μ_a and μ'_s values. In this work, a linear interpolation method is then implemented using Matlab's "griddata" function, whose input is measured R_d values and the LUT, and whose output is best fit optical properties.

This method has several limitations. First, the scaling method in Martinelli et al. is only described for homogeneous media, thus making it currently inapplicable for modeling multi-layer tissue geometries ⁷⁴. Additionally, the discrete Hankel transform is sensitive to discretization errors, which may lead to inaccuracies and artifacts depending on the density of the spatial sampling used ⁷⁵. A new method for obtaining multi-layer MC results in the spatial frequency domain was recently described by Gardner et al. ⁷⁵. The Gardner method obtains R_d estimates natively in the spatial frequency domain and is therefore not subject to the same discretization errors caused by taking a discrete transform of spatially resolved R_d . The Gardner method computes a frequency-dependent photon weight, as shown in Eq. 3.1, for a two-layer medium and a spatially modulated source in the x-direction:

$$W_n = \exp(-\mu_{a,1}d_{1,n} - \mu_{a,2}d_{2,n})\exp(-2\pi if_x x_n). \quad (3.1)$$

This expression was obtained by taking the spatial Fourier transform of the time-independent radiative transport equation over the transverse directions (i.e. x and y dimensions). It provides the final weight of the n -th detected photon originating from a point source at $x_o = 0$ with unity initial weight. Here, $d_{i,n}$ stands for the total photon path

length in the i -th layer, and subscripts 1 and 2 refer to the top and bottom layers, respectively, of the two-layer tissue model. In addition to the effect of absorption (first exponential term), as in the case of a conventional continuous absorption-weighted MC simulation, the photon weight exhibits the effect of spatial modulation as a frequency-dependent phase accumulation (second exponential term), which is sensitive only to the net lateral displacement (x_n) of the photon's exit location relative to the source. Equation 3.2 can then be used to compute R_d as a function of f_x , where N is the total number of photons simulated:

$$R_d(f_x) = \frac{1}{N} \sum_{n=1}^N W_n. \quad (3.2)$$

Provided that $d_{1,n}$, $d_{2,n}$, and x_n are stored, it is possible to compute R_d for various spatial frequencies and μ_a values from a single MC simulation. This method of scaling for μ_a is more accurate than applying Beer's law to R_d ^{68,74}. A separate MC simulation must be run to obtain results for each μ'_s value of interest.

In this work, we compare R_d and optical property extractions from LUT inverse models based on both the conventional MC simulations scaled with the methods described in Martinelli et al., as well as MC simulations conducted with the methods described in Gardner et al. For convenience, we will refer to the MC methods used to generate LUTs as either the "Martinelli method" or "Gardner method". Similarly, the different LUTs used to produce R_d and optical property extraction will be referred to as "Martinelli homogeneous," "Gardner homogeneous," and "Gardner two-layer."

3.2.1.2 Monte-Carlo simulation parameters for generating homogeneous and two-layer LUTs

The Martinelli method was used to construct a homogeneous LUT, and the Gardner method was used to construct both a homogeneous LUT and a two-layer LUT. The geometries of the MC simulations used to produce these LUTs are shown in Fig. 3.1A and Fig. 3.1B. Both models were constructed for the purpose of extracting optical properties from a subcutaneously implanted tumor on the mouse flank. For the homogeneous case, the tumor was modeled as a semi-infinite geometry, and the effects of the superficial skin layer were ignored. For the two-layer case, the top layer represents the skin layer, with fixed (i.e. known) μ_a , μ'_s and thickness (d), and the bottom layer represents a semi-infinite tumor layer. For all LUTs, the tumor optical properties are the free parameters of the inversion algorithm. Below we describe the properties of each layer in more detail.

Skin layer: Optical properties of the upper (skin) layer of the MC simulations were adapted from Sabino et al. ⁷⁶, who recently reported μ_a and μ'_s of skin from BALB/c male mice using a Kubelka-Munk model of photon transport and spectrophotometric measurements for the wavelength range of 400 - 1400 nm. The authors used skin from the mouse dorsal region and shaved any excess hair before measurements. We utilized the average μ_a and μ'_s values of the reported skin properties calculated over the four SFDI wavelengths (659, 691, 731 and 851 nm) for the upper layer properties in our two-layer MC simulations: $\mu_a = 0.096 \text{ mm}^{-1}$ (SD: 0.0075 mm^{-1}) and $\mu'_s = 0.78 \text{ mm}^{-1}$ (SD: 0.12 mm^{-1}).

The thickness of the skin layer was estimated using caliper measurements of eight

excised tumor skin samples from C57BL/6N female mice. The average skin thickness, which included the epidermis, dermis, and hypodermis, was 312.5 μm . H&E staining of representative tumor skin cross sections was conducted to validate this skin thicknesses (agreement was within 3.1 % for $n = 2$ samples). The C57BL/6N mouse strain was used to estimate thickness since it is commonly used for mouse tumor imaging ⁷⁷ and we plan to utilize this strain in future studies of mammary carcinoma. Our thickness measurements were similar to past reports of C57BL/6N skin thickness, where female mice were found to have a skin thickness of 371 μm ⁷⁸, 300 μm ⁷⁹, and 364 μm ⁷⁶. We note that data collected from male SCID mice were used in section 3.3.5 of this chapter as well as in our prior study in chapter 1 ⁵². The thickness of male SCID mouse skin was determined by measuring 18 skin samples taken prior to treatment ($n = 6$), during treatment with either DC101 or CPA ($n = 6$), and after treatment ($n = 6$) using brightfield microscopy of frozen tissue sections. The average skin thickness was found to be 326.9 μm , which is within 5 % of the thickness used in the two-layer model (312.5 μm). The difference between the thickness of samples taken before and during or after treatment was within 11 %. These results suggest the two-layer model is appropriate for subcutaneous tumor models in both female C57BL/6N and male SCID mice. Other mouse strains have somewhat similar skin thickness, including the commonly used BALB/c mouse strain (336 μm for female and 393 μm for male) ⁷⁶, immunocompetent albino mice (441 μm) ⁸⁰, immunocompromised athymic Nude mice (420 μm) ⁷⁹, and female SCID mice (220 μm) ⁸¹.

Tumor layer: In all three LUTs, the bottom (tumor) layer contains 400 μ_a values, ranging from 0.0005 to 0.2 mm^{-1} ($\Delta\mu_a = 0.0005 \text{ mm}^{-1}$) and 192 μ'_s values ranging from 0.1

to 3.58 mm^{-1} ($\Delta\mu'_s = 0.018 \text{ mm}^{-1}$). A separate MC simulation was run for each μ'_s value for both the homogeneous and two-layer Gardner LUTs. The tumor layer depth in all simulations was set to be at least 20 times the maximum l^* ($= 1/[\mu_a + \mu'_s]$) to mimic a semi-infinite tissue geometry, where l^* was determined using the lowest μ_a value (0.0005 mm^{-1}). Based on this criterion, a tumor layer thickness of 100 mm was used for all MC simulations except for the lowest sixteen μ'_s values (0.1 to 0.37 mm^{-1}), for which the thickness was increased to 200 mm.

3.2.1.3 Monte Carlo simulations at Boston University Shared Computer Cluster (SCC)

All MC simulations were conducted at the Boston University SCC located in Holyoke, MA. Previously developed command-line implementation of the Gardner method was used for the MC simulations (software developed by and implemented with the assistance of the Virtual Photonics Technology Initiative at the Beckman Laser Institute, University of California, Irvine). In all simulations and for both layers, the index of refraction and anisotropy factor (g) were set to 1.4 ²⁶ and 0.9 ⁸² respectively, except for simulations performed in Sec. 3.3.1, in which the index of refraction and g for both layers were set to 1.33 and 0.71 , respectively to match those used in Cuccia et al.⁵⁵. We launched 1×10^7 photons for each simulation⁵⁵. A total of 192 MC simulations were conducted to generate the Gardner LUTs, one for each μ'_s value of the tumor layer. In these 192 simulations, μ_a was set to a value of 0.0005 mm^{-1} for the tumor layer. The 192 simulations were divided into 12 groups, each with 16 simulations which were run in parallel. Each MC simulation required 2 CPUs, and runtime was dependent on optical properties and ranged from 2.5 – 4 days. The total photon path length in each layer and the photon exit position were stored

for each simulation. The results from each simulation were post-processed using Beer's law (as in Eq. 3.1) to achieve results for all values of μ_a . Post-processing runtime was 2 - 3 days, depending on the specific optical properties.

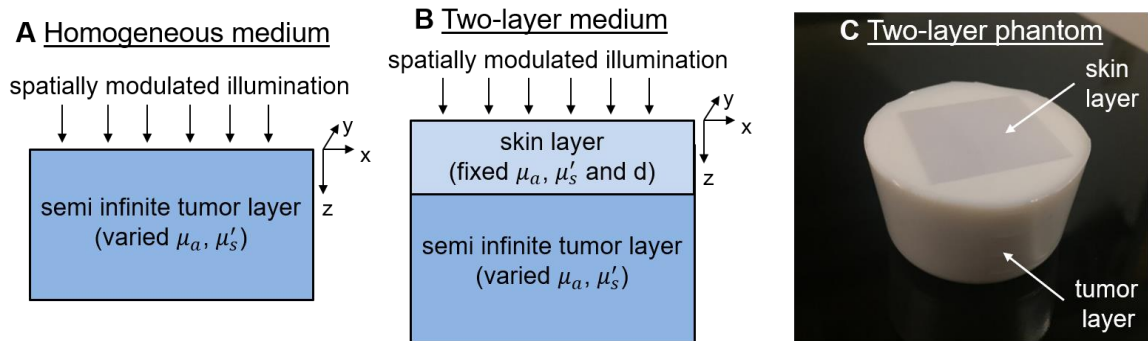


Figure 3.1: A, Schematic of tissue model for the homogeneous case. B, schematic of the tissue model for the two-layer case. C, an example of a custom-made two-layer silicone phantom used to validate the accuracy of the resulting two-layer inverse algorithm.

3.2.2 Two-layer tissue-simulating optical phantoms

A set of two-layer solid silicone phantoms was fabricated to optically simulate subcutaneous tumors in a mouse with a range of optical properties. These phantoms were used to test the accuracy of the Gardner LUT inversion algorithms. The phantoms consisted of a thin skin layer above a tumor layer. The top layer thickness and optical properties were fabricated to closely match the parameters described for MC simulations in Sec. 3.2.1. Four different two-layer phantoms were fabricated, all of which used the same skin layer. In all phantoms, silicone was used as the base solvent, nigrosin as the absorber, and titanium dioxide as the scatterer. The optical properties of the phantoms were adjusted by varying the amount of absorber and scatterer during fabrication as described in previously⁸³.

The thin upper layer phantom was made by adapting a previously described

technique⁸⁴. First, an aluminum phantom mold was fabricated by machining a well that was 330 μm in depth and 1.5" by 1.5" in the lateral dimensions using a computer-controlled milling machine (SV-2414S-M, Sharp Industries). After the phantom ingredients were mixed together, the liquid mixture was poured into the aluminum mold. A microtome blade was used to draw and spread the mixture evenly across the well, and the edges of the blade remained in contact with the top surface of the mold at all times. The phantom was then left to cure, uncovered, overnight. During curing, the silicone layer was observed to shrink in the center of the well. Once cured, the thin silicone layer was removed from the mold and cut to the size of 1" by 1" to remove the uneven and thicker edge. The thickness of the phantom was confirmed using caliper measurements by confining the thin layer between two microscope slide coverslips for stability and consistency. Because the top layer phantom was too thin for accurate optical property measurements with diffuse imaging techniques, a much larger, 2.5 cm thick homogeneous phantom was made from the same batch of material and SFDI was used to extract the optical properties.

Similarly, for the bottom (tumor) layer, four homogeneous phantoms were fabricated in collaboration with Dr. Muldoon's group⁸⁵ and measured with SFDI. The thickness of each phantom was 2.5 cm, and the μ_a and μ'_s values of each phantom were targeted to span known mouse tumor optical properties. The skin layer and tumor layer phantoms were stacked to create the two-layer phantoms. First, the thin skin layer phantom was cleaned using an alcohol wipe. Then, a small amount of ethanol was poured on a thick tumor layer phantom, and the thin layer was directly placed on top of the tumor layer, making sure that no visible air bubbles remained. The two-layer phantom was left under

the chemical hood overnight to allow the ethanol to evaporate without leaving any air pockets between the layers. An example of one of the two-layer phantoms is shown in Fig. 3.1C. The procedure was repeated 4 times to generate the four two-layer phantoms.

3.2.3 Longitudinal monitoring of a mouse tumor xenograft during cancer treatment

In chapter 1, we conducted SFDI longitudinal monitoring of the PC3/2G7 prostate tumor xenograft model during treatment with anti-cancer agents⁵². We have reprocessed a portion ($n = 2$ mice) of this longitudinal data using the new LUT inversion algorithms presented in this work in order to visualize the effect of using the multi-layer model in a relevant physiologic system. Details of the animal and tumor model, tumor cell preparation, tumor cell inoculation, animal handling and care, treatments schedule and dosing, and SFDI image acquisition and processing and tumor ROI selection can be found in chapter 1. All animal procedures and measurements were conducted under an institutionally approved protocol.

3.3 Results

3.3.1 Comparison between MC simulation results and LUT inversion algorithms: R_d

We first compared the results of the three different MC simulations methods (i.e. Martinelli homogeneous, Gardner homogeneous, and Gardner two-layer) and then compared how the LUT inversion algorithms based on these simulations differently map R_d values to optical property values.

Figure 3.2 shows an illustrative example of the differences and similarities in the MC simulation results. R_d is shown as a function of f_x for varying l^* values at a constant

ratio of $\mu'_s/\mu_a = 100$. The optical properties corresponding to each l^* value are as follows: For $l^* = 0.5$ mm: $\mu_a = 0.0198$ mm⁻¹, $\mu'_s = 1.98$ mm⁻¹; $l^* = 1$ mm: $\mu_a = 0.0099$ mm⁻¹, $\mu'_s = 0.99$ mm⁻¹; $l^* = 2$ mm: $\mu_a = 0.005$ mm⁻¹, $\mu'_s = 0.5$ mm⁻¹; and $l^* = 4$ mm: $\mu_a = 0.0025$ mm⁻¹, $\mu'_s = 0.25$ mm⁻¹. For the two-layer simulations, the skin layer properties were as previously described ($\mu_a = 0.096$ mm⁻¹, $\mu'_s = 0.78$ mm⁻¹, $d = 312.5$ μ m). From Fig. 3.2, it is evident that there is very little difference in MC simulation results between the Martinelli homogeneous and the Gardner homogeneous methods. However, the incorporation of the skin layer introduces a significant alteration in these results, as expected. Note that the effect of the skin layer is to sometimes shift R_d values higher than the homogeneous results and to sometimes shift them lower. This effect is dependent on spatial frequency as well as the specific optical properties of the tumor and skin layers. Because the Martinelli and Gardner homogeneous results are nearly identical, the remainder of the analysis will focus on the Gardner homogeneous and Gardner two-layer MC results and the LUT inversion algorithms based on these results.

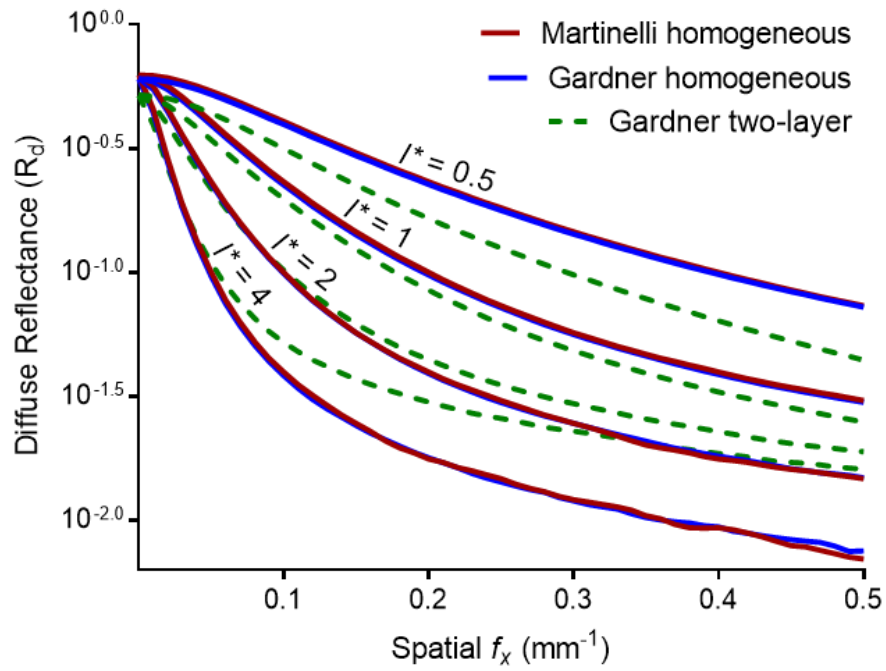


Figure 3.2: Comparison of Monte Carlo simulation results from the Martinelli homogeneous, the Gardner homogeneous and the Gardner two-layer methods. Diffuse reflectance (R_d) is shown as a function of spatial frequency (f_x) for varying values of l^* at a constant ratio of $\mu'_s/\mu_a = 100$. The Martinelli homogeneous and Gardner homogeneous results are nearly identical, while the introduction of the top (skin) layer introduces significant shifts in R_d that are dependent on f_x and the l^* of the bottom (tumor) layer.

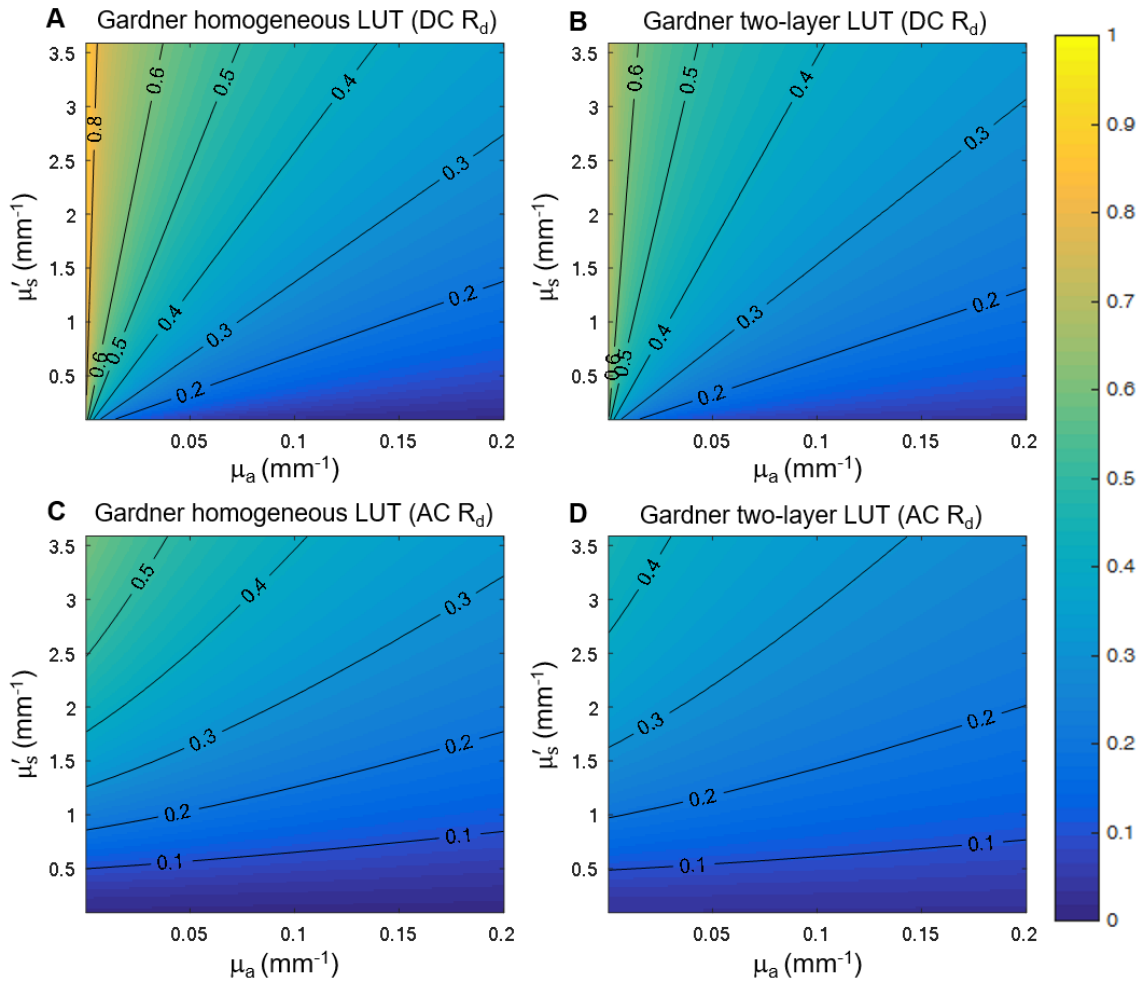


Figure 3.3: Comparison of LUT inversion algorithms based on Gardner homogeneous and Gardner two-layer methods. R_d values are shown both in the color dimension and as labeled isolines for the entire range of simulated μ_a and μ'_s values. A and B show optical properties versus DC R_d for the homogeneous and two-layer LUTs respectively. C and D show optical properties versus AC R_d for the homogeneous and two-layer LUTs respectively.

Figure 3.3 shows differences between the Gardner homogeneous and Gardner two-layer LUT inversion algorithms for two spatial frequencies: $f_x = 0 \text{ mm}^{-1}$ (DC R_d) and 0.1 mm^{-1} (AC R_d). Here, the x-axis displays μ_a , the y-axis displays μ'_s , and the color axis displays R_d . Isolines of constant R_d are displayed as an aid to visual comparisons between the subplots. As shown in Fig. 3.3, these plots visually show the substantial impact that the

skin layer has on the mapping between diffuse reflectance and optical properties.

3.3.2 Comparison between LUT inversion algorithms: optical property extraction

In practice, the LUT inversion algorithms accept experimentally measured R_d values as inputs and provide optical property extractions as outputs. We investigated the extent to which the LUTs provide different optical property extractions for the same input measurements (i.e. R_d values). To do this, we first chose 30 DC R_d values evenly spaced between 0.0419 - 0.749, and 30 AC R_d values, evenly spaced between 0.0289 - 0.4514. This range of R_d values was chosen as they are present in both the homogeneous and two-layer LUTs. For all combinations of the chosen DC and AC R_d values, μ_a and μ'_s were extracted using both LUTs, and the difference in μ_a and μ'_s extractions was computed. Absolute differences in optical properties between the LUTs are shown in Fig. 3.4A and Fig. 3.4C for μ_a and μ'_s , respectively, and the percent differences (relative to the homogeneous LUT values) are shown in Fig. 3.4B and Fig. 3.4D. For some DC and AC R_d combinations, the differences in optical property extractions are substantial. For example, from Fig. 3.4B, we see that percent differences for μ_a are larger (approximately 60 – 80 %) at higher DC R_d values. In Fig. 3.4D, larger differences in μ'_s extractions occur at higher AC R_d values. This analysis shows that the two LUTs differently map optical properties from R_d inputs. In the following section we demonstrate that the two-layer LUT improves the accuracy of tumor layer extractions.

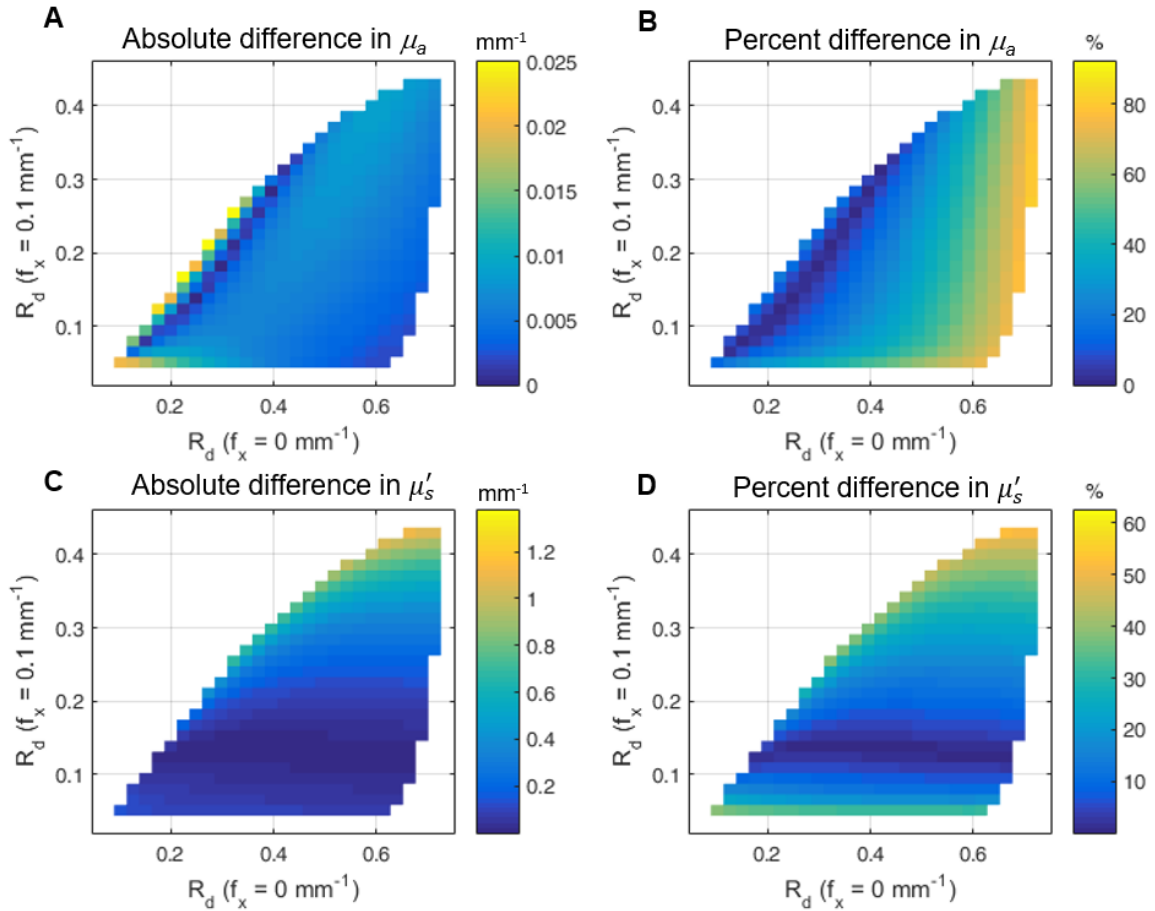


Figure 3.4: The impact on optical property extractions of the Gardner two-layer LUT inversion algorithm shown as absolute and % differences compared to the Gardner homogeneous case. A, Absolute and B, percent differences in μ_a extractions. C, Absolute and D, percent difference in μ'_s extractions.

3.3.3 The two-layer LUT improves the accuracy of tumor layer optical property extractions using SFDI

Experimental measurements were conducted to determine if the Gardner two-layer LUT inversion algorithm improves the accuracy of tumor layer optical property extractions compared to the Gardner homogeneous LUT. This accuracy test utilized the four two-layer phantoms described in Sec. 3.2.2. Each of the two-layer phantoms used the same top (skin) layer. The measured thickness of the skin layer was 310 μm at its center, which is within

0.8 % of the skin layer thickness defined in the MC simulations used to generate the Gardner two-layer LUT. Absorption of the skin layer was 0.0936 mm^{-1} at 659 nm, which is within 2.52 % of the MC absorption parameter, and the μ'_s value was 0.780 mm^{-1} at 659 nm, which is within 0.063 % of the MC value. For the tumor layer, four different pairs of optical properties were utilized, spanning a range of optical properties observed in our prior work in which we monitored PC3/2G7 mouse xenografts over 45 days using SFDI⁵². These pairs are labelled as tumor 1 through tumor 4 in Fig. 3.5. The optical property pairs, reported at 659 nm, are as follows: For tumor 1: $\mu_a = 0.0244 \text{ mm}^{-1}$ and $\mu'_s = 2.054 \text{ mm}^{-1}$; tumor 2: $\mu_a = 0.002 \text{ mm}^{-1}$ and $\mu'_s = 2.314 \text{ mm}^{-1}$; tumor 3: $\mu_a = 0.0039 \text{ mm}^{-1}$ and $\mu'_s = 0.714 \text{ mm}^{-1}$; and tumor 4: $\mu_a = 0.0301 \text{ mm}^{-1}$ and $\mu'_s = 0.676 \text{ mm}^{-1}$.

Each two-layer phantom was measured with SFDI, and the bottom (tumor) layer optical properties were extracted using both the Gardner homogeneous and Gardner two-layer LUTs. Since these phantoms have flat surfaces, no corrections for height or angle were implemented. The absolute differences between the measured and true μ_a for the tumor layer are shown in Figs. 5A and 5B. The absolute differences between the measured and true μ'_s for the tumor layer are shown in Figs. 5C and 5D. In both cases, the right subfigures (i.e. 5B and 5D) recapitulates the data in the left subfigures (i.e. 5A) and 5C) but with a zoomed-in y-axis to allow visualization of the small error values obtained for some phantoms. Table 3.1 shows the percent error in tumor layer optical property extractions for both the homogeneous and two-layer LUTs. In the worst case, the μ_a and μ'_s extraction errors were 20.33 % and 10.87 % for the two-layer LUT.

In all cases, the error in tumor layer optical property extraction is substantially lower for the two-layer LUT versus the homogeneous LUT. This effect is not as pronounced in μ'_s for tumors 3 and 4, as μ'_s values in these tumors are very similar to that of the skin layer ($\mu'_s = 0.78 \text{ mm}^{-1}$). Note that the decrease in error by the two-layer LUT is between 7 to 256 times for μ_a and between 2 to 24 times for μ'_s . Taken together, these results confirm that the two-layer LUT provides a better estimate of the true tumor layer optical properties than the homogeneous LUT.

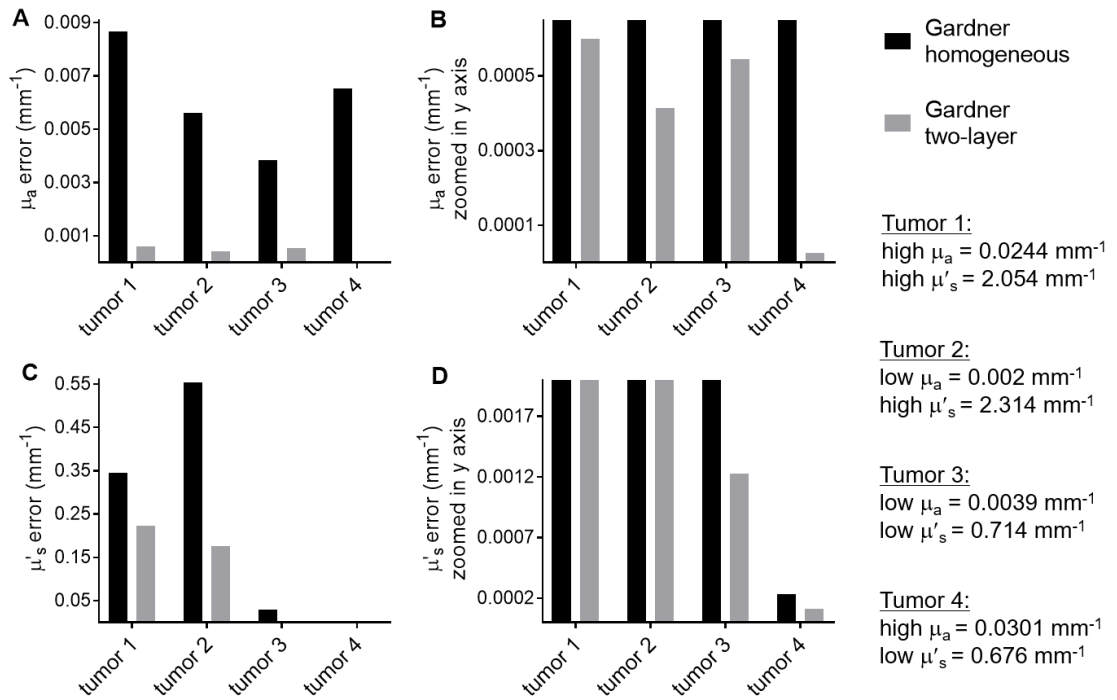


Figure 3.5: Comparisons in bottom (tumor) layer optical property extraction errors for the Gardner homogeneous and Gardner two-layer LUT inversion algorithms. Diffuse reflectance measurements of four two-layer tissue simulating optical phantoms were made with SFDI, and both inversion models were used to extract the bottom (tumor) layer optical properties (labeled as tumor 1 - 4). A shows the absolute extraction error compared with the known tumor layer μ_a . B shows the same data but with a zoomed-in y-axis so that small extraction errors can be visualized. C shows absolute errors in tumor layer μ'_s extractions and D shows the same data with a zoomed-in y-axis. Optical properties were measured at 659 nm.

	% error			
	μ_a		μ'_s	
	homogeneous	two-layer	homogeneous	two-layer
tumor 1	35.45	2.46	16.77	10.87
tumor 2	277.03	20.33	23.98	7.62
tumor 3	97.72	13.88	4.05	0.17
tumor 4	21.65	0.08	0.03	0.02

Table 3.1: Accuracy of optical property extractions in four two-layer tissue simulating optical phantoms. Each two-layer phantom is designated as tumor 1 - 4.

3.3.4 Sensitivity analysis of the two-layer LUT

We conducted a sensitivity analysis to characterize how mismatches in the skin layer optical properties and thickness affect the results of the Gardner two-layer LUT. Stated another way, the sensitivity analysis provides an indication of how well one must know the true skin layer properties in order to obtain accurate tumor layer optical property extractions. Additional MC simulations were conducted of a two-layer medium in which the properties of the skin layer (μ_a , μ'_s , d) were varied to introduce a mismatch to those used to generate the Gardner two-layer LUT. The skin layer μ_a value was varied by up to $\pm 40\%$ of the original Gardner two-layer value, μ'_s was varied by up to $\pm 40\%$, and d was varied from -40% to $+80\%$. Unlike optical properties, d was varied by up to $+80\%$ in order to simulate large skin thickness values, such as $d = 530\ \mu\text{m}$, reported previously in athymic nude mouse⁷⁹. For this analysis, four tumor layer optical property pairs were chosen to span a physiologically relevant range, and extraction errors are reported for each pair. The tumor layer optical property pairs at 659 nm are listed here: For tumor 1: $\mu_a = 0.031\ \text{mm}^{-1}$ and $\mu'_s = 2.025\ \text{mm}^{-1}$; tumor 2: $\mu_a = 0.004\ \text{mm}^{-1}$ and $\mu'_s = 2.2\ \text{mm}^{-1}$; tumor 3: $\mu_a = 0.005\ \text{mm}^{-1}$ and $\mu'_s = 0.676\ \text{mm}^{-1}$; and tumor 4: $\mu_a = 0.033\ \text{mm}^{-1}$ and $\mu'_s = 0.645\ \text{mm}^{-1}$.

In order to compute extraction errors induced by the mismatched skin layer, the R_d values at the DC and AC spatial frequencies produced from each of the new MC simulations (which each had mismatched skin layer properties) were fed to the original Gardner two-layer LUT and resulting optical property extractions were recorded. The absolute error was then computed, defined as the difference between the known tumor layer optical properties and the recorded optical property extractions. These errors are shown in Figs. 3.6A-F. As expected, the errors in μ_a and μ'_s extractions increase as the mismatch in skin layer properties increases. For example, as described Dodig et al. reported that female SCID mice had a skin thickness of approximately $220 \mu\text{m}$ ⁸¹. This is an approximately - 30 % mismatch with the skin thickness used for our model ($312.5 \mu\text{m}$). As shown in Figs. 6E and 6F, assuming the skin optical properties match, this - 30 % mismatch in skin layer thickness may induce an error in μ_a of as much as -0.0023 mm^{-1} and a μ'_s error of as much as 0.29 mm^{-1} (these are the worst-case errors observed from this analysis, substantially smaller errors were observed for some tumor optical property combinations).

Additional MC simulations were conducted in which the properties of the skin layer (μ_a , μ'_s , d) were varied simultaneously to explore the effect of combining these mismatches. The maximum errors observed when all three parameters were mismatched in the negative direction (i.e. all three parameters decreased by 40 %) was -0.0078 mm^{-1} for μ_a and 0.44 mm^{-1} for μ'_s . The maximum errors observed when all three parameters were mismatched in the positive direction (i.e. μ_a , μ'_s increased by 40 %, d increased by 80 %) was 0.021 mm^{-1} for μ_a and -0.51 mm^{-1} for μ'_s . Whether errors of this magnitude are tolerable depends on the specific application and biological questions posed.

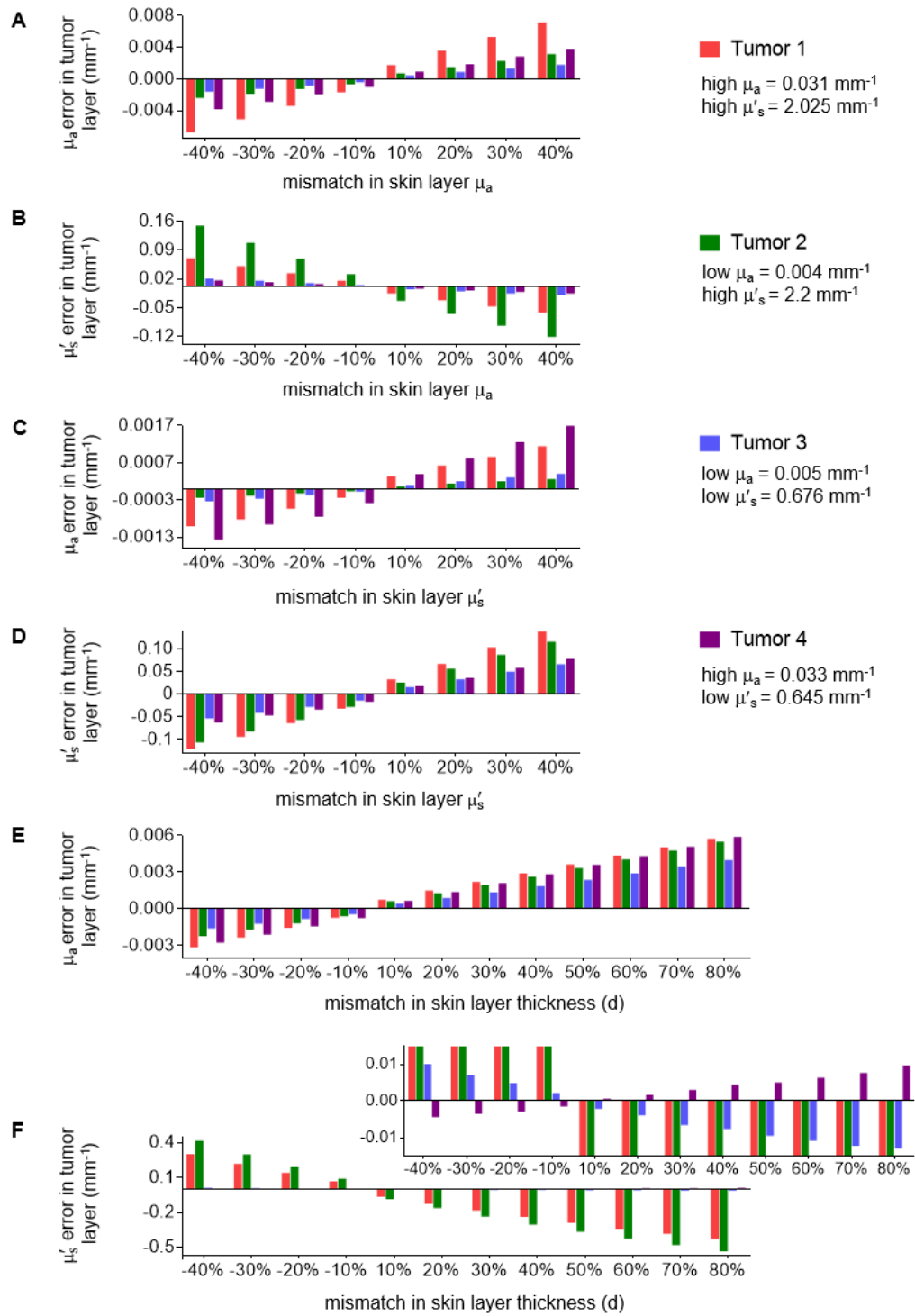


Figure 3.6: Results from a sensitivity analysis for the two-layer Gardner LUT inversion algorithm. Errors in tumor layer μ_a and μ'_s extractions are shown for various skin layer property mismatches A-F. In F, the inset image has a zoomed in y-axis. Optical properties were measured at 659 nm.

3.3.5 The Gardner two-layer LUT reveals larger therapy-induced optical scattering dynamics and a more hypoxic tumor environment during longitudinal monitoring of tumor xenografts

The homogeneous and two-layer LUT inversion algorithms were used to re-analyze a prior data set in which SFDI was used to monitor mice longitudinally during the course of anti-cancer therapy ⁵². The details of the data acquisition and analysis, including the methods for ROI selection, are described in detail in Tabassum et al. ⁵². Briefly, each SFDI measurement was repeated thrice and averaged to minimize breathing artifacts. The demodulated images were corrected for height and angle ⁵⁷. Two-by-two binning of the CCD was applied to improve the SNR. Mice were monitored longitudinally for a total of 45 days. R_d data acquired with SFDI were analyzed with both the Gardner homogeneous and Gardner two-layer LUT inversion algorithms for comparison.

Figure 3.7A shows changes in tumor μ'_s at 659 nm from a DC101-treated tumor over the course of 45 days. Injection dates are indicated by vertical dashed lines. The mean and standard deviation of μ'_s values extracted over a manually chosen ROI are shown. The two-layer LUT reveals higher μ'_s values throughout the study compared to the homogeneous LUT, and the changes in μ'_s over time are also larger. Figure 3.7B shows tumor μ'_s colormaps overlaid on a planar mouse image at day 0 and day 30 for both LUTs. The increase in μ'_s is apparent throughout the tumor region at these time points.

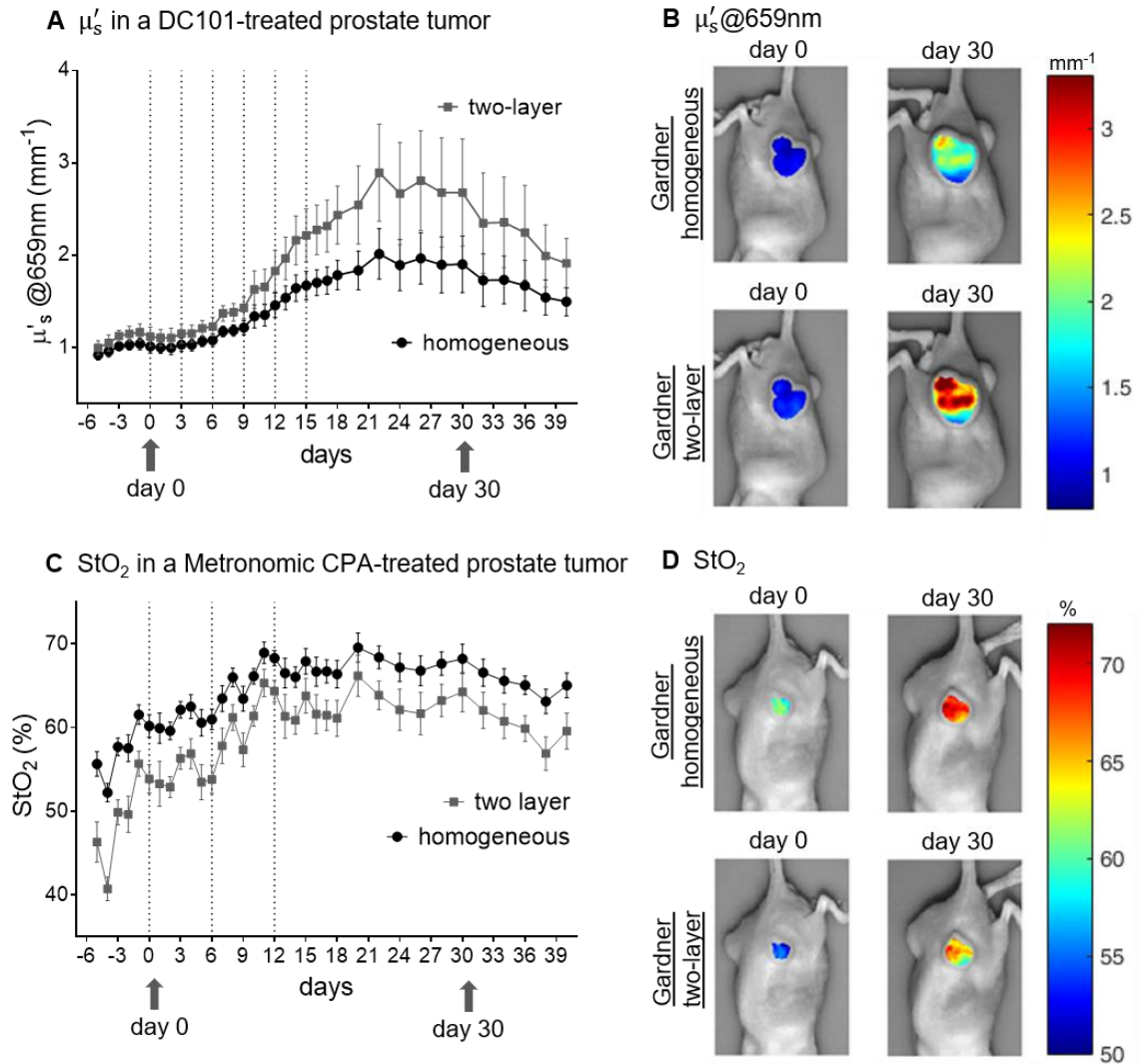


Figure 3.7: An example of the Gardner homogeneous and the Gardner two-layer LUT inversion algorithms applied to SFDI data collected during a longitudinal treatment monitoring study of PC3/2G7 prostate tumor xenografts. **A**, μ'_s extractions from both LUTs are shown during and after DC101-treatment. **B**, μ'_s colormaps overlaid on DC101-treated planar mouse images at day 0 and day 30. **A**, **B** plot mean with standard deviation over tumor ROI. **C**, StO_2 values determined using four wavelength optical property extractions from both LUTs for a CPA-treated tumor. **D**, StO_2 colormaps overlaid on CPA-treated planar mouse images at day 0 and day 30.

Figure 3.7C shows changes in tumor StO_2 from a CPA-treated tumor on a metronomic schedule, followed by a rebound period. Mean and standard deviation of StO_2 values extracted over a manually chosen ROI are shown. The two-layer LUT reveals lower

StO₂ values over the entire study period compared to the homogeneous LUT; the values decrease by roughly the same extent throughout the study. Figure 3.7D shows tumor StO₂ colormaps overlaid on planar mouse images at day 0 and day 30 for both LUTs. A decrease in StO₂ is apparent throughout the tumor region at these time points.

3.4 Discussion

In this work, a new two-layer LUT inversion algorithm was introduced to more accurately account for the tumor and skin layered physiology in a small animal oncology model when imaging with SFDI. The LUT was constructed using Monte Carlo simulation results conducted natively in the spatial frequency domain with the recently developed method by Gardner et al., which avoids the discretization errors associated with Fourier or Hankel transforming conventional spatially-resolved Monte Carlo results ⁷⁵. The two-layer tissue LUT was superior in its ability to extract both μ_a and μ'_s from the tumor layer, decreasing errors by as much as a factor of 256 for μ_a compared to a homogeneous LUT. The magnitude of the improvement was highly dependent on both the optical properties of the tumor layer and spatial frequencies considered. When applied to a longitudinal data set, the two-layer LUT revealed larger antitumor therapy-induced changes in tumors and a more hypoxic tumor environment.

One important characteristic of the two-layer model developed here is that the top (skin) layer optical properties and thickness (μ_a , μ'_s , d) were fixed rather than free parameters. Estimates for these parameters were based on a prior report of male BALB/c albino mice mouse skin optical properties and our own mouse skin thickness measurements ⁷⁶. Unfortunately, there are limited reports of mouse skin optical properties in the literature,

and skin thickness reports vary by mouse strain and gender^{76,79}. A sensitivity analysis was conducted to evaluate the impact of imperfect top layer assumptions on the extraction of bottom (tumor) layer optical properties. This analysis is useful for understanding the impact of using this two-layer LUT for mouse strains and genders with different optical properties or thicknesses, or for measurements in different wavelength regions. Care should be taken when this model is applied to other mouse strains and genders, as each application will have a different threshold for acceptable error.

The utility of the two-layer LUT was demonstrated by re-analyzing a prior longitudinal data set with the new model and comparing the results to a homogeneous LUT. The two-layer LUT revealed substantial differences compared to the homogeneous LUT during treatment with two anticancer therapies: DC101, a targeted antiangiogenic, and CPA, a cytotoxic agent. For example, larger increases in μ'_s (up to 2.75X) were observed in the DC101-treated tumor when analyzed with the two-layer LUT, and the optical contrast between pre- and post-treatment time points was enhanced significantly. In the CPA-treated tumor, the two-layer LUT revealed lower tumor StO₂ throughout the study, including before baseline, during treatment, and during a rebound period. In both of these scenarios, the differences between the two-layer and homogeneous results are presumably due to the fact that the two-layer LUT is better able to isolate the tumor layer optical properties, whereas the homogeneous LUT convolves the changes in the tumor layer with the skin layer. It is of note that in some cases the two-layer LUT provides better agreement with other reported tumor values compared with the homogeneous LUT. For example, the baseline StO₂ in the CPA-treated tumor was 60.2 % with the homogeneous LUT and 53.9

% with the two-layer LUT. In this case, the two-layer LUT StO₂ value better matches the StO₂ values of 40 - 55 % reported for K1735 malignant mouse melanoma subcutaneous tumors measured using diffuse reflectance spectroscopy ⁶².

There have been other reports of multi-layer inversion models for SFDI, but they have largely focused on clinical applications in human skin in which layer thicknesses, chromophores, and optical properties may be substantially different than those for mice. For example, Weber et al. developed an analytic two-layer model based on photon diffusion theory in the spatial frequency domain ⁶⁹. The model had five fit parameters (i.e. top and bottom layer μ_a , μ'_s , and top layer thickness), and provided bottom layer μ_a extractions with an accuracy of 25 % when the top layer thickness was constrained to within 25 % of the true value. This model was tested for top layer thicknesses of 2 - 4 mm, which are substantially larger than the 312.5 μm top layer thickness used in the present work. Saager et al. utilized Hankel-transformed conventional (i.e. spatially resolved) Monte Carlo simulations to develop a two-layer model of human epidermis (containing melanin) and dermis (containing melanin and hemoglobin) ^{70,86}. This model also provides estimates for top layer thickness constrained within a range of 80 - 300 μm . Yudovsky et al. also utilized Hankel-transformed conventional Monte Carlo to create a two-layer model of human skin, with special attention to skin pigmentation and epidermal thickness ^{72,87}. The authors used the Monte Carlo results to train an artificial neural network in order to develop their inversion algorithm. The work presented here differs from these prior works in that the model parameters were specific to small animal tumor models, and the Monte Carlo simulations used to generate the LUT-based inversion model were conducted

natively in the spatial frequency domain.

While this work demonstrated that a two-layer LUT model improves the optical property extraction accuracy of the bottom (tumor) layer for a mouse tumor model, there are some limitations that the reader should bear in mind. For example, it is currently unknown to what extent skin optical properties or thickness changes during treatment in different mouse tumor models, which could affect the ability to accurately extract tumor optical properties. Additionally, as previously discussed, this model assumed a fixed set of upper layer optical properties and thickness. This limits the applicability of the two-layer LUT to substantially different mouse models and different wavelength ranges. It is of note that the general methodology described here can be utilized to construct multi-layer LUTs for other SFDI applications, including for different mouse models or clinical applications with different layer thicknesses and optical property ranges, but this requires additional MC simulations and data post processing. An additional limitation is that the two-layer model only accounted for skin as a single layer, whereas a more complex model might include separate epidermis, dermis, and hypodermis layers in addition to the tumor layer. It is conceivable that a more complex layered model would improve optical property extraction accuracy, but there are challenges associated with isolating and measuring the optical properties of each of these layers for use as fixed model parameters. It is possible to allow upper layer thickness and optical properties to be free parameters in the inverse model, but this substantially increases the solution space and may reduce the ability to accurately extract bottom-layer optical properties⁶⁹. It can also lead to underdetermined problems⁷². Finally, we reported results only for spatial frequencies of DC and 0.1 mm^{-1} .

While the Monte Carlo results can be post-processed for arbitrary spatial frequencies, the choice to use this frequency pair was made based on our recent work utilizing Cramér-Rao lower bounds to determine optical property uncertainty estimates for SFDI⁷³. This analysis revealed DC and 0.1 mm^{-1} as excellent choices to reduce optical property extraction uncertainty for similar optical property ranges.

3.5 Conclusions

In conclusion, the two-layer LUT model presented was shown to substantially improve the ability of SFDI to extract bottom (tumor) layer optical properties, and this revealed larger treatment changes in tumor optical properties and a more hypoxic tumor environment in a mouse tumor model. Since therapy-induced optical changes may be subtle for some drugs and tumor models, the ability of the two-layer LUT to provide more accurate and enhanced pre- and post-treatment tumor contrasts may substantially increase the utility of SFDI as a preclinical imaging tool for monitoring cancer treatments.

CHAPTER FOUR

Early chemotherapy and antiangiogenic response revealed by tumor optical scattering using label-free Spatial Frequency Domain Imaging

The work in Chapter Four will be submitted to a cancer journal with the following contributing authors:

Syeda Tabassum¹, Anup Tank², Fay Wang², Cameron Vergato³, Kavon Karrobi², David J. Waxman³, and Darren Roblyer²

¹Electrical and Computer Engineering, Boston University, Boston, Massachusetts

²Biomedical Engineering, Boston University, Boston, Massachusetts

³Division of Cell and Molecular Biology, Department of Biology and Bioinformatics Program, Boston University, Boston, Massachusetts

4.1 Introduction

Surveillance of *in vivo* tumor state with methods that can detect chemotherapeutic response and resistance may help to maximize overall treatment efficacy while sparing patients from the cost and burden of overtreatment. Unfortunately, current standard of care imaging tools (e.g., MRI, PET/CT, mammography, ultrasound) have been shown to be limited in their ability to monitor treatment response in solid tumors^{15,23,24}. Over the last decade clinical Diffuse Optical Imaging (DOI) techniques have emerged as a powerful alternative to these techniques. DOI provides a metabolic and molecular profile of tumors while being label-free, non-invasive, safe, and generally low cost^{25,28,30,35,88}. Although prior efforts have been

made to correlate *in vivo* DOI clinical measurements with histopathology results from clinical biopsies or surgical specimens^{36,37}, obtaining tissue samples during treatment remains a challenge in the clinic. Alternatively, the preclinical setting provides opportunities for testing new treatment regimens in well characterized tumor models and patient derived xenografts while simultaneously allowing better access to tumor tissue samples for histological correlations. This provides a means of placing DOI metrics in a biological context for a variety of treatment strategies. Preclinical optical monitoring also makes it possible to correlate clinically observed DOI parameters with underlying tumor and host biology at the cellular and molecular levels, during treatment with a wide variety of drug regimens or combination treatments.

In this work we sought to accomplish two goals: 1.) investigate the biological correlates of SFDI optical and functional metrics, and 2.) characterize the ability of SFDI to identify early optical markers of treatment response. We first demonstrated that SFDI can track both absorption and scattering based contrast in a prostate xenograft model in response to a cytotoxic and an antiangiogenic treatment for over one month. We next show correlation between SFDI metrics and tumor physiological markers by immunohistochemical analysis in a cross-sectional large-scale animal study. We focused on optical scattering as a marker of treatment response since prior work has linked optical scattering and micro-architectural changes in cellular density and size and thus cellular death and proliferation⁸⁹⁻⁹¹. Tumor markers of apoptosis, proliferation, vessel density, glucose uptake, macrophage, and vessel patency are analyzed.

While the clinical studies with DOI so far have largely focused on absorption based

parameters like hemoglobin, water and lipid^{28,30,35,88}, only recently has SFDI enabled the ability to measure optical scattering over a wide field⁶⁴. Here we show that optical scattering is able to provide substantial contrast in treated versus controls at early timepoints during treatment, and that specific changes in scattering are highly correlated to apoptosis and proliferation. We also show results from a classification analysis that optical scattering along with tumor anatomic information, can provide a very strong predictive ability for both cytotoxic and antiangiogenic treatments. Together, these results suggest that optical scattering with DOI may be an underappreciated imaging biomarker for treatment response monitoring.

4.2 Materials and Methods

4.2.1 SFDI data acquisition and processing

Descriptions of SFDI instrumentation, data acquisition and analysis are similar to those described in section 2.2.1, 2.2.7 and 3.2.3 and references (1,2), except for several differences in image processing that will be described here. Here, tumor regions of the images were segmented, and edge artifacts were removed using a combination of automated and manual segmentation steps. First an area of interest was manually chosen over the tumor using the μ_a map; pixels at the extreme edge of the tumor were excluded due to edge effects⁵². An automated mask was then applied to the area of interest in order to exclude pixels on the tissue surface greater than 40° relative to the camera axis⁵². Finally, pixels with very low μ_a values ($\mu_a < 0.0001 \text{ mm}^{-1}$) were excluded and any remaining minor artifacts at the tumor edge were manually removed. Lastly, a manual mask was applied to the tumor region to remove extreme edge artifacts at the tumor periphery.

4.2.2 Cell lines, animals, and treatment details

Details of preparation and inoculation of the PC3/2G7 prostate tumor xenograft model can be found in sections 2.2.6 and 3.2.3 of the previous chapters. Briefly, in this chapter, severe combined immunodeficient (SCID) hairless outbred mice (SHO-*Prkdc^{scid}Hr^{hr}*), 5 to 6 weeks old male (21-23 gram), were purchased from Charles River Laboratories, and housed in the Boston University Laboratory Animal Care Facility in accordance with an institutionally approved protocol (IACUC 16-003) and federal guidelines. Tumor length (L) and width (W) were measured throughout the study using digital calipers every 2 or 3 days. Mice bearing PC3/2G7 tumors were assigned to three groups once the average group TV reached $\sim 500 \text{ mm}^3$. Mice were treated with either cyclophosphamide (CPA) or DC101 (both given intraperitoneally) or left untreated as control. Mice were given CPA on a metronomic schedule at a dose of 140.3 mg/kg every 6 days for 3 cycles. DC101 was administered at a dose of 28.6 mg/kg every 3 days for 6 cycles. An additional imaging experiment was conducted where syngeneic E0771 tumors were grown in 6 weeks old (15-18 g) female C57BL/6 mice purchased from Taconic Biosciences (model B6-F, Rensselaer, New York) under an institutionally approved protocol (IACUC 16-013). E0771 cells were grown in RPMI 1640 media supplemented with 10% fetal bovine serum and 1% penicillin/streptomycin under 37C 5% CO₂ conditions. Immediately prior to inoculation, cells were collected via trypsinization, washed and subsequently resuspended in PBS. Prepared cells were stored on ice until injection. 2×10^5 cells in 100 μ L PBS were implanted in the fourth mammary fat pad of each mouse. TV was measured every 3 days. Mice were randomized to 3 groups, Control, CPA and DC101, as average TV reached $\geq 250 \text{ mm}^3$.

CPA was administered on a metronomic schedule at a dose of 130 mg/kg every 6 days for 2 cycles. DC101 was administered at a dose of 40 mg/kg every 3 days for 3 cycles. The Control group received non-specific mouse IgG (mIgG) (Jackson Immuno Research Laboratories) solutions at a dose of 40 mg/kg every 3 days for 3 cycles. All treatments were implemented via intraperitoneal injections. During SFDI measurements, all mice were anesthetized using isoflurane by inhalation (5% induction). Although we have not tested the effects of isoflurane on SFDI parameters, a prior study using Diffuse Reflectance Spectroscopy (DRS), a point probe DOI tool which is similar to SFDI, showed that decreases in THC, StO₂, and HbO₂ occurred with increasing isoflurane concentrations, while having no effect on μ'_s ⁹². Mice were euthanized using cervical dislocation according to the approved protocols.

4.2.3 Longitudinal Monitoring with SFDI

SCID mice bearing PC3/2G7 tumors were monitored longitudinally with SFDI for 22 days of initial tumor growth + 27 days after the start of treatment. Mice were imaged every 3 days during tumor growth, twice every 3 days during the 18 days of treatment, and every 3 days following treatment in the rebound period. Some mice were monitored longer (up to 69 days after the start of treatment) for the purposes of movie visualizations. Mice were allocated to three groups at the start of treatment: Control, CPA and DC101. Several mice from each group were euthanized for tissue analysis at days 0, 1, 9, 18, and 26. Tumors were frozen or fixed for cross-sectional histological analysis using Immunohistochemistry (IHC). The C57BL/6 mice bearing E0771 tumors were imaged with SFDI for a total of 10 days, including day 0, 3, 6, and 9.

4.2.4 Immunohistochemistry (IHC)

The DNA-binding dye Hoechst 33342 has been widely used to study the patency of the tumor vasculature^{93,94}. In this study, stock solutions of 16 mM Hoechst 33342 in PBS were stored at 4°C in the dark. Two minutes after tail vein or retro-orbital injections at 15 mg Hoechst 33342/kg body weight (40–50 µl/mouse with a 29 gauge needle), mice were euthanized and the entire tumor was collected⁹⁴. A green tissue marking dye (cat 24110, Polysciences Inc.) was applied on the top surface of the tumor, and a yellow tissue marking dye (cat 24112, Polysciences Inc.) was applied to the bottom surface of the tumor to label entire tumor surface. Following that, tumor was snap frozen in isopentane pre-cooled with dry ice. The tumor was then cut in half such that each half contains tumor surface labeled with green and yellow dyes, and were stored in -80°C. One half of the frozen tumor was sectioned (5 µm) in microtome to look at Hoechst stain and were stored at -80°C. The other half of the frozen tumor was first thawed at room temperature, fixed in 4% paraformaldehyde overnight, dehydrated in 70% ethanol, and was sent to Maine Health Center (Portland, ME) for preparation of paraffin-embedded blocks, sectioning (5 µm), and staining⁹⁵. Paraffin sections were stained with 5 different immunohistochemical markers, CD31, Glut-1, cleaved Caspase-3, PCNA, Mac-1. Briefly, paraffin-embedded sections were baked, de-waxed and treated with 3% H₂O₂ for 10 min to inactivate endogenous peroxidases. Antigen retrieval was carried out by steaming in 10 mM Sodium citrate buffer, pH 6 for 30 min. The samples were cooled to room temperature and then incubated in normal serum blocking buffer for 30 mins. The slides were then incubated in Vector A/B kit (SP2001, Vector Laboratories) for biotin blocking for 30 mins, incubated in primary

antibody overnight at 4°C, incubated in secondary antibody for 30 mins, incubated in signal amplification reagent (TSA for 60 mins or ABC for 30 mins), and incubated in DAB substrate (SK-4100, Vector laboratories) for 2-10 min (checked every min after 2 min). TBS-T wash buffer (1x Tris buffered saline pH 7.6 with 0.05% Tween) was used for the intermediate wash steps. Following a thorough wash with tap water, the slides were dehydrated and sealed with synthetic resin (Ex. Permount mounting medium). More details on reagents for each IHC marker is given below:

CD31:

Primary antibody: Anti-CD31 (ab28364, ABCAM) diluted 1:250 in blocking buffer

Secondary antibody: Biotinylated Goat anti-Rabbit (BA1000, Vector Laboratories) diluted 1:500 in PBS

Signal amplification reagent: Tyramide signal amplification TSA Biotin Kit (NEL700 or NEL700A, PerkinElmer)

CC3:

Primary antibody: Anti-cleaved caspase-3 (Asp175) (Cat. #9664L, Cell Signaling Technology) diluted 1:50 in blocking buffer

Secondary antibody: Biotin-SP-conjugated Goat Anti-Rabbit IgG (H+L) (Cat. #111-065-144, Jackson Immuno Research Laboratories) diluted 1:500 in PBS

Signal amplification reagent: ABC kit (PK-6100, Vector laboratories)

PCNA:

Primary antibody: Anti-PCNA (Cat. #2586S, Cell Signaling Technology) diluted 1:2000 in blocking buffer

Secondary antibody: Biotin-SP-conjugated Goat Anti-Rabbit IgG (H+L) (Cat. #111-065-144, Jackson Immuno Research Laboratories) diluted 1:500 in PBS

Signal amplification reagent: ABC kit (PK-6100, Vector laboratories)

Glut1:

Primary Antibody: Anti-Glut-1 (Cat. #07-1401, Millipore Sigma) diluted 1:400 in blocking buffer

Secondary antibody: Biotin-SP-conjugated Goat Anti-Rabbit IgG (H+L) (Cat. #111-065-144, Jackson Immuno Research Laboratories) diluted 1:500 in PBS

Signal amplification reagent: ABC kit (PK-6100, Vector laboratories)

Mac-1:

Primary antibody: Anti-CD11-b (Mac-1) (Cat #133357, Abcam) diluted 1:400 in blocking buffer

Secondary antibody: Biotin-SP-conjugated Goat Anti-Rabbit IgG (H+L) (Cat. #111-065-144, Jackson Immuno Research Laboratories) diluted 1:500 in PBS

Signal amplification reagent: ABC kit (PK-6100, Vector laboratories)

4.2.5 IHC Image Analysis

The frozen sections were imaged using the Olympus FSX100 Bio Imaging Navigator fluorescence microscope system (Olympus America Inc., Center Valley, PA) through a blue channel (excitation filter: BP360-370, DM400, emission filter: BA420-460). Liver of each mouse, sacrificed for IHC, was also sectioned (5 μ m) and imaged to observe Hoechst stain which confirms proper injection. The same microscope was used in bright field to image the paraffin embedded sections. One representative tumor cross-section was imaged

for each of the six biomarkers. All images were captured with 4.2X magnification. Representative images for each marker taken with 20X objective are shown in Fig. 4.1.

Figure 4.2 shows the IHC image processing procedure. Image processing was performed using FIJI⁹⁶. IHC images were captured in a snaking pattern with ~10% overlap²⁰, and then combined using the ‘stitching’ plugin. An example is shown in Fig. 4.2A with PCNA staining. The dotted region shows a single image and the inset shows a 20X magnification of a small represented area within the tumor, showing individual cells. The ‘Region of Interest (ROI) manager’ tool was used to manually select an ROI for the entire tumor cross-section, shown with solid yellow line in Fig. 4.2B. The ‘H DAB filter’ was then applied from the ‘color deconvolution’ plugin to extract the DAB signal. The image was then binarized using an intensity threshold as shown in Fig. 4.2C. For Mac-1 and Hoechst biomarkers, the threshold value was kept same for all tumors. For the other biomarkers the threshold varied to address differences in DAB staining. The percent of pixels above the threshold and within the ROI was then calculated as positive staining area (%).

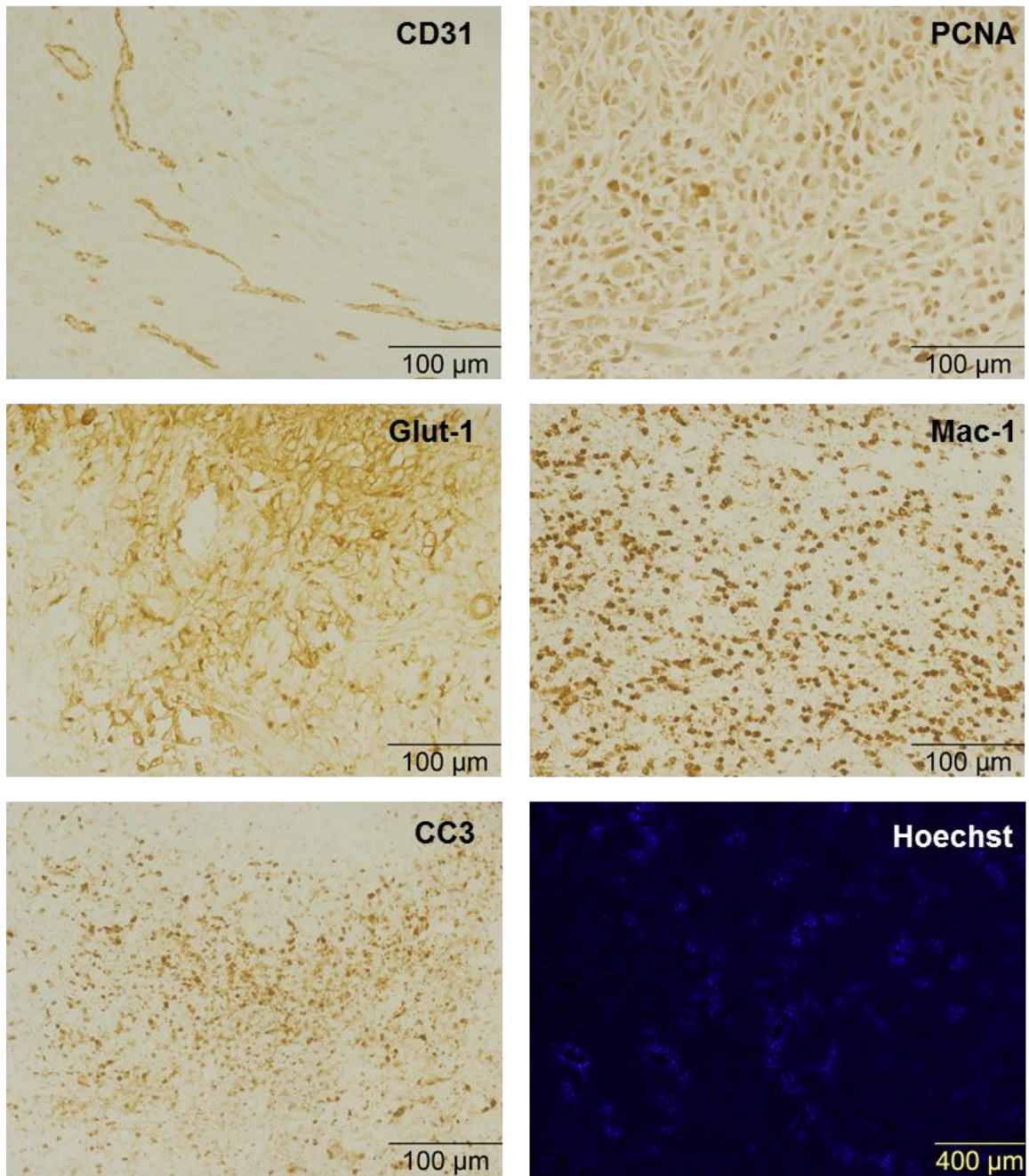


Figure 4.1: Representative images of the five IHC markers and Hoechst in a single PC3/2G7 tumor.

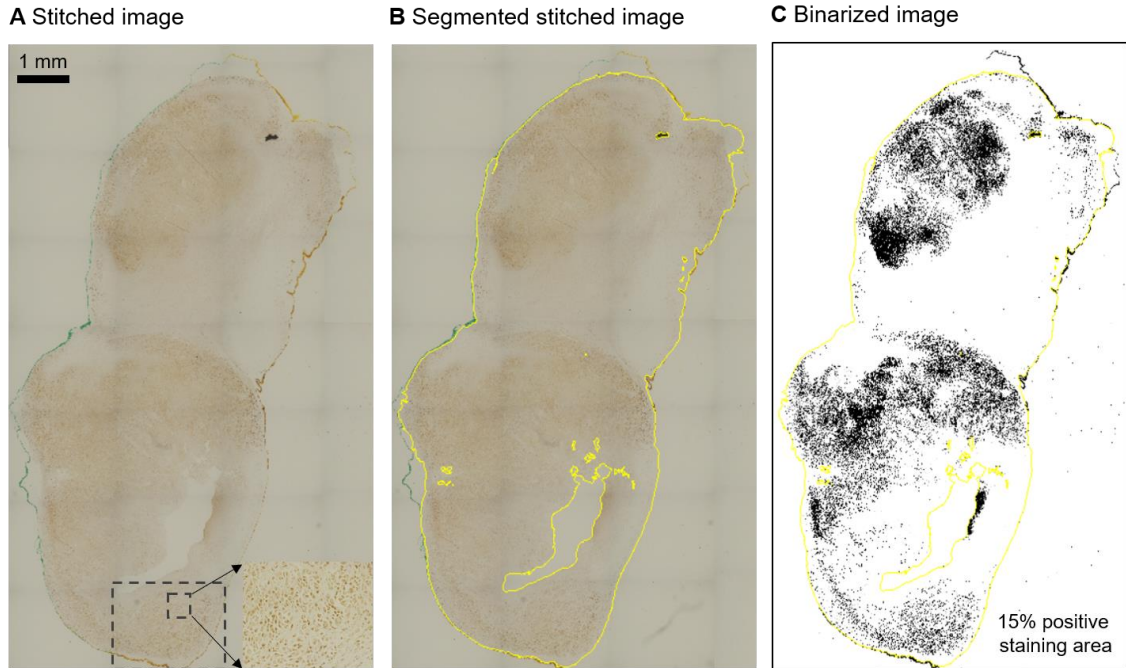


Figure 4.2: Image processing steps shown for a representative PC3/2G7 tumor. **A.** The tumor cross section was imaged in a snaking pattern with ~10% overlap, and then combined using the ‘stitching’ plugin in FIJI software to produce the stitched image. The dotted region shows a single image and the inset shows a 20X magnification of a small represented area within the tumor, showing individual cells. Green dye indicates top surface and yellow dye indicates bottom surface of the tumor. **B.** The solid yellow line shows manually segmented region for the tumor cross-section obtained with the help of the ‘Region of Interest (ROI) manager’ tool in FIJI. **C.** Binarized image obtained with the application of an intensity threshold. The percent of pixels above the threshold and within the ROI was defined as positive staining area (%). This tumor sample was stained for the PCNA marker (proliferation) and resulted a 15% positive staining area.

4.2.6 Statistical analysis

The Mann-Whitney Wilcoxon rank sum test was used to test if longitudinal SFDI and IHC metrics were statistically different from their baseline (day 0) values (results shown in Fig. 4.6, Fig. 4.8, and Fig. 4.9). Additionally, correlations were evaluated between each of six SFDI metrics (a, b, HbO₂, Hb, THb, StO₂) and each of six IHC metric (CC3, PCNA, CD31, Hoechst, Glut-1, MAC-1) using the Pearson correlation coefficient (ρ_P). Both unadjusted

P value and Tukey-Ciminera-Heysel (TCH) adjusted P values are reported in Fig. 4.6 and Fig. 4.8.

The Wilcoxon signed rank test was conducted to test if treated vs. control contrasts were significant (results shown in Fig. 4.11 and Fig. 4.12). Contrasts at each day were compared to a hypothetical median of 0. The resulting P values were adjusted with the TCH procedure for 24 (8 days X 3 metrics) multiple comparisons in Fig. 4.11 and 40 (8 days X 5 metrics) multiple comparisons in Fig. 4.12.

Multivariate discriminant analysis was performed for determination of treatment prediction accuracy (Fig. 4.13 and Fig. 4.14). Two types of classification algorithms were utilized, a linear classifier and a quadratic classifier^{30,97}. 5 fold cross-validation was used for all classifiers to mitigate potential over-training³⁰. Receiver-Operating Characteristic (ROC) curves were generated using computed posterior probabilities calculated from the classifiers. The Area Under the Curve (AUC) of the ROC curve was used as performance metric for the classifiers. Statistical analysis was conducted using the Prism 8 (GraphPad) software.

4.3 Results

4.3.1 SFDI reveals dynamic changes in optical scattering in control and treated tumors

Both CPA and DC101 treatments led to tumor regression in the PC3/2G7 tumors while control tumors grew exponentially during the course of the study (Fig. 4.3). Longitudinal visualizations of SFDI parameters were created to show the changes in optical parameters that occurred during the study, especially the changes in optical scattering, which tended to be the most dramatic. Figure 4.4 shows μ'_s maps ($\lambda=659$ nm) for representative control,

CPA, and DC101 treated PC3/2G7 tumors on days 0, 1, 9, 18 and 27. The display range for each tumor was chosen so that day 0 values fell in the middle of the color bar. This visually highlights both increases (shown in red) and decreases (shown in blue) from baseline. For the control tumor, tumor volume increased while scattering decreased throughout the 27 days period of tumor growth. For the CPA tumor, volume increases were mitigated by treatment while scattering increased, in stark contrast to the control. Similarly, for the DC101 treated tumor, volume increase was minimal but μ'_s increased dramatically up to day 27 in the rebound period. Although the μ'_s longitudinal increase is smaller in this particular CPA tumor compared to the DC101, the group average changes are comparable for the CPA and DC101 groups (Fig. 4.6A). Time course videos highlight similar changes with finer temporal resolution (Fig. 4.5). Less prominent contrast was observed in absorption based hemodynamic parameters such as HbO₂, THb and StO₂.

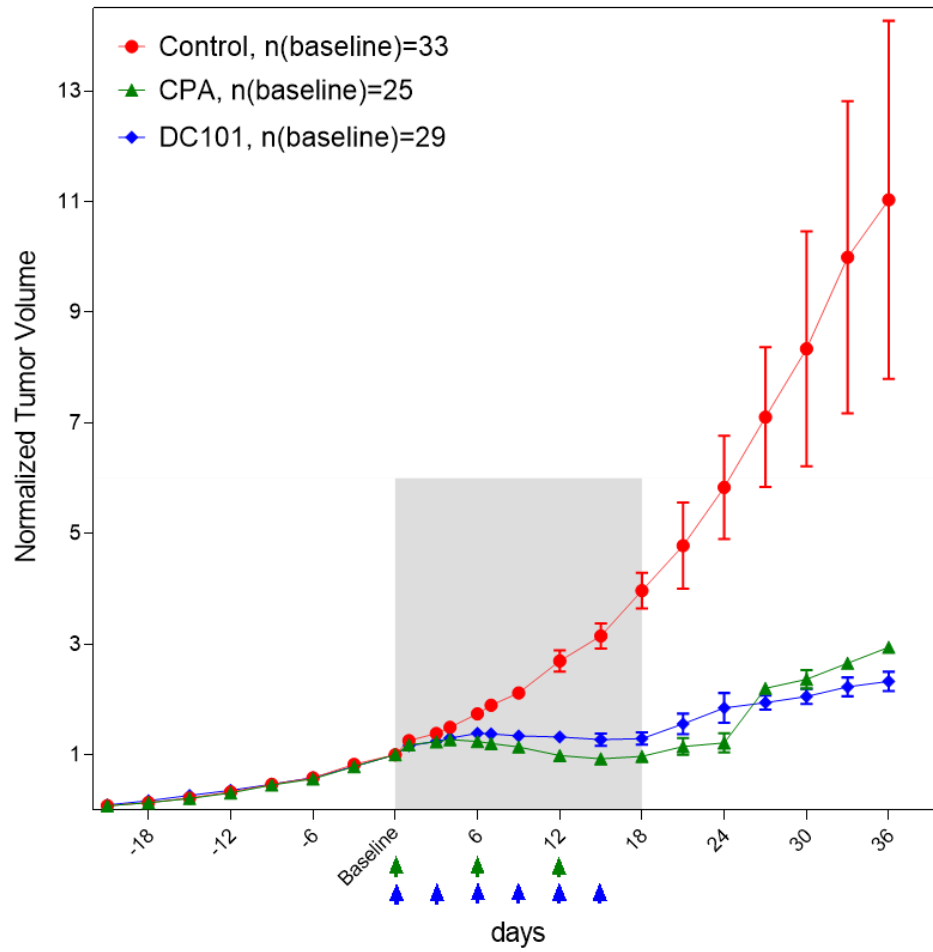


Figure 4.3: Tumor volume normalized to baseline for PC3/2G7 tumors for CPA, DC101, and no treatment (control) groups. The shaded region represents the 18 days of treatment period, and the arrows represent treatment cycles. The n values in the legend shows tumor population for each group at baseline, which reduced with days as mice were sacrificed for IHC. Each point represents group mean with standard error (SE). Tumor volume group mean and SE at baseline was $915 \pm 76 \text{ mm}^3$ for control, $805 \pm 86 \text{ mm}^3$, and $871 \pm 116 \text{ mm}^3$ for DC101.

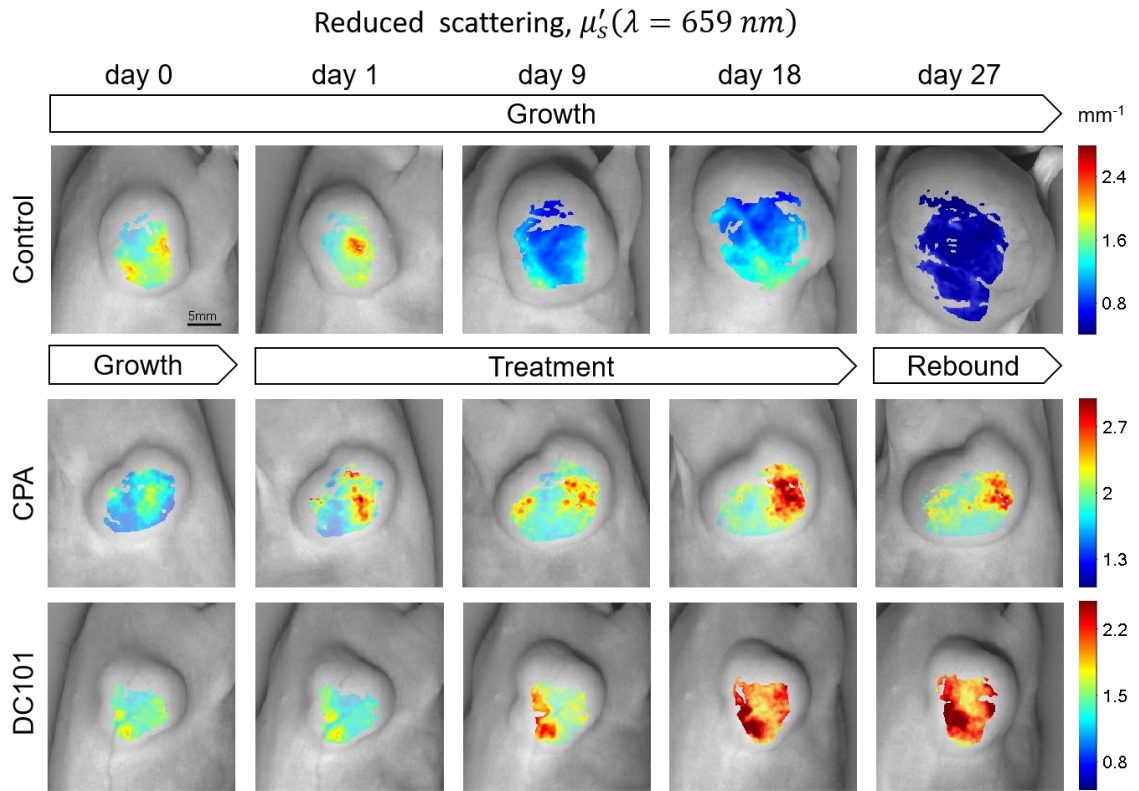


Figure 4.4: Longitudinal changes in reduced scattering maps at $\lambda=659 \text{ nm}$ for representative control, CPA, and DC101 treated PC3/2G7 tumors at days 0, 1, 9, 18 and 27.

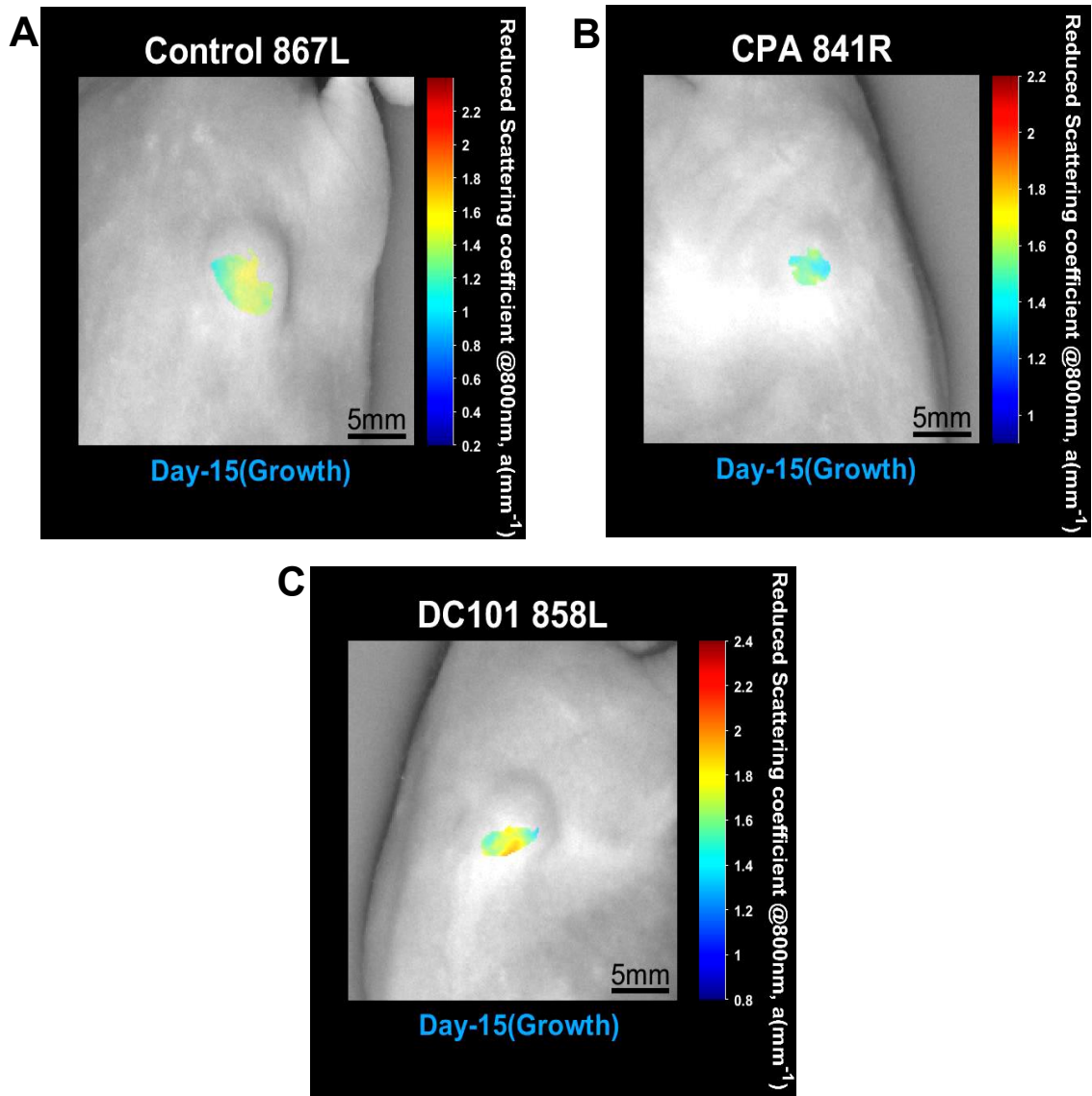


Figure 4.5: Videos of scattering amplitude a parameter μ'_s ($\lambda=800$ nm) for three representative PC3/2G7 tumors. Days, along with study periods, can be observed at the bottom of each image in the video. In the control tumor, tumor volume increased but a decreased continually until the mouse was euthanized on day 27. In contrast, in both CPA and DC101 treated tumors, a continued to increase before these mice were euthanized on day 57.

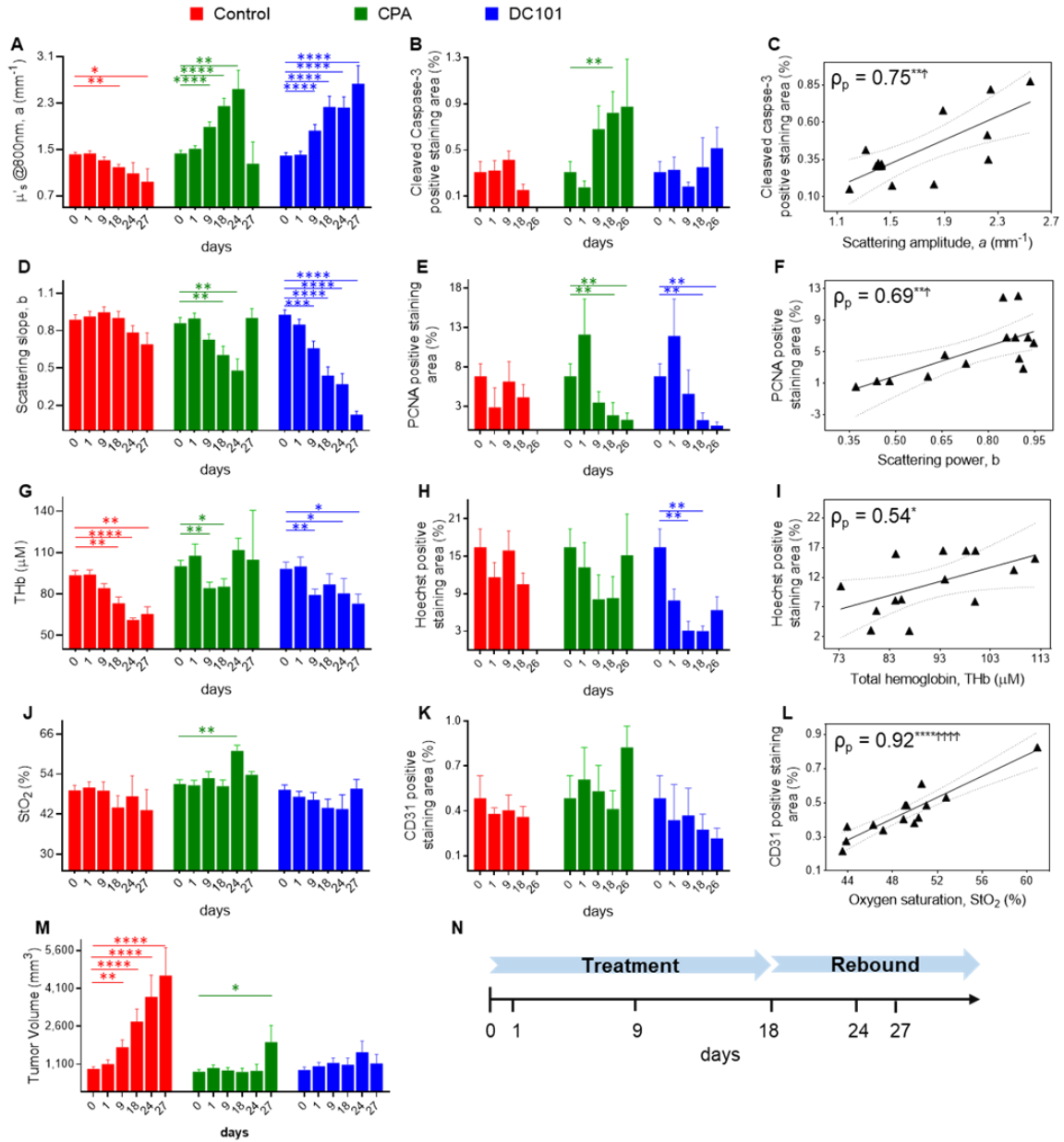
4.3.2 SFDI scattering parameters correlate with apoptosis and proliferation

Optical scattering is known to be sensitive to micro-architectural changes at the cellular and sub-cellular levels, and is likely to be correlated with treatment-induced biological changes⁸⁹⁻⁹¹. We explored how optical scattering and other SFDI parameters relate to the underlying tumor biology. To do this, *in vivo* SFDI imaging data of PC3/2G7 xenografts were interpreted in the context of IHC analysis of apoptosis (cleaved Caspase-3, CC3), proliferation (PCNA), vessel density (CD31), glucose uptake (Glut-1), macrophage infiltration (Mac-1), and vessel patency (openness) (Hoechst assay). Table 4.1 summarizes the SFDI optical parameters and their exploratory IHC biomarkers, along with our hypothesis for potential correlations and previous literature supporting the basis of potential correlations. For example, prior work in scattering spectroscopy and Optical Coherent Tomography (OCT) (integrated backscatter) demonstrated a positive correlation between scattering amplitude and apoptosis^{89-91,98,99}. Additionally, prior clinical diffuse optical clinical imaging studies and OCT preclinical work have shown a reduction in the wavelength dependence of scattering (i.e. scattering slope) as a marker of treatment response^{31,33,90,99}.

Figure 4.6 shows longitudinal changes in the SFDI parameters paired with IHC results. The pretreatment baseline measurements are shown at day 0. Treatment continued to day 18; day 24, 26, and 27 were in the post-treatment rebound period. Correlations between key imaging and IHC metrics are also shown. The number of tumors at each timepoint decreased over the study as mice were sacrificed for IHC analysis (shown in Fig. 4.7).

IHC and SFDI correlative analysis		
SFDI optical marker	IHC marker	Physiological basis for correlation
Scattering amplitude	Apoptosis	Cell break down during apoptosis may increase density of optical scattering events, resulting in an increase in scattering amplitude. This hypothesis is also supported by previous work ^{98,99}
Scattering power	Proliferation	The increase in cell density during proliferation may alter the distribution of scattering particle sizes, which causes scattering power to change. This hypothesis is also supported by previous work ^{31,33,99}
Oxyhemoglobin	Vessel density, vessel patency	A higher number of functional vessels is likely to result in increased blood distribution in the tumor, which will increase the Oxyhemoglobin parameter. This hypothesis is also supported by previous work ^{31,33,37}
Deoxyhemoglobin	Proliferation, glucose uptake	Increases in cell proliferation can potentially lead to increases in oxygen consumption due to higher metabolic activity in the tissue, causing an increase in Hb which can act as an indicator of tissue oxygen consumption. This hypothesis is also supported by previous literature ^{31,33}
Total hemoglobin	Vessel density, vessel patency	A higher number of functional vessels is likely to result in increased blood volume in the tumor, which will cause Total hemoglobin parameter to increase. This hypothesis is also supported by previous work ^{37,100,101}
Oxygen saturation	Vessel density, vessel patency	A higher number of functional vessels is likely to result in increased blood distribution in the tumor, which will cause the Oxygen saturation parameter to increase

Table 4.1: Exploratory correlations between SFDI optical parameters and IHC biomarker.



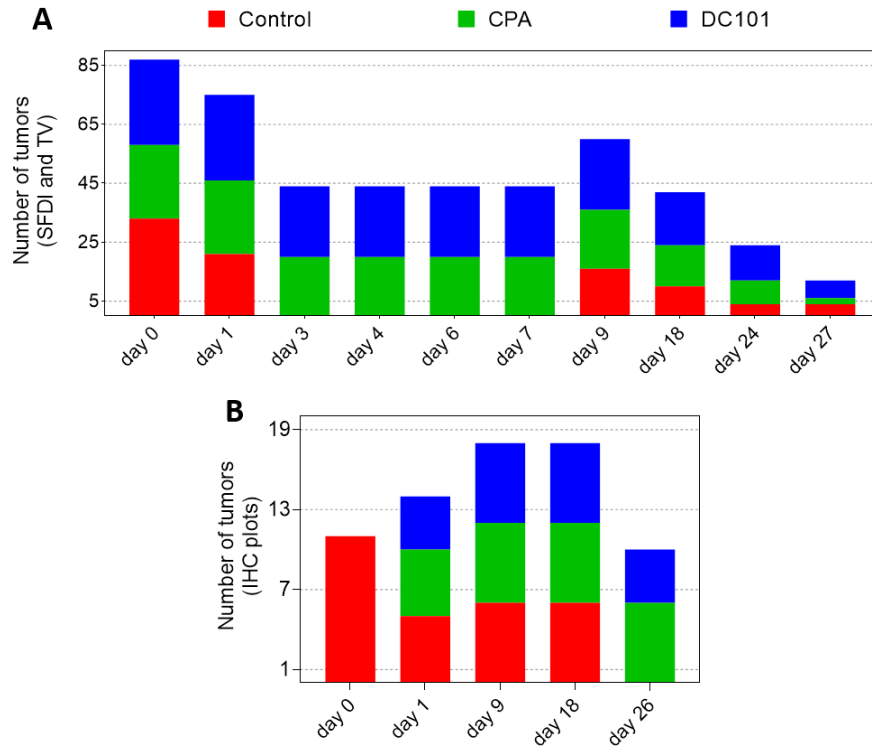


Figure 4.7: A. The number of tumors in each group at specific timepoints used for plotting and statistical tests with SFDI parameters and TV. Number of tumors from each group used in the Wilcoxon One-Sample Signed Rank test are the same as those shown above except for TV at day 1 for which number of tumors were $n(\text{control})=17$, $n(\text{CPA})=21$, $n(\text{DC101})=25$. The number of tumors from each group used in the classification test are the same as those shown above except for day 1, where the number of tumors were $n(\text{control})=17$, $n(\text{CPA})=21$, $n(\text{DC101})=25$ for both SFDI and TV. **B.** The number of tumors in each group at specific timepoints used for plotting of IHC markers.

The SFDI a parameter decreased in the control group but increased significantly in both CPA and DC101 groups during treatment and rebound (Fig. 4.6A). The SFDI b parameter displayed an opposite longitudinal trend in the treatment groups, with significant decreases observed during treatment and rebound (Fig. 4.6D). We note that in all of our previous preclinical tumor measurements with SFDI we have observed a and b to vary inversely with each other. More broadly, the relationship between the a and b parameters have been shown to be context-specific in literature in prior work⁸⁹⁻⁹¹.

The longitudinal patterns observed in the a parameter were broadly mimicked in CC3 as indicated by the large increases in both parameters in the CPA and DC101 groups (Fig. 4.6B). The changes in the b parameter were likewise mimicked in the PCNA trends, with significant decreases observed in both treatment groups (Fig. 4.6E). The correlations of the daily group means of these SFDI and IHC parameters were also strong for a versus CC3 (Fig. 4.6C, Pearson correlation coefficient (ρ_p) = 0.75 (unadjusted $P < 0.01$, TCH adjusted $P < 0.0085$)) and b versus PCNA (Fig. 4.6F, $\rho_p = 0.69$ (unadjusted $P < 0.01$, TCH adjusted $P < 0.0085$)). CC3 and PCNA values at day 26 were plotted against a and b at day 24 since no SFDI measurements were taken on day 26, and a and b at day 27 were not included in the correlation analysis due to the small number of tumors in the CPA group at this time point ($n=2$). It is of note that the drop in a and increase in b observed at day 27 in the CPA group coincides with the rebound period, and an increase in the average tumor size of that group (Fig. 4.6A and 4.6D, and Fig. 4.3). This may be an indication of tumor regrowth after treatment, although the small number of tumors at that timepoint ($n=2$) make this uncertain.

Similar trends to those observed in PC3/2G7 model were also observed in the a parameter for the E0771 tumors grown in C57BL/6 mice in response to CPA treatment (Fig. 4.9). Although the b parameter did not show a statistically significant decrease in the treated groups, the CPA group means showed a decreasing trend compared to control. The DC101 group did not show a trend in the b parameter, likely because of the poor treatment response of the DC101 treated E0771 tumors (Fig 4.9C and D).

4.3.3 SFDI hemodynamic parameters correlate with patency and vessel density

Prior clinical studies have demonstrated that both THb and HbO₂ decrease during successful treatment in breast cancer patients treated with neoadjuvant chemotherapy^{31,33} and several prior works have shown a positive correlation between THb and mean vessel area in breast cancer patients^{100,101}. In this study, significant decreases in THb and HbO₂ were observed in both treated and control groups (Figs. 4.6G and 4.8A), and significant decreased in Hb were observed in the DC101 treatment group (Figs. 4.8B). We hypothesized that the extent of functional vessels revealed by the Hoechst assay were likely to be correlated with blood volume and THb. This relationship was reflected to the largest degree in the DC101 group, where significant decreases in Hoechst staining were observed at day 9 and 18. The correlation between THb and Hoechst is shown in Fig. 4.6I ($\rho_p = 0.54$, unadjusted $P < 0.05$, insignificant TCH adjusted P value).

While there were changes in StO₂ over time, none of the changes were statistically significant except for day 24 in the CPA group. There were no significant changes in CD31 staining. However, the trends in these parameters were similar for each group, with decreases observed in the control and DC101 groups, and a spike within the rebound period in the CPA group. The linear correlation between these parameters was very strong (Fig. 4.6I. $\rho_p = 0.92$ (unadjusted $P < 0.0001$, TCH adjusted $P < 0.0000166$)).

The remaining longitudinal trends and correlations are shown in Fig. 4.8. The trends in both HbO₂ and Hb mimicked the trends in THb, with decreases observed in control and DC101 treatment groups, as well as a spike during rebound in the CPA group. Decreases in the glucose transporter Glut-1 were observed in the CPA group while increases were

observed in the DC101 group. Large increases in macrophage infiltration were observed in the DC101 treatment group. It is also of note that StO₂ and Glut-1 were strongly correlated $\rho_p = 0.83$ (unadjusted $P < 0.001$, TCH adjusted $P < 0.0017$), the b parameter and Mac-1 were strongly correlated $\rho_p = 0.8$ (unadjusted $P < 0.001$, TCH adjusted $P < 0.0017$), and the Hb parameter and the PCNA were strongly correlated $\rho_p = 0.72$ (unadjusted $P < 0.01$, TCH adjusted $P < 0.0017$). The drop in StO₂ with higher Glut-1 and increase in Hb with higher PCNA may both reflect the fact that an increased proliferation leads to increased oxygen consumption and a buildup of Hb³¹. A detailed list of the Pearson's ρ (ρ_p) values for each SFDI and IHC marker are shown in Figure 4.10. Based on our stated mechanistic hypotheses and previous literature supporting the basis of these correlations, we propose that these correlations represent, at least in part, causative links rather than merely associations.

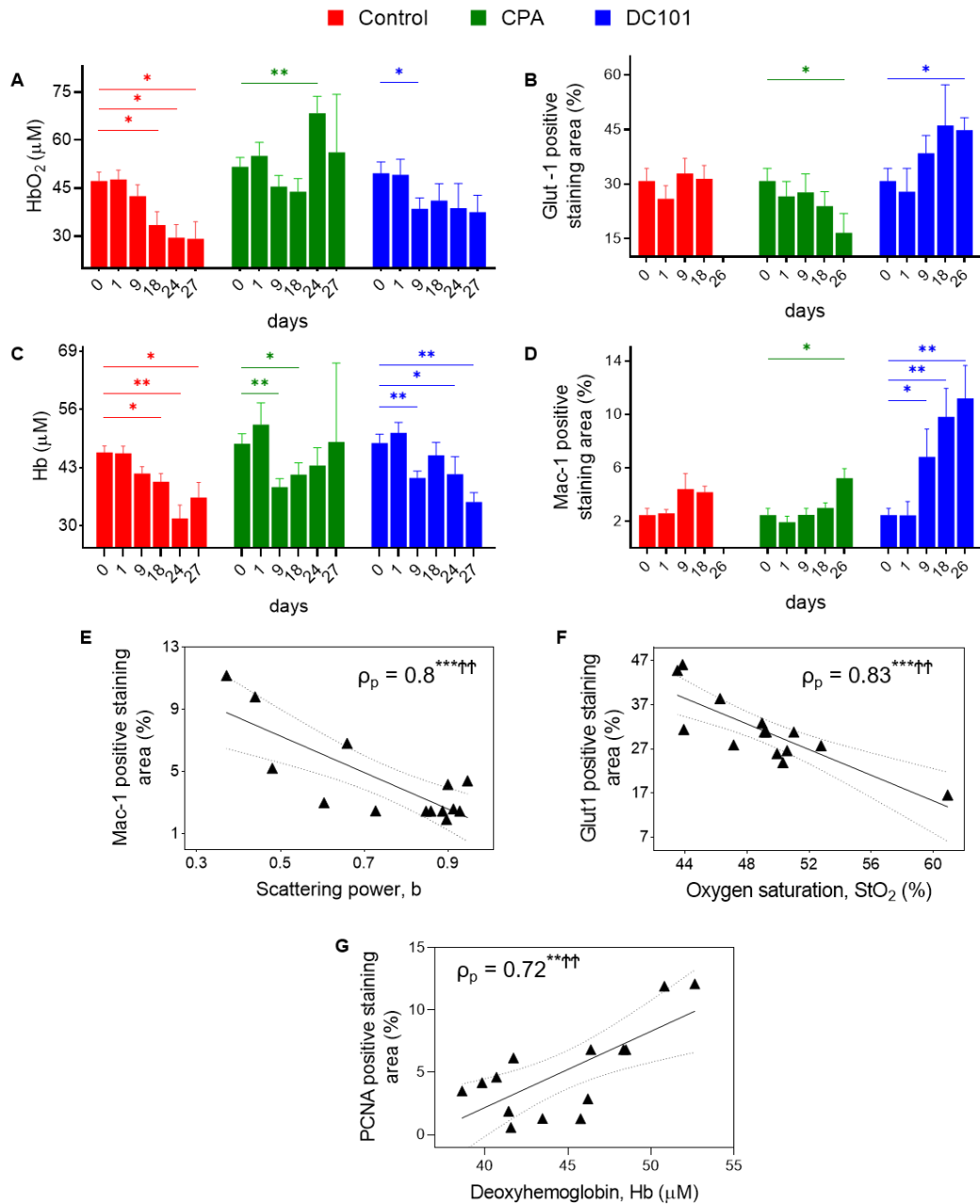


Figure 4.8: Longitudinal changes in the SFDI parameters (HbO₂ in A, Hb in C) and immunohistochemical results (Glut-1 in B, Mac-1 in D) at representative days in PC3/2G7 tumors. Data in the bar plots represent mean and standard error in each group. Mann-Whitney Wilcoxon rank sum tests were conducted to test if longitudinal SFDI and IHC metrics were statistically different from their baseline (day 0) values. The relationships between SFDI and IHC metrics are shown in E, F and G using daily group means from the bar plots. The linear best fit and 95% confidence intervals are indicated. The Pearson's ρ (ρ_p) is reported for each plot, along with significance range using P values. *Denotes significance range using unadjusted P values, and † denotes significance range using TCH adjusted P values. Here, *, $P < 0.05$; **, $P < 0.01$; ***, $P < 0.001$; ††, $P < 0.0017$.

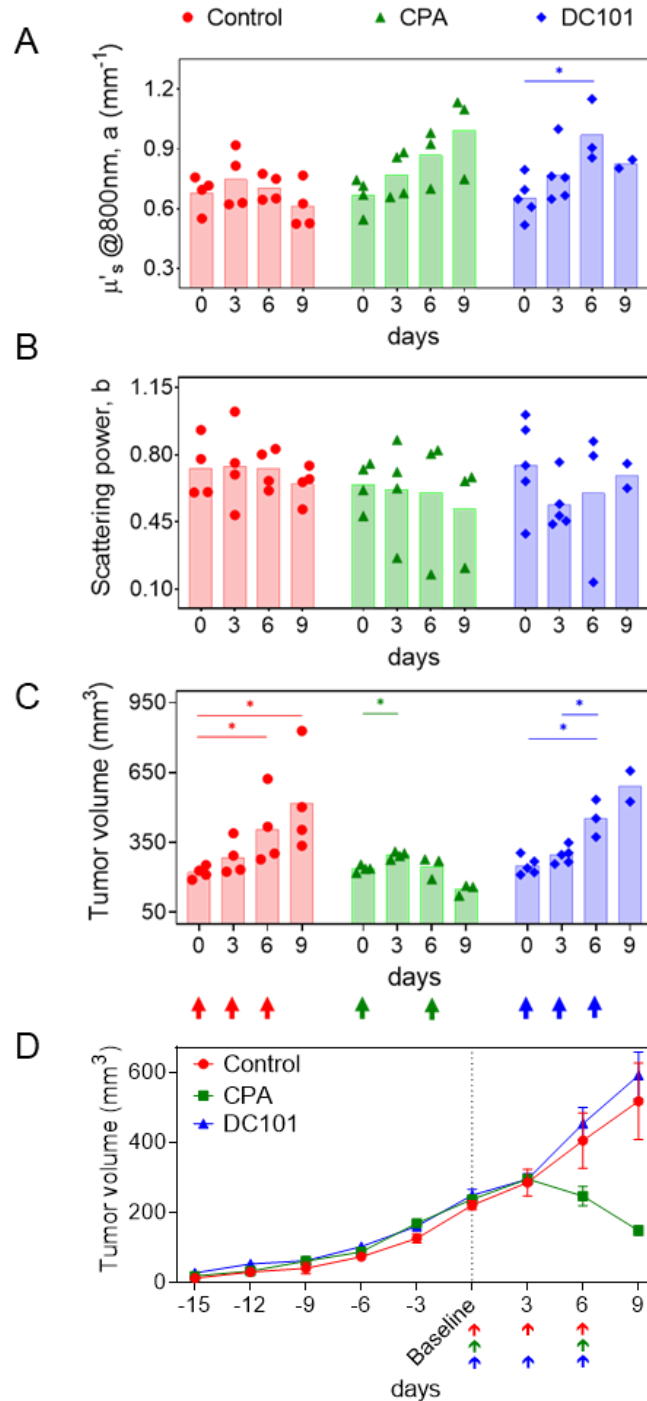


Figure 4.9: Longitudinal changes in the SFDI parameters a and b and TV in E0771 tumors in response to CPA and DC101. Data in A-C represent group mean along with individual tumor values, and in D represent group mean with SE. C and D both plot tumor volume but in different formats. Arrows represent treatment cycles. Mann-Whitney Wilcoxon rank sum test was used to test if longitudinal SFDI and TV metrics were statistically different from their baseline (day 0) values. *, $P < 0.05$.

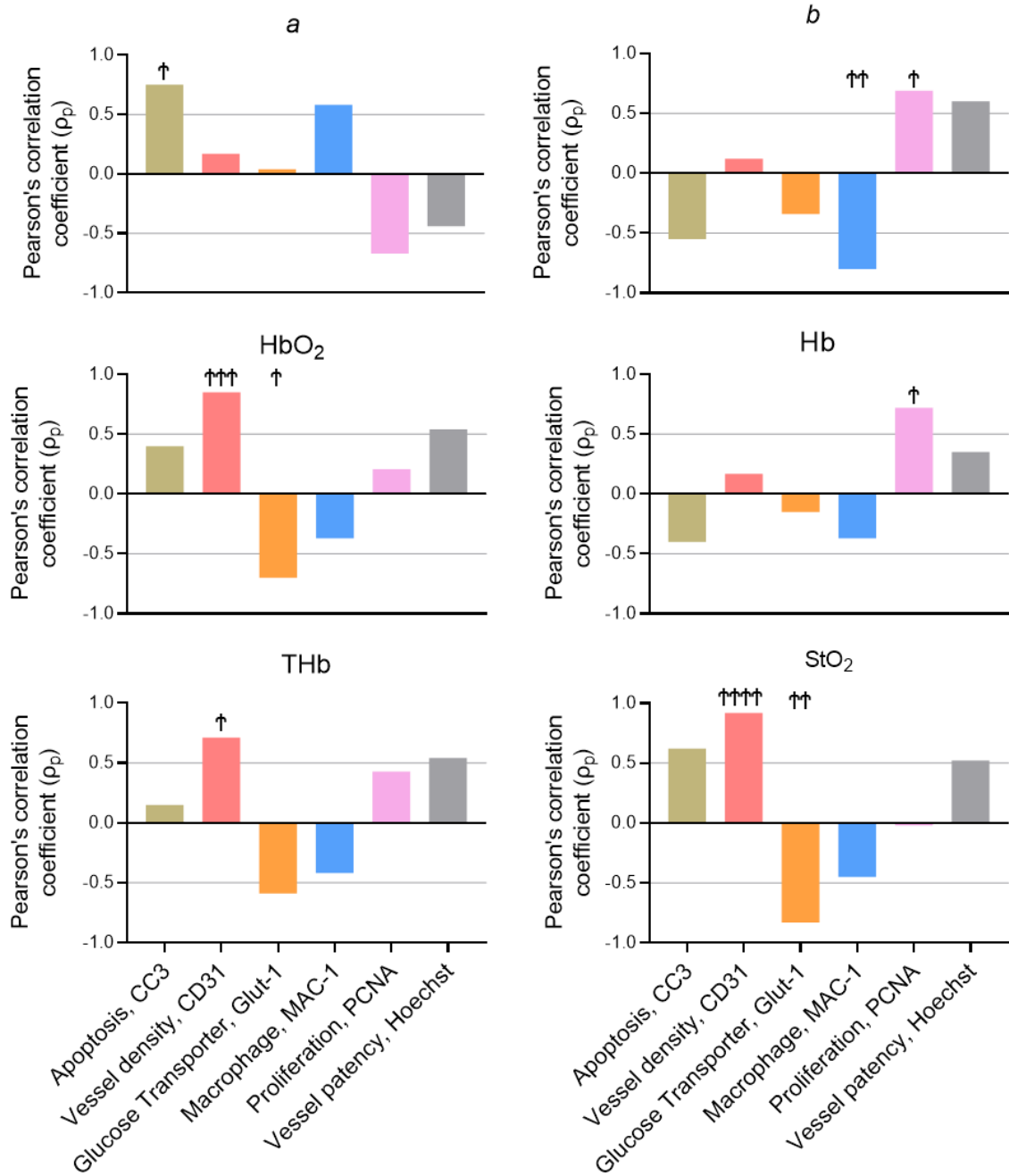


Figure 4.10: Pearson's ρ (ρ_p) values for each SFDI and IHC marker. † Denotes significance range using TCH adjusted P values. Here, †, $P < 0.0085$; ††, $P < 0.0017$; †††, $P < 0.000167$; ††††, $P < 0.0000166$.

4.3.4 Optical scattering provides high contrast between treated and control tumors

Imaging parameters that provide high contrast between responding and non-responding patients at early timepoints during cancer therapies provide the highest clinical utility for treatment monitoring³⁵. Here we explored optical contrast between treated and untreated tumors as a surrogate for clinical response. All tumor values were first normalized to day 0 (baseline) values. The Log_2 ratio of tumor and control optical properties and tumor volume (TV) are plotted over the duration of the study (Fig. 4.11). Each data point represents the ratio of a single treated tumor's value divided by the average value of the control group at that time point. The $y=0$ line indicates no contrast between treated and control whereas the $y=2$ represents a 4X contrast ($\log_2(2^2)=4$) and $y=-2$ represents a 0.25X contrast. The Wilcoxon One-Sample Signed Rank Test with a hypothetical median of 0 was used to test if the contrast was different from 0 at each time point. The resultant p values were adjusted with the Tukey-Ciminera-Heysel (TCH) procedure to account for multiple comparisons¹⁰².

For CPA, TV provided the largest average contrast between treated and control tumors over the study, but the a and b scattering parameters also provided high contrast (Fig. 4.11A). The contrast in these parameters continued to increase throughout the duration of the study. These trends were similar for DC101, where b performed almost as well as TV (Fig. 4.11B). It is to note that, TV follows b , but inversely follows a in the contrast plots.

Figure 4.12 shows contrast data for other SFDI hemodynamic parameters (HbO_2 , Hb, THb, StO_2). The contrasts in these hemodynamic parameters were not statistically

significant for most days in the study. Based on the results from this analysis, we next explored how SFDI parameters could be used either as a stand-alone marker, or as a companion marker to anatomic tumor size to predict treatment response at early timepoints.

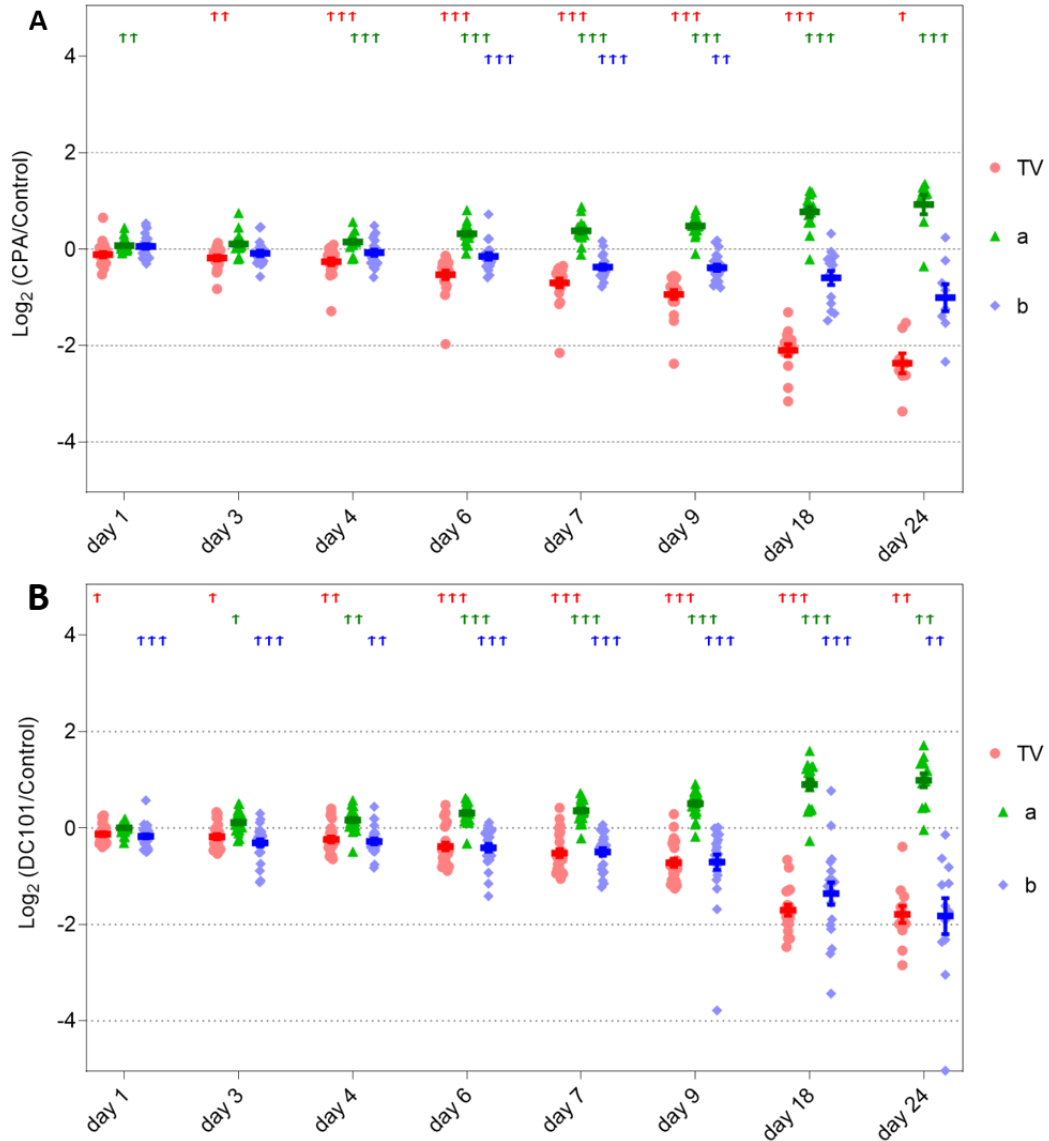


Figure 4.11: A. Log₂ ratios of CPA treated versus control for TV, *a* and *b*. **B.** Log₂ ratio of DC101 treated versus control. Mean and standard errors are indicated. The Wilcoxon One-Sample Signed Rank Test with a hypothetical median of 0 was used to test if the contrast (Log₂ ratio) was different from 0 at each time point. The resultant *P* values were adjusted with the TCH procedure to account for multiple comparisons. † denotes significance range using TCH adjusted *P* values. Here, †, *P* < 0.0104; ††, *P* < 0.002; †††, *P* < 0.0002.

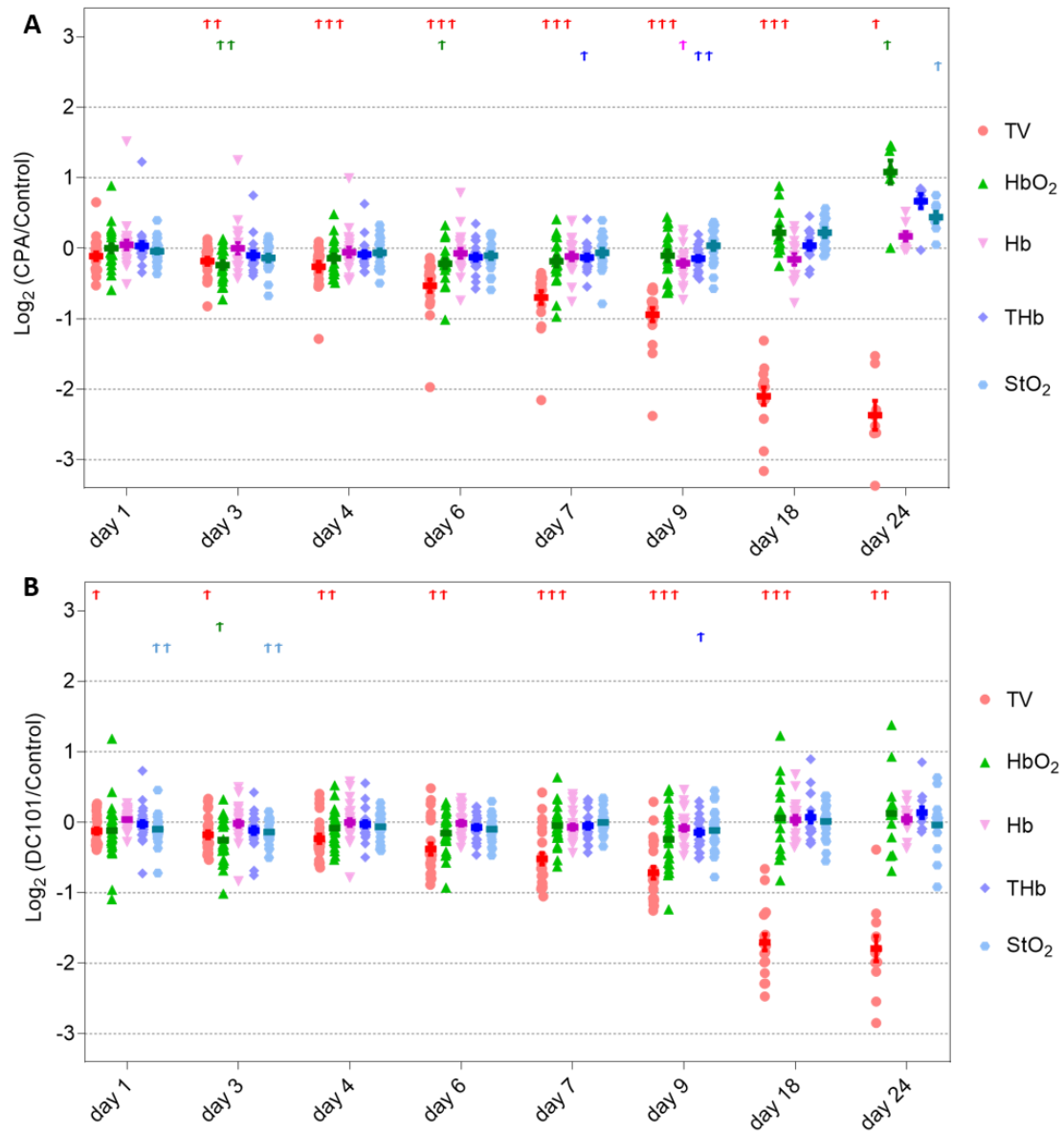


Figure 4.12: A. Log₂ ratio of CPA treated tumor and control group average for TV and SFDI parameters (HbO₂, Hb, THb and StO₂) over the duration of the study. **B.** Log₂ ratio of DC101 treated tumor and control group average for TV and SFDI parameters. Mean and standard errors are shown. The Wilcoxon One-Sample Signed Rank Test with a hypothetical median of 0 was conducted to test if the contrast (Log₂ ratio) was different from 0 at each time point. The resultant *P* values were adjusted with the TCH procedure to account for multiple comparisons. † denotes significance range using TCH adjusted *P* values. Here, †, *P* < 0.0081; ††, *P* < 0.0016; †††, *P* < 0.000158.

4.3.5 The combination of the SFDI scattering parameter a and tumor volume provides a superior early response prediction than either parameter alone

Multivariate discriminant analysis was conducted to determine the prediction accuracy of SFDI parameters as either stand-alone imaging markers, or as companion markers to anatomic tumor size, which can be measured with a number of standard-of-care imaging modalities (e.g. ultrasound, mammography, MRI). In this analysis, tumor values were normalized to day 0 (baseline) and only timepoints within the treatment period (\leq day 18) were considered. Classification was conducted using single features and sets of two features. Classification for each individual feature and set of features was repeated 101 times and the median performing classifier (determined by AUC) was used for comparisons at individual days. The single feature and feature combination that provided the highest average AUC over all measurement days were defined as the best feature sets.

The scattering parameter a was the best performing single SFDI feature, with an average AUC across all days of 0.84 for CPA and 0.83 for DC101. TV had an average AUC of 0.86 for CPA and 0.80 for DC101. The combination of a and TV was the best performing dual feature, with an average AUC of 0.86 for CPA and 0.87 for DC101.

A summary of classifier performance of several well performing single and dual features at different study days is shown in Fig. 4.13. For CPA, a provided better performance than TV at days 1 and 4 despite the fact that TV had a higher contrast on these days (Fig. 4.11A). This is due to the lower variation in a parameter across tumors within the treatment and control groups, providing a better separation of these groups by the classifier. When a was combined with TV (referred to as $a+TV$ in Fig. 4.13), superior

performance occurred at days 3 and 4 when comparing to either parameter alone. For DC101, a provided better performance than TV at days 1, 4, 6, 7, and 9, and the combination of a and TV had superior performance over either single feature at days 3, 4, 6, 7, and 9. The AUC for other well performing features such as b , $a+b$, $b+TV$ are also shown. It is to note that at very early timepoints, such as day 1 and day 3, the stand-alone SFDI features a and b perform better than TV. This is also apparent in the ROC curves at day 1 and day 3.

An additional analysis was conducted to compare how much earlier SFDI can predict response compared to TV. Fig. 4.14A and Fig. 4.14B shows AUC values up to day 7 along with linear regression lines for CPA and DC101. The number of days it takes for TV to reach the same AUC value obtained with the a or b parameter was computed for each day using the regression fits. The difference in days is plotted on y axis. Here, a positive y value means SFDI feature precedes TV by that many days, and negative y value means TV precedes the SFDI feature. For CPA, the a parameter exhibits a positive value close to 2 days at day 1, meaning within just one day into treatment, a parameter can be a better predictor of treatment response than TV (Fig. 4.14C). This may be because the a parameter reflects ongoing apoptosis, but the resulting change in tumor volume likely takes longer due to the time it takes in clearance of cell debris. However, the b parameter exhibits only negative values meaning it doesn't precede TV on any day. These results are consistent with the AUC values plotted in Fig. 4.13A at day 1. For DC101, the b parameter exhibits positive values of around 2 days up to day 4, meaning at these early timepoints b parameter can be a better predictor of treatment response than TV (Fig. 4.14D). The a parameter for

DC101 precedes *TV* starting at day 4. These results are consistent with the AUC values plotted in Fig. 4.13B. The fact that the a parameter is more effective in CPA and the b parameter is more effective in DC101 at early timepoints may be a result of the specific mechanism of each of these drugs.

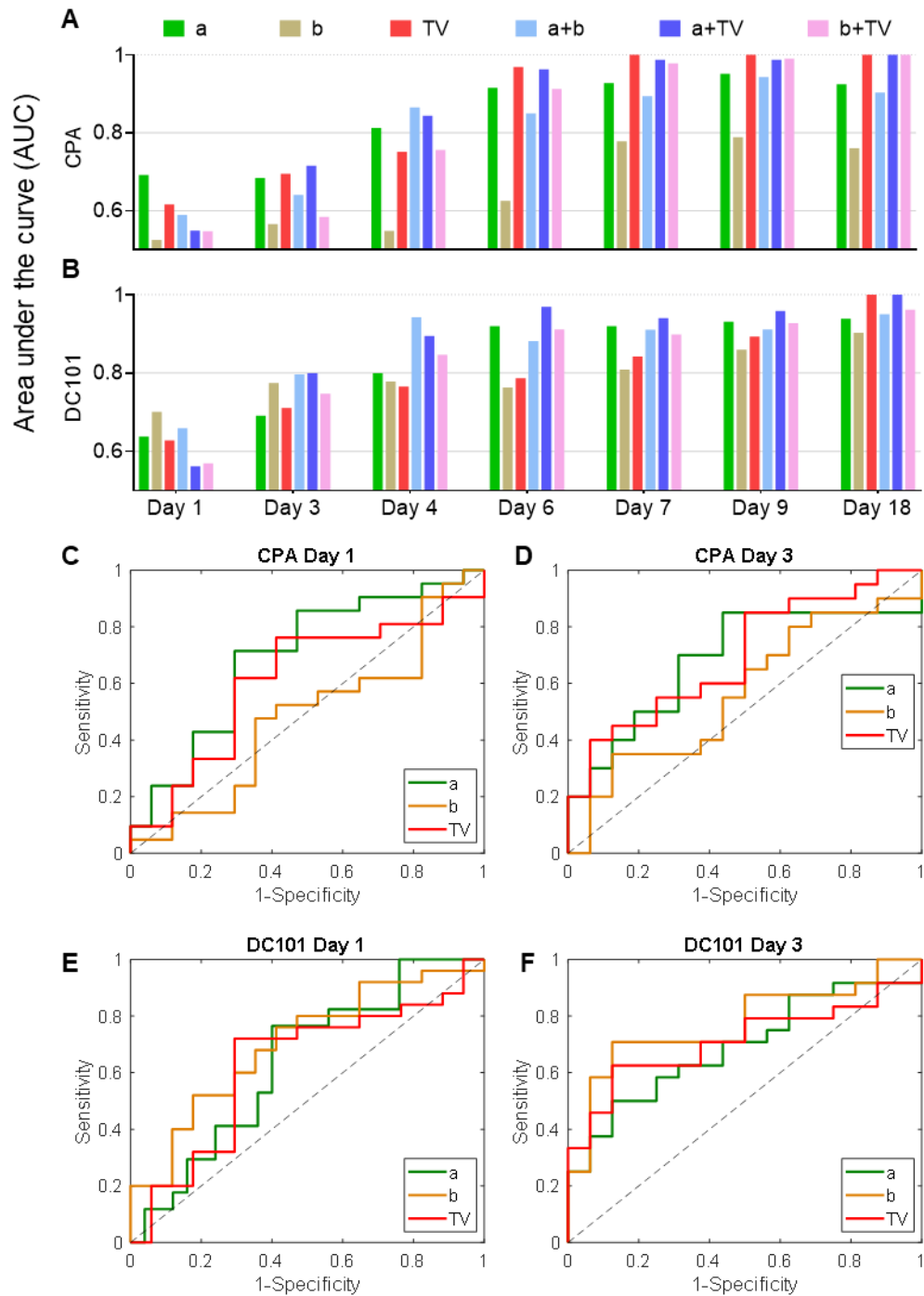


Figure 4.13: Multivariate discriminant classification analysis for discrimination of treated versus control tumors. The AUC of the well performing stand-alone and dual features along with the best performing features are shown in A for CPA and in B for DC101. Corresponding ROC curves for CPA are shown in C for day 1 and in D for day 3. ROC curves for DC101 are shown in E for day 1 and in F for day 3.

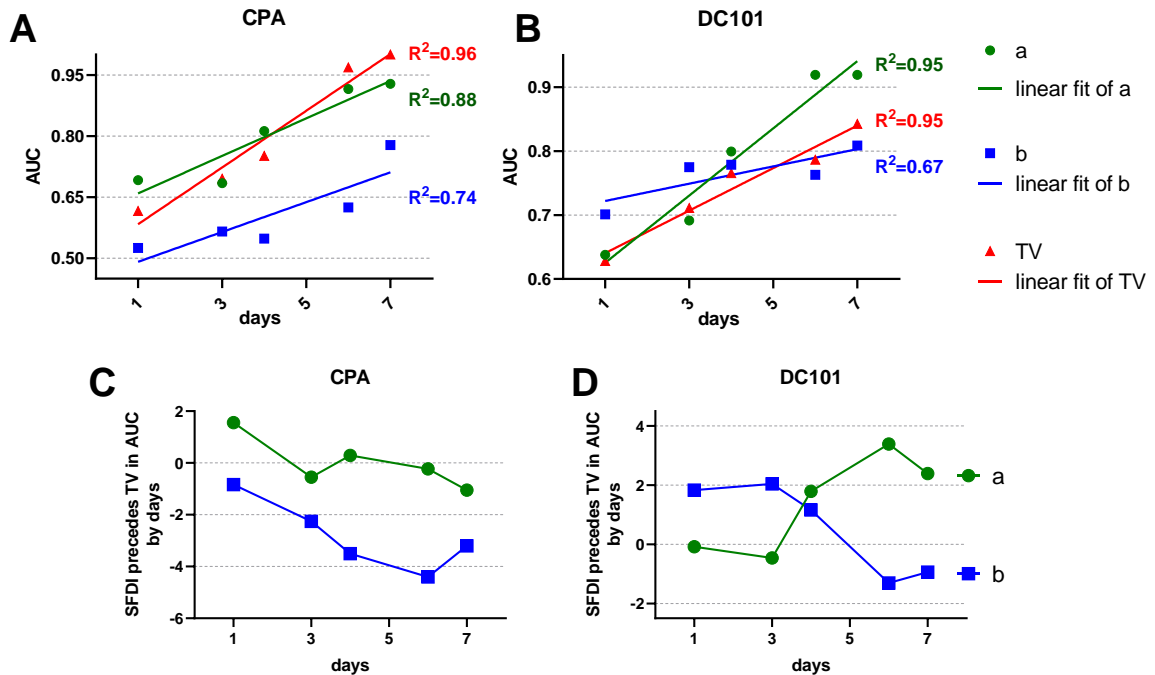


Figure 4.14: A and B plots AUC values up to day 7 and the linear regression lines for CPA and DC101 respectively. In C and D, the TV regression equation from A and B was used to calculate how many days it will take for TV to reach the same AUC value obtained with *a* or *b* parameter on a certain day, and their difference is plotted on y axis for CPA and DC101 respectively.

4.4 Discussion

In current clinical practice, NAC response assessment is determined predominantly by serial physical examination, mammography and/or ultrasound¹⁶. Yeh et.al showed that palpation, mammography, ultrasound and MRI had 19%, 26%, 35%, and 71% agreement, with final pathological response respectively. These and other studies have shown that anatomical changes in tumor presentation are not reliable predictors of final pathological state^{103–105}. This leaves an opportunity for other modalities to measure response markers that provide different functional information than simply anatomic changes. Although functional measurements of tumors from contrast-enhanced MRI, MRS, and PET have shown substantial improvement over conventional anatomic imaging^{106–110}, the cost,

radiation exposure, and potential toxicities of contrast agents limit the frequency of these scans during treatment.

DOI offers a low-cost and safe approach and thus a potential candidate to address this very clinical need. A growing number of reports over the last have shown that DOI derived hemodynamic parameters can correlate with treatment response in breast cancer patients receiving NAC²⁸⁻³⁵. SFDI is a preclinical DOI tool that provides the same optical and functional information, and thus is a great candidate for *in vivo* tumor monitoring in small animal oncology models. Chapter 2 and 3 of this dissertation were focused on establishing the feasibility of longitudinally and frequently monitoring tumor xenografts and improving SFDI accuracy for preclinical tumor models^{52,53}. This chapter focuses on understanding the rationale behind changes in SFDI parameter and explored the ability of SFDI to predict treatment response early in the treatment. First, we demonstrated that SFDI can track both absorption and scattering based contrast in a prostate xenograft model in response to cytotoxic and antiangiogenic treatment for over a period of one month. Then using a large-scale cross-sectional animal study design, correlations were established between specific SFDI and IHC markers over the course of the study (up to day 27 after treatment). And lastly, the SFDI imaging parameters were tested to identify early optical markers of treatment response.

Longitudinally, the a parameter decreased in the control group but increased substantially in CPA with the exception of day 27. The decrease in a at day 27 may result from the tumor rebound, which was apparent in the tumor volume data (Fig. 4.6M). The a parameter increases substantially in the DC101 groups during both treatment and rebound

(Fig. 4.6A). Unlike the CPA group, the DC101 tumors did not rebound rapidly after the end of treatment (Fig. 4.6M), which likely explain the continued increase in the a parameter up to day 27. The SFDI b parameter displayed an opposite longitudinal trend in the treatment groups, with substantial decreases observed during treatment and rebound (Fig. 4.6D). It is of note that the drop in a and increase in b observed at day 27 in the CPA group coincides with the rebound period, and an increase in the average tumor size of that group (Fig. 4.6A, 4.6D, and Fig. 4.3). While, this may be an indication of tumor regrowth post treatment period ($n=2$), it needs to be tested in higher number of tumors. For the DC101 group, tumor rebound is likely to take longer due to the vascular damage from the antiangiogenic treatment¹¹¹.

In the correlation analysis, the scattering a parameter strongly correlated with cell apoptosis (CC3) ($\rho_p = 0.75$) and scattering power b parameter correlated strongly with cell proliferation (PCNA) ($\rho_p = 0.69$). Prior work utilizing modelling in and *in vitro* cell experiments with optical scattering methods have demonstrated distinct relationships between scattering amplitude (a) and the density of scattering events, as well as scattering power (b), and the distribution of scattering particles sizes^{89,90}. We hypothesize that as cells break down during apoptosis the density of optical scattering events increases, resulting in an increase in the a parameter. The increase in cell density during proliferation may in turn alter the distribution of scattering particle sizes, which causes b to decrease. Prior OCT work has also demonstrated an increase in integrated backscatter and decrease in scattering slope in response to treatment in preclinical tumors^{98,99}. Clinical DOI tools have also revealed a decrease in the b parameter in breast cancer patients responding to

treatment, similar to our observation in prostate xenograft^{31,33}. Similar trends were observed in the a and b parameters for the E0771 tumors (Fig. 4.9).

For the absorption based parameters, the vessel density marker CD31 correlated strongly with the SFDI hemoglobin parameters ($\rho_p(\text{HbO}_2)=0.85$, $\rho_p(\text{THb})=0.71$ and $\rho_p(\text{StO}_2)=0.92$), and the vessel patency marker Hoechst correlated fairly well ($\rho_p(\text{HbO}_2)=0.54$, $\rho_p(\text{THb})=0.54$ and $\rho_p(\text{StO}_2)=0.52$) as expected (Fig. 4.5). Prior work also reported positive correlations between THb, HbO₂ and mean vessel area marker (CD34)^{100,101}. Our hypothesis behind these correlations is that a higher number of functional vessels is likely to result in increased blood distribution in the tumor, which will cause the hemodynamic parameters to increase. The Hb parameter was found to strongly correlate with PCNA ($\rho_p = 0.72$), and we hypothesize that increases in proliferation lead to increases in oxygen consumption, resulting in an increase in Hb³¹. The macrophage marker Mac-1 was found to positively correlate with a ($\rho_p = 0.58$), likely due to macrophage recruitment caused by clearance of dead cells after substantial apoptosis¹¹². In total, the correlation analysis both validated changes and correlated previously observed in preclinical and clinical studies, while strongly identifying the much less explored optical scattering parameters as potential non-invasive markers of apoptosis, proliferation, and overall treatment response.

For CPA, both a and b scattering parameters and TV provided high contrast between treated and control tumors (Fig. 4.10A). These trends were similar for DC101 (Fig. 4.10B). Changes in TV are likely related to the balance between cell death and cell proliferation. Since we found strong correlations between apoptosis and the a parameter,

and proliferation and the b parameter, these SFDI parameters may be a useful non-invasive way to track treatment response over time. The relatively poor optical contrast between treated and untreated in SFDI hemodynamic parameters (Fig. 4.11) may be a reflection of hypoxia within the control group induced by rapid tumor growth outpacing vascular supply¹¹³. This could result in similar decreasing hemodynamic trends in both treated and control groups, but with different biological origins.

In the classification analysis scattering a parameter was the best performing single SFDI feature, and $a+TV$ was the best performing dual feature considering days until the end of treatment (day 18). This suggests that the a parameter may substantially supplement or replace tumor volume as an indicator for treatment response. This is important as anatomic tumor size is currently the only available clinical marker for measuring treatment response in many cancers¹⁶. However, at the early timepoints, the SFDI stand-alone feature a and b perform better than TV in treatment response prediction in CPA and DC101 respectively. This might be a reflection of how these two drugs act against tumor and thus should be further investigated.

4.5 Conclusions

While DOI techniques have emerged as a powerful new tool aid to provide metabolic and molecular profiles of tumors, these tools so far have largely focused on absorption based endogenous parameters like hemoglobin, water and lipid^{28,30,35,88}. Optical scattering remains largely unexplored in the context of treatment monitoring in the clinic. We have shown here that scattering a and b parameters have the potential to indicate treatment response due to their sensitivity to apoptosis and proliferation respectively. Our findings

suggest optical scattering should be further investigated in the clinical setting for breast and other tumor types with clinical DOI tools. Upon successful clinical translation and validation, findings from this chapter may help clinical DOI tools develop as important feedback methods in the application of treatment monitoring, testing new drug, and personalizing treatments.

CHAPTER FIVE

Develop a new Light Emitting Diode (LED)-based SFDI system to measure tissue water content in the VIS-NIR region

A portion of the methods and text below are part of the article under review for the Journal of Biomedical Optics with the following contributing authors. There was no work related to IR-SFDI or water measurements in the article. I spearheaded the construction of the IR-SFDI device as well as the specific measurements and analysis presented in this chapter 5.

openSFDI: An open-source guide for constructing a spatial frequency domain imaging system

Matthew B. Applegate^a, Kavon Karrobi^a, Joeseeph Angelo^b, Wyatt Austin^c, Syeda Tabassum^d, Karissa Tilbury^c, Rolf Saager^e, Sylvain Gioux^b, Darren Roblyer^a

^aBoston University, Department of Biomedical Engineering

^bUniversité de Strasbourg

^cUniversity of Maine

^dBoston University, Department of Electrical and Computer Engineering

^eLinköping University

5.1 Introduction

A limitation to most of the prior SFDI literature as well as the previous chapters of this thesis is that SFDI has largely been developed to monitor only tissue hemodynamics and optical scattering. Prior clinical DOI studies have also focused on water and lipid extractions, which have been shown to be important biomarkers for treatment response

monitoring^{33,114}. In this chapter we begin to address this limitation by expanding SFDI instrumentation to include spectral sensitivity to water content.

Insight into tumor water content can be derived from MRI studies of the apparent diffusion coefficient of water (ADC_w). The ADC_w correlates with cellular density in several tissues, including brain^{115,116}, breast¹¹⁷, and bone marrow¹¹⁸. Several research studies using breast tumor animal models¹¹⁹ and human melanoma xenografts¹²⁰ have supported these findings. The ADC_w also was shown to correlate with cellular pathology¹¹⁸. The concept that changes in the ADC_w can reflect tumor therapeutic response was also supported by other studies in murine tumor models¹²¹. Subtle variations in water content, optically detected, have also been shown to relate to subtle changes in tumor cell density and edema, where reductions in tumor water content may represent diminished cellularity due to cell death¹²².

Over the last decade, in numerous studies with breast cancer patients receiving NAC, clinical DOI tools have found that the tissue concentration of water ($H_2O(\%)$) in tumors is important for treatment monitoring^{31,33,35}. For example, Soliman et al. showed that water decreased from 100% to 40.4% over 4 weeks of treatment in responders ($n=5$) compared to 84.6% in nonresponders ($n=3$)³³. We note here the reported H_2O is the concentration of measured tissue water divided by pure water concentration (55.6 M). Thus, the reported water percentages are relative figures of merit compared to pure solutions of the substance. The value is not the measure of strict volume and doesn't add up to 100%³³. The ability to quantify tissue water content also has significance for other conditions such as edema, burns, and wound healing^{123,124}.

These prior findings help demonstrate that water is an important prognostic biomarker for cancer. While hemoglobin absorption features span the VIS and NIR, most prior SFDI systems utilize measurements below 850 nm^{125,126}. Water absorption features occur at wavelengths past this limit, with a prominent peak location at 970 nm (Fig 5.2). There are only a few prior reports where efforts were made to employ SFDI at water sensitive wavelengths¹²⁷⁻¹³⁰, and these prior systems are expensive and lack portability due to the use of tabletop laser systems as illumination sources in the Short Wave Infrared (SWIR) region^{129,130}. To bridge this gap, in this work we developed an LED-based compact SFDI system that can measure water content as well as tissue hemodynamics, and thus improve on the scope and application of SFDI. The system will be referred to as Infrared-SFDI (i.e. IR-SFDI) in rest of the chapter.

5.2 Materials and methods

5.2.1 IR-SFDI Hardware

There are three main components to IR-SFDI system: light source, method of spatially modulating the illumination field, and the detector⁵⁵. The specific components of the IR-SFDI system were chosen to balance cost, and overall performance. A schematic of the system is shown in Fig. 5.1. The total cost of the IR-SFDI system was kept within \$5000 USD.

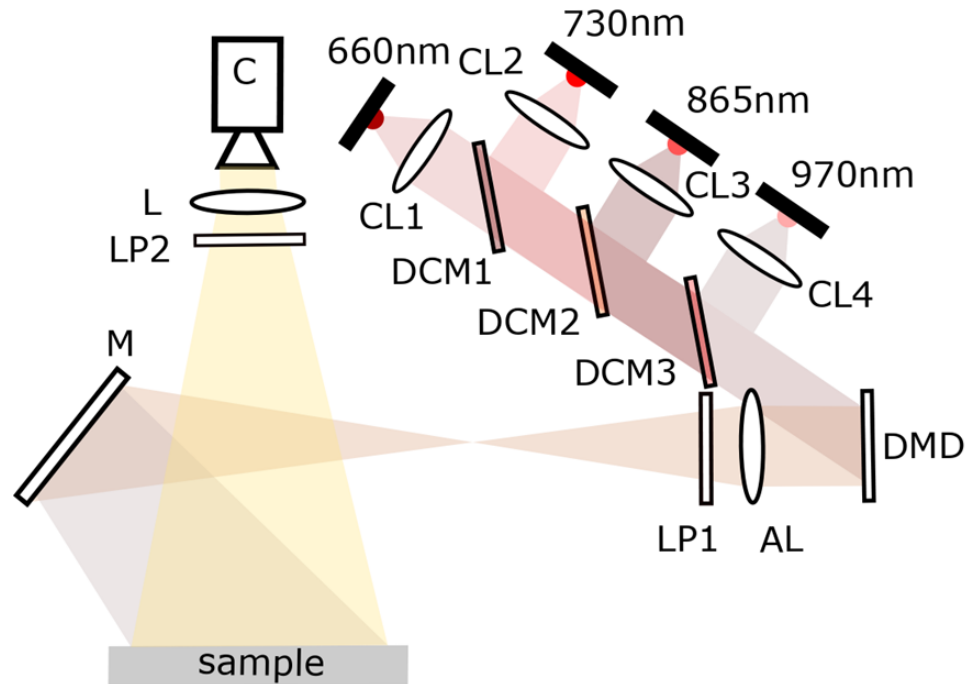


Figure 5.1: Schematic of the IR-SFDI system. CL: collimating lens, DCM: Dichroic mirror, AL: Achromatic lens, LP: Linear polarizers, M: Mirror, L: Lens, C: Camera.

The system uses 4 high-powered near infrared LED on Metal-Core PCB with center wavelengths of 660 nm, 735 nm, 865 nm, and 970 nm purchased from Thorlab Inc. The first three wavelengths are very commonly used in the spectroscopic and diffuse optical community to measure tissue hemodynamics. It is the addition of the 970 nm LED that enables IR-SFDI to be sensitive to water. Although stronger absorption peaks for water lie in the SWIR region (near 1150, 1450, and 1900 nm), water has a smaller absorption features near 970 nm. Figure 5.2 shows tissue absorption spectra which shows that water has very low absorption below 900 nm, but peaks at 970 nm¹³¹.

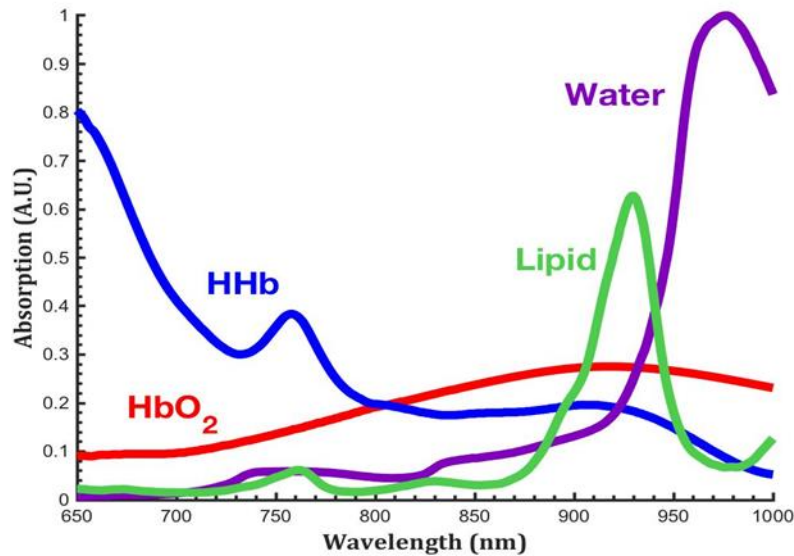


Figure 5.2: Water, lipid, oxyhemoglobin (HbO₂) and deoxyhemoglobin (Hb) absorption peaks in the VIS-NIR region.

The system utilizes digital micromirror devices (DMD) to project patterns onto the sample. DMDs have an array of mirrors that can be individually addressed and tilted to direct and pattern the illumination field. The DMD chosen for IR-SFDI (LC4500, Keynote Photonics) is available as a small DMD chipset with a 0.45" WXGA DMD. The DMD controller is provided on a separate printed circuit board. A pair of orthogonal linear polarizers was used in the illumination and imaging paths to reduce specular reflection from the sample surface⁵⁵.

The camera used in the system (BlackFly-S BFS-U3-13Y3M-C, FLIR, Wilsonville, OR) is a 1280 X 1024 pixel, 10-bit, monochromatic CCD camera chosen because it is relatively low-cost and can easily interface with LabView. Additionally, it allows for low-level control of the image acquisition which makes it possible to turn off automatic

corrections that might lead to nonlinear output. Although the camera only provided a 5% quantum efficiency at 970 nm LED, it will be shown that the camera, although low cost, is able to measure tissue absorption at this wavelength.

5.2.2 IR-SFDI software: Image acquisition

IR-SFDI was designed to make it easy to rapidly begin acquiring SFDI data. To that end, a LabView acquisition code was developed that will run out of the box with any camera supported by IMAQdx. The software has options for collecting multiple measurements, selecting wavelengths, choosing spatial frequencies, and allows users to choose the orientation of the spatially projected patterns, shown in Fig. 5.3. The Labview code controls LEDs through an Arduino, creates 1D sinusoidal pattern and projects that with the DMD, takes images with the camera and upon acquisition stores the SFDI images. Exposure time was kept within 50ms for each LED (660nm: 30ms, 735nm: 30ms, 865nm: 30ms, 970nm: 50ms). Measurements were taken at DC ($f_x=0 \text{ mm}^{-1}$) and 0.1 mm^{-1} spatial frequencies. Currently, the system field of view is 7.5 by 4.5cm.

5.2.3 IR-SFDI data processing

Data processing for IR-SFDI is in most cases was kept the same as SFDI measurements used in previous chapters, except for the calibration phantom and the use of an in-frame phantom. A 10% intralipid liquid phantom (10% lipid, 90% water) was used as calibration phantom for which optical properties were collected from the literature¹³². Absorption and scattering of 100% water and 100% lipid were taken from literature^{132,133}. Like fine tuning described in section 2.2.7, here an additional 10% intralipid phantom (referred to as in-

frame phantom) was used in the FOV during measurements. The measured calibrated reflectance (R_d) image was adjusted by a correction factor determined by the difference between the measured R_d of the 10% intralipid in-frame phantom and the expected R_d calculated from known optical properties found in the literature^{132,133}.

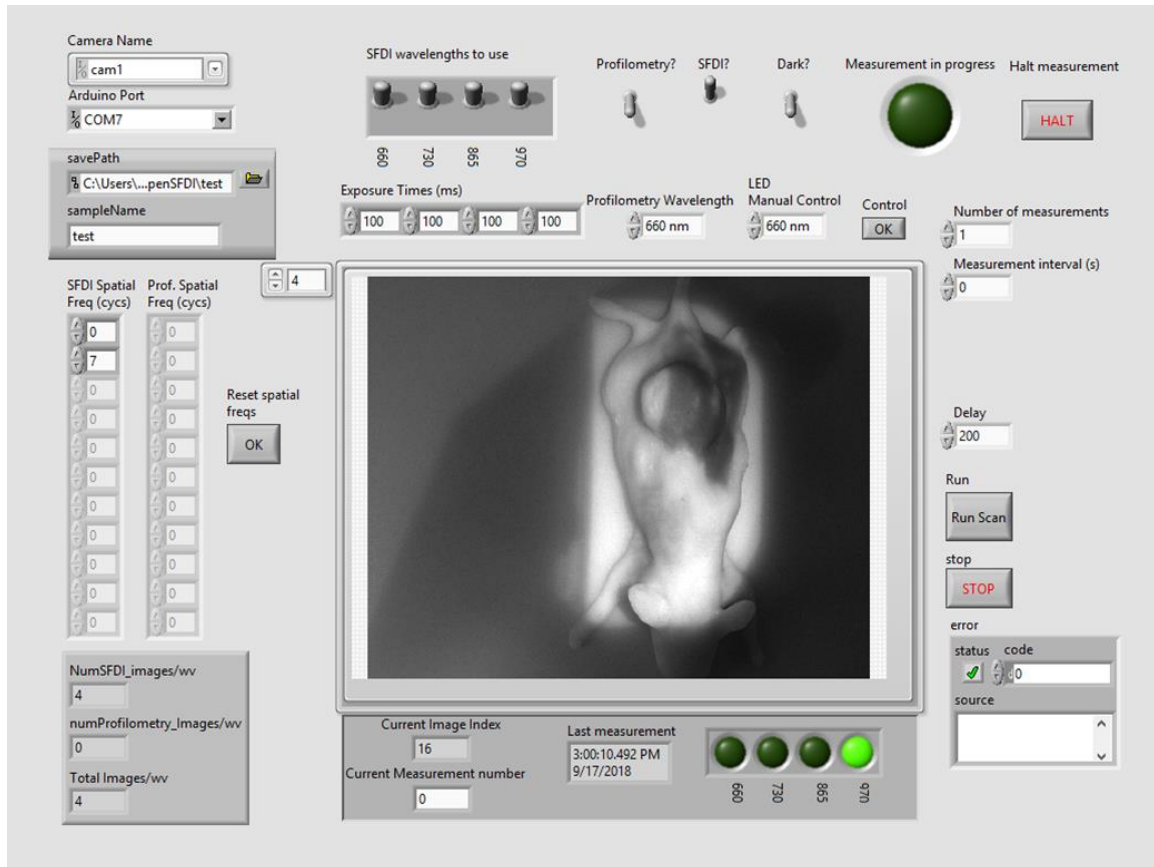


Figure 5.3: IR-SFDI labview code for image acquisition and storage¹. The figure measured raw image of a 3D printed phantom in the field of view.

5.3 Results

5.3.1 LED power stability

The LED optical output power can be unstable due to thermal effects and/or instability of the driving current. IR-SFDI utilizes heatsinks to stabilize the temperature of the LEDs, to account for overheating issues during longitudinal repeated measurements or long

exposure times. Both of these scenarios can lead to LED temperature fluctuations resulting in unstable light output. Figure 5.4 shows that the four LEDs used in the system-maintained good stability during 60 measurements over a 10 minutes period. Precision for the four LEDs, calculated as the standard deviation of the longitudinal measurements, were found as 0.046, 0.034, 0.133, and 0.33 mW respectively.

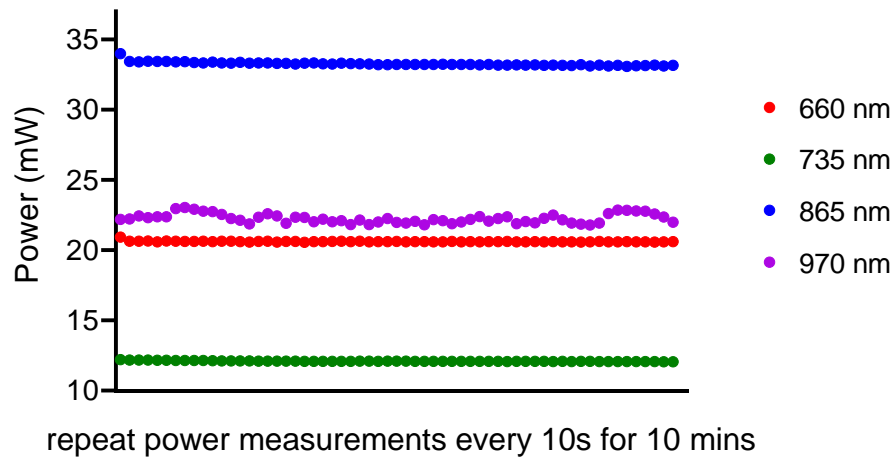


Figure 5.4: Repeat power measurements every 10s for 10 mins for LEDs used in the system.

5.3.2 Reflected intensity

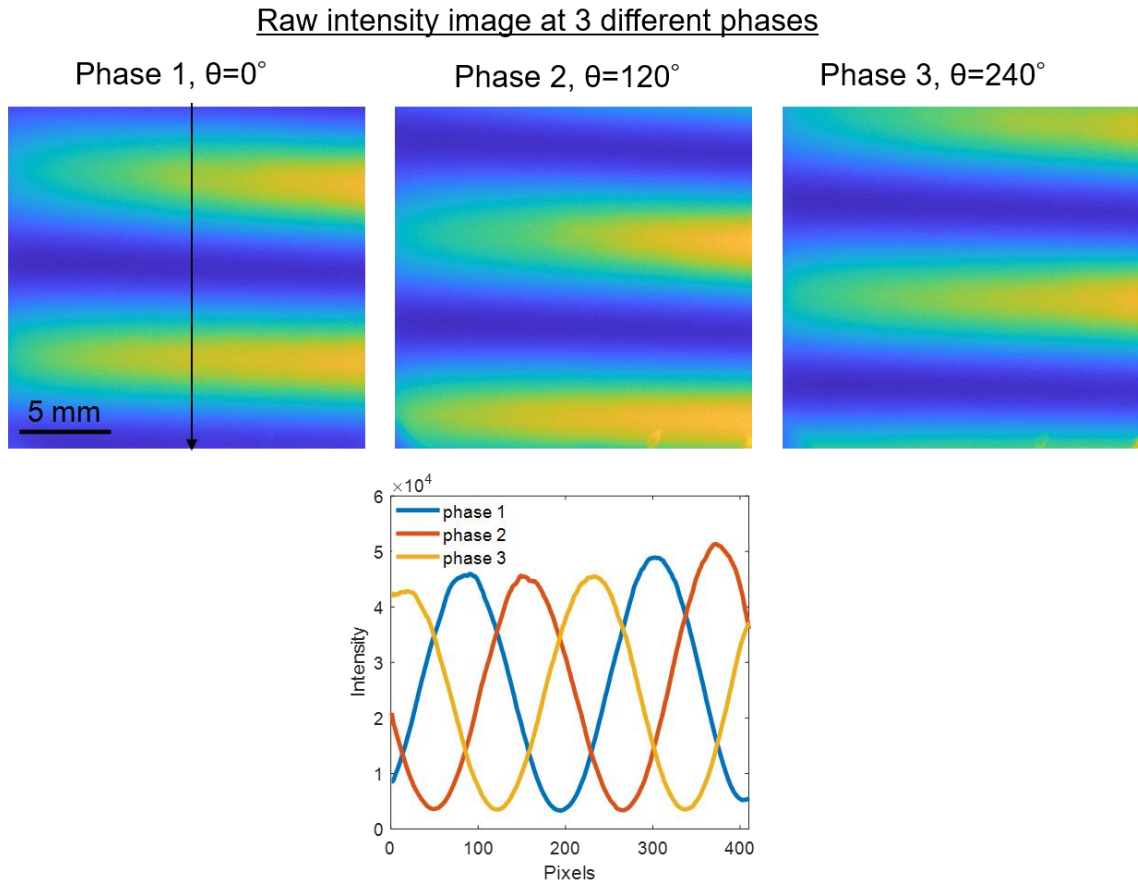


Figure 5.5: A, Reflected intensity images for the 970nm LED acquired at the 3 phases. B, Line profile plots intensity vs. pixels.

Figure 5.5A shows reflected intensity images for the 970nm LED acquired at the 3 phases. The line profile shown in Figure 5.5B shows that the projections at the 3 phases were implemented properly, with each phase having approximately equal amplitude and minimal shape distortion.

5.3.3 Demodulation

Demodulation errors often occur with SFDI, and may be due to unstable illumination sources, non-linearity of projection patterns or camera sensitivity, and others. The 970 nm channel implemented here was challenging due to relatively low power of LED and the low quantum efficiency of the camera at this wavelength. Figure 5.6 shows successfully demodulated images at two 660 nm and 970 nm at two different spatial frequencies.

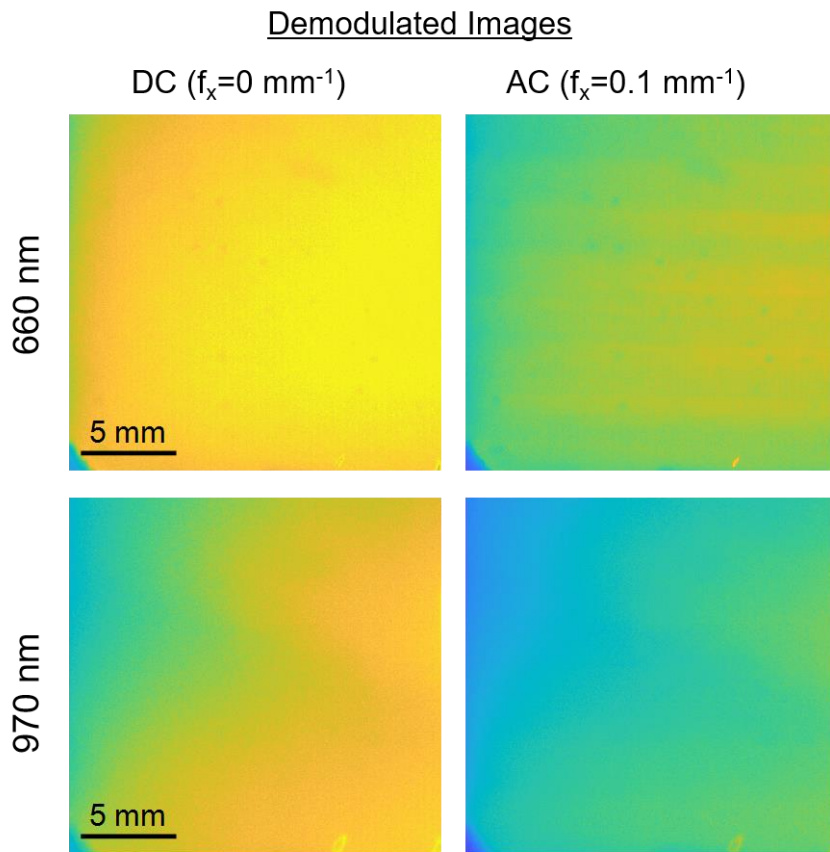


Figure 5.6: Demodulated images at two different wavelengths at two different spatial frequencies.

5.3.4 Optical properties

Figure 5.7 shows extracted optical properties (absorption and reduced scattering) for two LEDs, 865 and 970nm, measured from a 20% intralipid phantom. As expected, absorption at 970 nm is higher than at 865 nm due to the water peak at 970 nm.

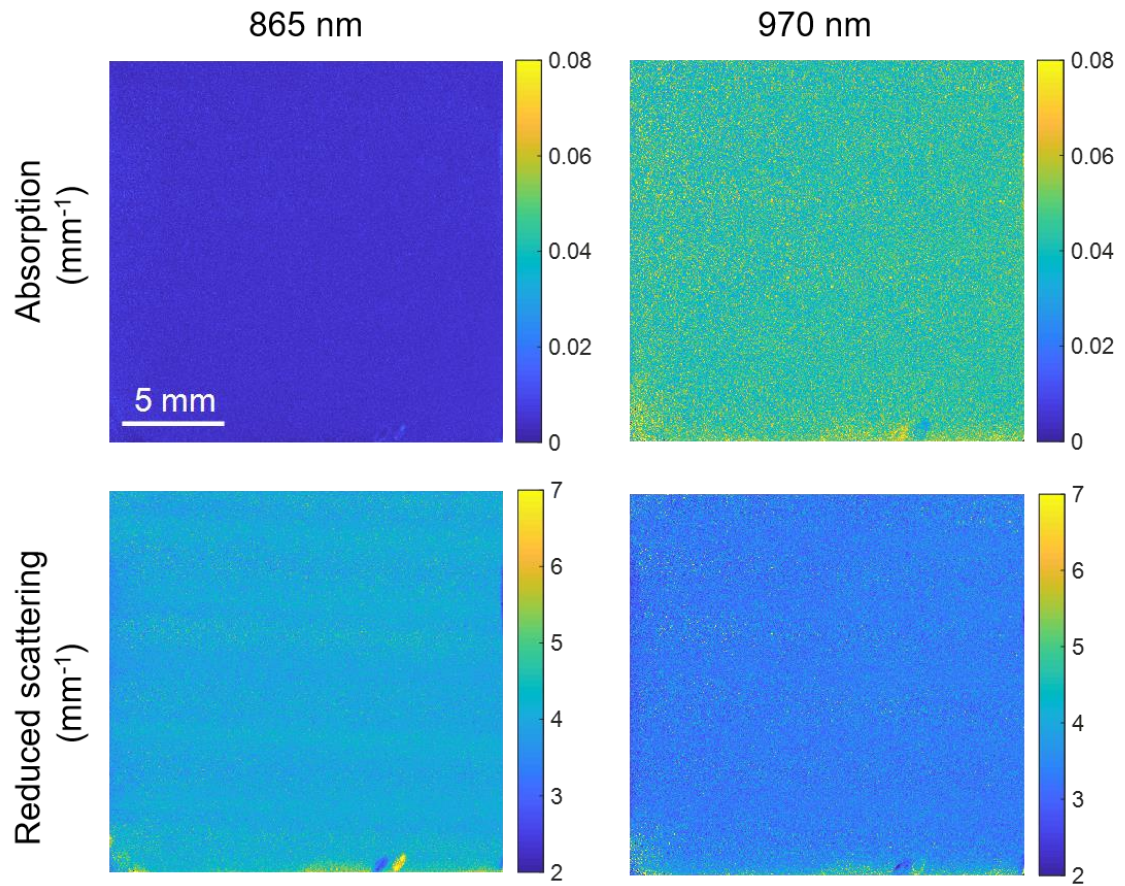


Figure 5.7: Extracted optical properties (absorption and reduced scattering) for two LEDs, 865 and 970nm, measured from a 20% intralipid phantom.

5.3.5 In vitro intralipid testing

Figure 5.9 shows measured absorption along with absorption fit for 10% and 20% intralipid phantoms. Due to very low absorption values at wavelengths less than at 970 nm, a portion

of the extracted optical properties were excluded from analysis due to unrealistic values. As expected, absorption is higher at 970 nm due to the water absorption peak at this wavelength. Scattering increased for the 20% phantom compared to the 10% phantom intralipid phantom due to higher scatterer density.

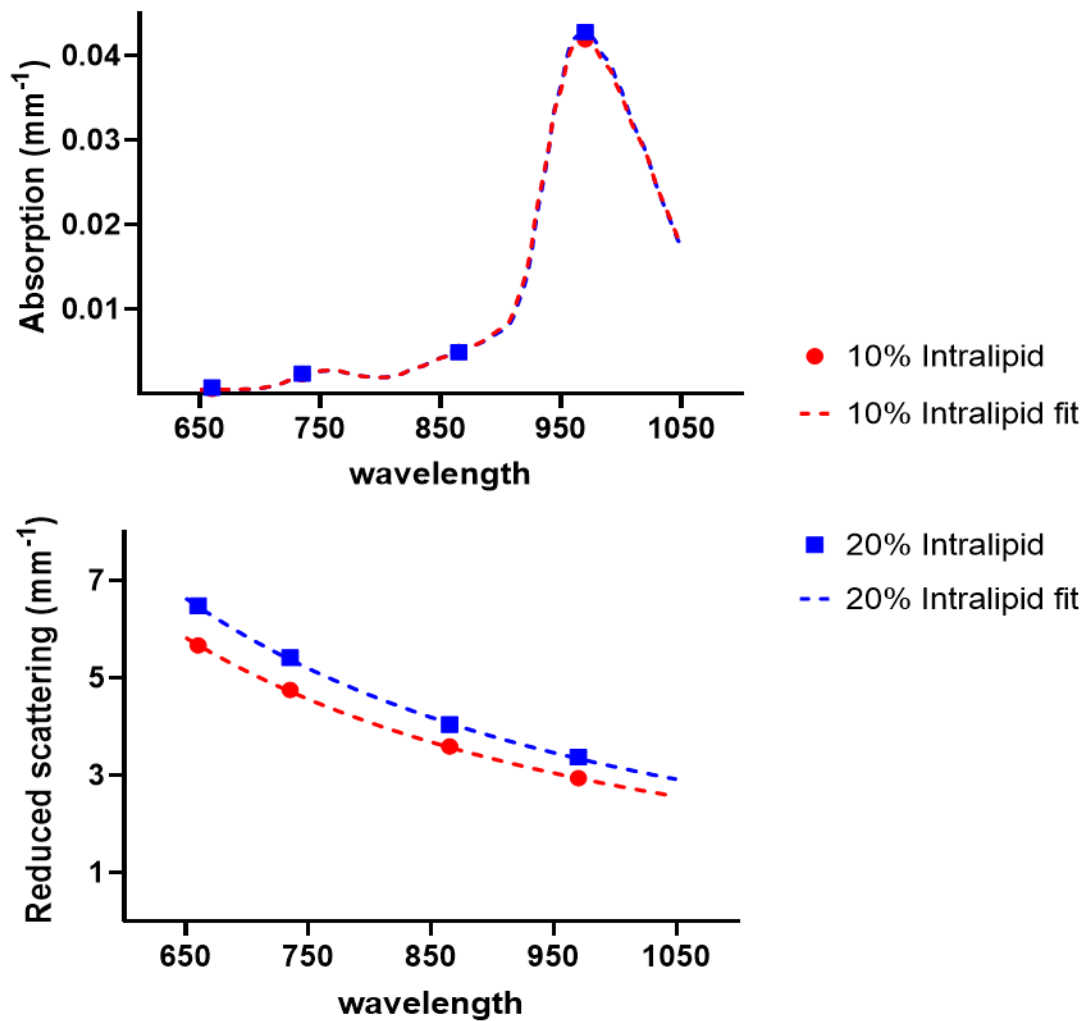


Figure 5.8: Measured and spectral fits of absorption and scattering LEDs.

The absorption fit curves were generated by multiplying measured chromophore values with the 100% water and 100% lipid extinction spectra. Unfortunately, the measured absorption for the two different phantoms are not well discriminated in this case.

5.4 Discussion

In the last chapter of this thesis, we presented preliminary data collected from a new LED-based, cost effective and simple IR-SFDI system. The goal of this new system was to add the capability of measuring water in tumors and other tissue locations. The 1D projection of sinusoids with an 970nm LED was properly implemented by the DMD. The three phase images of the reflected intensity showed that intensity along a line profile within field of view didn't vary with phase, which is a critical factor in 3-phase demodulation. The extracted optical properties showed higher absorption and lower scattering at 970 nm compared to 865 nm, as expected. Spectral data collected from intralipid phantoms showed a higher measured scattering for 20% intralipid than 10% intralipid, as shown in Fig. 5.9, as expected.

In terms of limitations, the accuracy plots showed that the measured absorption couldn't separate 10% intralipid from 20% intralipid phantom, although the spectral shape of intralipid matched the expected shape. A number of issues may have caused the imperfect fitting of water and lipid, including limitations in the current phantom measurement setup or in the current inverse model, which has not yet been extensively tested for this wavelength range.

5.5 Conclusions

The next steps in this project will be to improve absorption fitting for more accurate water and lipid concentration extractions. There is possibility to improve more on measurement accuracy by adding more LEDs in the VIS-NIR region. In future, this system will have multiple applications in our laboratory, including monitor changes in water and hemodynamics in small animal and/or human skin.

CHAPTER SIX

Conclusions

This final chapter summarizes the conclusions from this body of work and offers potential directions for related future work.

6.1 Discussion

SFDI is a wide-field Diffuse Optical Imaging (DOI) modality, capable of tracking the same optical metrics (absorption and scattering) measured using clinical DOI modalities and is well suited for preclinical oncology work. This work established the feasibility of using SFDI for frequent longitudinal monitoring of chemotherapy and targeted therapy efficacy in small animal oncology models. Following that, this work also improved SFDI optical property accuracy in subcutaneous tumor by introducing a new inversion model. This work later validated the SFDI optical and functional metrics in the context of cellular and molecular correlates and explored the treatment prediction ability of SFDI parameters earlier than tumor volume or improve total predictability in combination with tumor volume. Novel findings of this body of work is that SFDI scattering parameters solely, in a non-invasive and label-free manner, may track tumor volume changes by being sensitive to important tumor physiology such as apoptosis and proliferation. Although the scattering parameters were mostly unexplored in the context of treatment monitoring until now, findings of this work introduced these potential new optical markers for cancer to be tested in the clinic for breast and other tumor types with the clinical DOI tools. Another novelty of this work that the scattering a parameter can be combined with the tumor volume information to evaluate outcome of treatment response.

Lastly, this work described a custom light-emitting diode (LED) based SFDI system to acquire measurements in the VIS-NIR spectral region and measure tissue water content, referred to as IR-SFDI. The novelty of this system lies in proper intensity modulation and 3 phase demodulations of the 970nm LED and keeping the system cost within \$5K. Overall, this work advances preclinical cancer treatment monitoring with SFDI. Upon successful clinical translation and validation, knowledge from this work may help clinical DOI tools provide better feedback in the application of treatment monitoring.

6.2 Future directions

Biological

1. Explore if SFDI a and b parameter can track tumor volume changes in other subcutaneous preclinical tumor models
2. Track tumor rebound post-treatment with a and b parameters in multiple preclinical tumor models
3. Track tumor resistance post treatment with a and b parameters in multiple preclinical tumor models
4. Adapt frequency and dosing of treatment in mice based on real-time feedback of SFDI
5. Monitor tumor hemodynamics and water in subcutaneous preclinical tumor models using IR-SFDI

Algorithmic

1. A limitation of the two-layer LUT based inverse model is that it only accounted for skin as a single layer, whereas a more complex model might include separate epidermis, dermis, and hypodermis layers in addition to the tumor layer. A more complex layered

model might improve optical property extraction accuracy using the Gardner et al. method.

2. Expand the scope of the two-layer LUT based inverse model to other tumor types and/or, by accounting the skin layer thickness and optical properties as free parameters.

Technical

1. Improve measurement accuracy and precision of IR-SFDI
2. Expand scope of IR-SFDI and measure other endogenous markers by implementing the appropriate wavelengths in the system, including lipids (930nm, 1210nm) and collagen (1180nm)
3. Design and develop IR-SFDI gen2 that can be portable

BIBLIOGRAPHY

1. M. B. Applegate, "OPEN SFDI Step-by-step instructions for building an SFDI system," 2019, <<http://opensfdi.org/>>.
2. "American Cancer Society. Cancer Facts & Figures 2019. Atlanta: American Cancer Society; 2019."
3. "Noone AM, Howlader N, Krapcho M, Miller D, Brest A, Yu M, Ruhl J, Tatalovich Z, Mariotto A, Lewis DR, Chen HS, Feuer EJ, Cronin KA (eds). SEER Cancer Statistics Review, 1975-2015, National Cancer Institute. Bethesda, MD, https://seer.cancer.gov/csr/1975_2."
4. A. M. Cook et al., "Chemotherapy and immunotherapy: Mapping the road ahead," in *Current Opinion in Immunology* (2016) [doi:10.1016/j.coi.2015.12.003].
5. F. S. Liu, "Mechanisms of Chemotherapeutic Drug Resistance in Cancer Therapy- A Quick Review," in *Taiwanese Journal of Obstetrics and Gynecology* (2009) [doi:10.1016/S1028-4559(09)60296-5].
6. "American Cancer Society. Cancer Facts & Figures 2016. Atlanta: American Cancer Society; 2016."
7. J. Sheng et al., "The efficacy of combining antiangiogenic agents with chemotherapy for patients with advanced non-small cell lung cancer who failed first-line chemotherapy: A systematic review and meta-analysis," in *PLoS ONE* (2015) [doi:10.1371/journal.pone.0127306].
8. E. Diamond et al., "Cytotoxic chemotherapy in the treatment of advanced renal cell carcinoma in the era of targeted therapy," in *Critical Reviews in Oncology/Hematology* (2015) [doi:10.1016/j.critrevonc.2015.08.007].
9. K. Lien et al., "Low-dose metronomic chemotherapy: A systematic literature analysis," *European Journal of Cancer* (2013) [doi:10.1016/j.ejca.2013.06.038].
10. C. Peters and S. Brown, "Antibody-drug conjugates as novel anti-cancer chemotherapeutics," in *Bioscience Reports* (2015) [doi:10.1042/BSR20150089].
11. C. Holohan et al., "Cancer drug resistance: An evolving paradigm," in *Nature Reviews. Cancer* (2013) [doi:10.1038/nrc3599].
12. X. X. Sun and Q. Yu, "Intra-tumor heterogeneity of cancer cells and its implications for cancer treatment," in *Acta Pharmacologica Sinica* (2015)

[doi:10.1038/aps.2015.92].

13. M. S. Linet et al., “Cancer risks associated with external radiation from diagnostic imaging procedures,” *CA. A Cancer Journal for Clinicians* **62**(2), 75–100 (2012) [doi:10.3322/caac.21132].
14. F. Kiessling et al., “Recent advances in molecular, multimodal and theranostic ultrasound imaging,” in *Advanced Drug Delivery Reviews* **72**, pp. 15–27 (2014) [doi:10.1016/j.addr.2013.11.013].
15. Y. Minami and M. Kudo, “Imaging modalities for assessment of treatment response to nonsurgical hepatocellular carcinoma therapy: Contrast-enhanced US, CT, and MRI,” *Liver Cancer* **4**(2), 106–114 (2015) [doi:10.1159/000367733].
16. E. Yeh et al., “Prospective comparison of mammography, sonography, and MRI in patients undergoing neoadjuvant chemotherapy for palpable breast cancer,” *American Journal of Roentgenology* (2005) [doi:10.2214/ajr.184.3.01840868].
17. A. A. Tardivon et al., “Monitoring therapeutic efficacy in breast carcinomas,” *European Radiology* (2006) [doi:10.1007/s00330-006-0317-z].
18. P. J. Drew et al., “Evaluation of response to neoadjuvant chemoradiotherapy for locally advanced breast cancer with dynamic contrast-enhanced MRI of the breast,” *European Journal of Surgical Oncology* (2001) [doi:10.1053/ejso.2001.1194].
19. M. Tozaki et al., “Predicting pathological response to neoadjuvant chemotherapy in breast cancer with quantitative ¹H MR spectroscopy using the external standard method,” *Journal of Magnetic Resonance and Imaging* (2010) [doi:10.1002/jmri.22118].
20. S. Preibisch, S. Saalfeld, and P. Tomancak, “Globally optimal stitching of tiled 3D microscopic image acquisitions,” *Bioinformatics* (2009) [doi:10.1093/bioinformatics/btp184].
21. J. A. Cintolo, J. Tchou, and D. A. Pryma, “Diagnostic and prognostic application of positron emission tomography in breast imaging: Emerging uses and the role of PET in monitoring treatment response,” in *Breast Cancer Research and Treatment* (2013) [doi:10.1007/s10549-013-2451-z].
22. X. Sun et al., “¹⁸F-FPPRGD2 and ¹⁸F-FDG PET of response to Abraxane therapy,” *Journal of Nuclear Medicine* (2011) [doi:10.2967/jnumed.110.080606].
23. N. Cho et al., “Early prediction of response to neoadjuvant chemotherapy in breast cancer patients: comparison of single-voxel (1)H-magnetic resonance spectroscopy

- and (18)F-fluorodeoxyglucose positron emission tomography.,” *European Radiology* (2015) [doi:10.1007/s00330-015-4014-7].
24. I. J. Chou et al., “Subjective discomfort in children receiving 3 T MRI and experienced adults’ perspective on children’s tolerability of 7 T: A cross-sectional questionnaire survey,” *BMJ Open* **4**(10) (2014) [doi:10.1136/bmjopen-2014-006094].
 25. T. D. O’Sullivan et al., “Diffuse optical imaging using spatially and temporally modulated light,” *Journal of Biomedical Optics* **17**(7), 0713111 (2012) [doi:10.1117/1.JBO.17.7.071311].
 26. T. Durduran et al., “Diffuse optics for tissue monitoring and tomography,” in *Reports on Progress in Physics* **73**(7) (2010) [doi:10.1088/0034-4885/73/7/076701].
 27. S. L. Jacques and B. W. Pogue, “Tutorial on diffuse light transport,” *Journal of Biomedical Optics* (2008) [doi:10.1117/1.2967535].
 28. B. E. Schaafsma et al., “Optical mammography using diffuse optical spectroscopy for monitoring tumor response to neoadjuvant chemotherapy in women with locally advanced breast cancer.,” *Clinical Cancer Research* **21**(3), 577–584 (2015) [doi:10.1158/1078-0432.CCR-14-0736].
 29. S. Jiang et al., “Predicting breast tumor response to neoadjuvant chemotherapy with diffuse optical spectroscopic tomography prior to treatment.,” *Clinical Cancer Research* **20**(23), 6006–6015 (2014) [doi:10.1158/1078-0432.CCR-14-1415].
 30. S. Ueda et al., “Baseline tumor oxygen saturation correlates with a pathologic complete response in breast cancer patients undergoing neoadjuvant chemotherapy,” *Cancer Research* **72**(17), 4318–4328 (2012) [doi:10.1158/0008-5472.CAN-12-0056].
 31. A. Cerussi et al., “Predicting response to breast cancer neoadjuvant chemotherapy using diffuse optical spectroscopy.” *Proceedings of the National Academy of Sciences of the United States of America* **104**(10), 4014–4019 (2007) [doi:10.1073/pnas.0611058104].
 32. B. W. Pogue et al., “Quantitative Hemoglobin Tomography with Diffuse Near-Infrared Spectroscopy: Pilot Results in the Breast,” *Radiology* **218**(1), 261–266 (2001) [doi:10.1148/radiology.218.1.r01ja51261].
 33. H. Soliman et al., “Functional imaging using diffuse optical spectroscopy of neoadjuvant chemotherapy response in women with locally advanced breast cancer,” *Clinical Cancer Research* **16**(9), 2605–2614 (2010) [doi:10.1158/1078-

0432.CCR-09-1510].

34. Q. Zhu et al., “Noninvasive monitoring of breast cancer during neoadjuvant chemotherapy using optical tomography with ultrasound localization,” *Neoplasia* **10**(10), 1028–1040 (2008) [doi:10.1593/neo.08602].
35. D. Roblyer et al., “Optical imaging of breast cancer oxyhemoglobin flare correlates with neoadjuvant chemotherapy response one day after starting treatment,” *Proceedings of the National Academy of Sciences of the United States of America* **108**(35), 14626–14631 (2011) [doi:10.1073/pnas.1013103108].
36. M. G. Pakalniskis et al., “Tumor angiogenesis change estimated by using diffuse optical spectroscopic tomography: Demonstrated correlation in women undergoing neoadjuvant chemotherapy for invasive breast cancer?” *Radiology* (2011) [doi:10.1148/radiol.11100699].
37. S. H. Chung et al., “Macroscopic optical physiological parameters correlate with microscopic proliferation and vessel area breast cancer signatures,” *Breast Cancer Research* **17**(1) (2015) [doi:10.1186/s13058-015-0578-z].
38. C. K. Hayakawa et al., “Optical sampling depth in the spatial frequency domain,” *Journal of Biomedical Optics* (2018) [doi:10.1117/1.jbo.24.7.071603].
39. K. P. Nadeau et al., “Quantitative assessment of renal arterial occlusion in a porcine model using spatial frequency domain imaging,” *Optics Letters* **38**(18), 3566 (2013) [doi:10.1364/OL.38.003566].
40. A. Ponticorvo et al., “Quantitative assessment of partial vascular occlusions in a swine pedicle flap model using spatial frequency domain imaging,” *Biomedical Optics Express* **4**, 298–306 (2013) [doi:10.1364/BOE.4.000298].
41. J. Q. Nguyen et al., “Spatial frequency domain imaging of burn wounds in a preclinical model of graded burn severity,” *Journal of Biomedical Optics* **18**(6), 066010 (2013) [doi:10.1117/1.JBO.18.6.066010].
42. Y. Zhao and D. Roblyer, “Spatial mapping of fluorophore quantum yield in diffusive media,” *Journal of Biomedical Optics* **20**(8), 86013 (2015) [doi:10.1117/1.JBO.20.8.086013].
43. U. Sunar et al., “Quantification of PpIX concentration in basal cell carcinoma and squamous cell carcinoma models using spatial frequency domain imaging,” *Biomedical Optics Express* **4**(4), 531–537 (2013) [doi:10.1364/BOE.4.000531].
44. A. Yafi et al., “Postoperative quantitative assessment of reconstructive tissue status in a cutaneous flap model using spatial frequency domain imaging,” *Plastic and*

- Reconstructive Surgery (2011) [doi:10.1097/PRS.0b013e3181f959cc].
45. S. Gioux et al., “First-in-human pilot study of a spatial frequency domain oxygenation imaging system,” *Journal of Biomedical Optics* (2011) [doi:10.1117/1.3614566].
 46. A. J. Lin et al., “Spatial frequency domain imaging of intrinsic optical property contrast in a mouse model of alzheimer’s disease,” *Annals of Biomedical Engineering* (2011) [doi:10.1007/s10439-011-0269-6].
 47. R. P. Singh-Moon et al., “Spatial mapping of drug delivery to brain tissue using hyperspectral spatial frequency-domain imaging,” *Journal of Biomedical Optics* (2014) [doi:10.1117/1.jbo.19.9.096003].
 48. D. J. Rohrbach et al., “Preoperative Mapping of Nonmelanoma Skin Cancer Using Spatial Frequency Domain and Ultrasound Imaging,” *Academic Radiology* **21**(2), 263–270 (2014) [doi:10.1016/j.acra.2013.11.013.Preoperative].
 49. S. D. Konecky et al., “Spatial frequency domain tomography of protoporphyrin IX fluorescence in preclinical glioma models,” *Journal of Biomedical Optics* **17**(5), 056008 (2012) [doi:10.1117/1.JBO.17.5.056008].
 50. A. M. Laughney et al., “Scatter spectroscopic imaging distinguishes between breast pathologies in tissues relevant to surgical margin assessment,” *Clinical Cancer Research* (2012) [doi:10.1158/1078-0432.CCR-12-0136].
 51. R. B. Saager et al., “Quantitative fluorescence imaging of protoporphyrin IX through determination of tissue optical properties in the spatial frequency domain,” *Journal of Biomedical Optics* (2011) [doi:10.1117/1.3665440].
 52. S. Tabassum et al., “Feasibility of spatial frequency domain imaging (SFDI) for optically characterizing a preclinical oncology model,” *Biomedical Optics Express* **7**(10) (2016) [doi:10.1364/BOE.7.004154].
 53. S. Tabassum et al., “Two-layer inverse model for improved longitudinal preclinical tumor imaging in the spatial frequency domain,” *Journal of Biomedical Optics* (2018) [doi:10.1117/1.jbo.23.7.076011].
 54. K. Zhang and D. J. Waxman, “Impact of Tumor Vascularity on Responsiveness to Antiangiogenesis in a Prostate Cancer Stem Cell-Derived Tumor Model,” *Molecular Cancer Therapeutics* **12**(5), 787–798 (2013) [doi:10.1158/1535-7163.MCT-12-1240].
 55. D. J. Cuccia et al., “Quantitation and mapping of tissue optical properties using modulated imaging,” *Journal of Biomedical Optics* **14**(2), 024012 (2009)

[doi:10.1117/1.3088140].

56. S. Gioux et al., “Three-dimensional surface profile intensity correction for spatially modulated imaging,” *Journal of Biomedical Optics* (2009) [doi:10.1117/1.3156840].
57. Y. Zhao et al., “Angle correction for small animal tumor imaging with spatial frequency domain imaging (SFDI),” *Biomedical Optics Express* **7**(6) (2016) [doi:10.1364/BOE.7.002373].
58. C. E. Meacham and S. J. Morrison, “Tumour heterogeneity and cancer cell plasticity,” in *Nature* (2013) [doi:10.1038/nature12624].
59. W. G. Zijlstra and A. Buursma, “Spectrophotometry of hemoglobin: Absorption spectra of bovine oxyhemoglobin, deoxyhemoglobin, carboxyhemoglobin, and methemoglobin,” *Comparative Biochemistry and Physiology. Part B, Biochemistry & Molecular Biology* (1997) [doi:10.1016/S0305-0491(97)00230-7].
60. A. Mazhar et al., “Wavelength optimization for rapid chromophore mapping using spatial frequency domain imaging,” *Journal of Biomedical Optics* (2010) [doi:10.1117/1.3523373].
61. H.-W. Wang et al., “Treatment-Induced Changes in Tumor Oxygenation Predict Photodynamic Therapy Outcome,” *Cancer Research*. **64**(20), 7553–7561 (2004) [doi:10.1158/0008-5472.CAN-03-3632].
62. U. Sunar et al., “Hemodynamic responses to antivasular therapy and ionizing radiation assessed by diffuse optical spectroscopies,” *Optics Express* **15**(23), 15507–15516 (2007) [doi:10.1364/OE.15.015507].
63. K. Vishwanath et al., “Using Optical Spectroscopy to Longitudinally Monitor Physiological Changes within Solid Tumors,” *Neoplasia* **11**(9), 889–900 (2009) [doi:10.1593/neo.09580].
64. S. D. Konecky et al., “Quantitative optical tomography of sub-surface heterogeneities using spatially modulated structured light,” *Optics Express* **17**(17), 14780 (2009) [doi:10.1364/OE.17.014780].
65. J. Condeelis and R. Weissleder, “In vivo imaging in cancer,” in *Cold Spring Harbor Perspectives in Biology* **2**(12) (2010) [doi:10.1101/cshperspect.a003848].
66. T. L. Becker et al., “Monitoring blood flow responses during topical ALA-PDT,” *Biomedical Optics Express* **2**(1), 123–130 (2010) [doi:10.1364/BOE.2.000123].

67. M. L. Flexman et al., “Monitoring early tumor response to drug therapy with diffuse optical tomography,” *Journal of Biomedical Optics* **17**(1), 016014 (2012) [doi:10.1117/1.JBO.17.1.016014].
68. C. K. Hayakawa et al., “Perturbation Monte Carlo methods to solve inverse photon migration problems in heterogeneous tissues,” *Optics Letters* **26**(17), 1335 (2001) [doi:10.1364/OL.26.001335].
69. J. R. Weber et al., “Noncontact imaging of absorption and scattering in layered tissue using spatially modulated structured light,” *Journal of Applied Physics* **105**(10) (2009) [doi:10.1063/1.3116135].
70. R. B. Saager et al., “*In vivo* isolation of the effects of melanin from underlying hemodynamics across skin types using spatial frequency domain spectroscopy,” *Journal of Biomedical Optics* **21**(5), 057001 (2016) [doi:10.1117/1.JBO.21.5.057001].
71. D. Yudovsky and A. J. Durkin, “Spatial frequency domain spectroscopy of two layer media,” *Journal of Biomedical Optics* **16**(10), 107005 (2011) [doi:10.1117/1.3640814].
72. D. Yudovsky, J. Q. M. Nguyen, and A. J. Durkin, “*In vivo* spatial frequency domain spectroscopy of two layer media,” *Journal of Biomedical Optics* **17**(10), 107006 (2012) [doi:10.1117/1.JBO.17.10.107006].
73. V. Pera et al., “Optical property uncertainty estimates for spatial frequency domain imaging,” *Biomedical Optics Express* **9**(2) (2018) [doi:10.1364/BOE.9.000661].
74. M. Martinelli et al., “Analysis of single Monte Carlo methods for prediction of reflectance from turbid media,” *Optics Express* **19**(20), 19627 (2011) [doi:10.1364/OE.19.019627].
75. A. R. Gardner and V. Venugopalan, “Accurate and efficient Monte Carlo solutions to the radiative transport equation in the spatial frequency domain,” *Optics Letters* **36**(12), 2269 (2011) [doi:10.1364/OL.36.002269].
76. C. P. Sabino et al., “The optical properties of mouse skin in the visible and near infrared spectral regions,” *Journal of Photochemistry and Photobiology. B, Biology* **160**, 72–78 (2016) [doi:10.1016/j.jphotobiol.2016.03.047].
77. S. M. Marques et al., “Genetic background determines mouse strain differences in inflammatory angiogenesis,” *Microvascular Research* **82**(3), 246–252 (2011) [doi:10.1016/j.mvr.2011.08.011].

78. L. Azzi et al., “Gender differences in mouse skin morphology and specific effects of sex steroids and dehydroepiandrosterone.,” *Journal of Investigative Dermatology* **124**(1), 22–27 (2005) [doi:10.1111/j.0022-202X.2004.23545.x].
79. K. Calabro et al., “Gender variations in the optical properties of skin in murine animal models,” *Journal of Biomedical Optics* **16**(1), 011008 (2011) [doi:10.1117/1.3525565].
80. L. S. Hansen et al., “The influence of the hair cycle on the thickness of mouse skin,” *Anatomical Record* **210**(4), 569–573 (1984) [doi:10.1002/ar.1092100404].
81. T. D. Dodig et al., “Development of the tight-skin phenotype in immune-deficient mice,” *Arthritis and Rheumatism* **44**(3), 723–727 (2001) [doi:10.1002/1529-0131(200103)44:3<723::AID-ANR122>3.0.CO;2-V].
82. M. A. Ansari et al., “Diffuse optical tomography: Image reconstruction and verification,” *Journal of Lasers in Medical Sciences* **5**(1), 13–18 (2014).
83. F. Ayers et al., “Fabrication and characterization of silicone-based tissue phantoms with tunable optical properties in the visible and near infrared domain,” *Proceedings of SPIE* **6870**, 07-1-7–9 (2008) [doi:10.1117/12.764969].
84. R. B. Saager et al., “Multilayer silicone phantoms for the evaluation of quantitative optical techniques in skin imaging,” *Proceedings of SPIE* **7567** (2010) [doi:10.1117/12.842249].
85. G. J. Greening et al., “Characterization of thin poly(dimethylsiloxane)-based tissue-simulating phantoms with tunable reduced scattering and absorption coefficients at visible and near-infrared wavelengths,” *Journal of Biomedical Optics* **19**(11), 115002 (2014) [doi:10.1117/1.JBO.19.11.115002].
86. R. B. Saager et al., “Method for depth-resolved quantitation of optical properties in layered media using spatially modulated quantitative spectroscopy,” *Journal of Biomedical Optics* **16**(7), 077002 (2011) [doi:10.1117/1.3597621].
87. D. Yudovsky and A. J. Durkin, “Spatial frequency domain spectroscopy of two layer media,” *Journal of Biomedical Optics* **16**(10), 107005 (2011) [doi:10.1117/1.3640814].
88. B. J. Tromberg et al., “Predicting responses to neoadjuvant chemotherapy in breast cancer: ACRIN 6691 trial of diffuse optical spectroscopic imaging,” *Cancer Research* (2016) [doi:10.1158/0008-5472.CAN-16-0346].
89. J. R. Mourant et al., “Predictions and measurements of scattering and absorption over broad wavelength ranges in tissue phantoms,” *Applied Optics* (1997)

- [doi:10.1364/ao.36.000949].
90. J. R. Mourant et al., “Mechanisms of light scattering from biological cells relevant to noninvasive optical-tissue diagnostics,” *Applied Optics* (1998) [doi:10.1364/ao.37.003586].
 91. B. Beauvoit et al., “Characterization of absorption and scattering properties for various yeast strains by time-resolved spectroscopy,” *Cell Biophysics* (1993) [doi:10.1007/BF02796508].
 92. G. J. Greening et al., “Effects of isoflurane anesthesia on physiological parameters in murine subcutaneous tumor allografts measured via diffuse reflectance spectroscopy,” *Biomedical Optics Express* (2018) [doi:10.1364/boe.9.002871].
 93. M. Franco et al., “Targeted anti-vascular endothelial growth factor receptor-2 therapy leads to short-term and long-term impairment of vascular function and increase in tumor hypoxia,” *Cancer Research* (2006) [doi:10.1158/0008-5472.CAN-05-3295].
 94. J. Ma and D. J. Waxman, “Dominant effect of antiangiogenesis in combination therapy involving cyclophosphamide and axitinib,” *Clinical Cancer Research* (2009) [doi:10.1158/1078-0432.CCR-08-1174].
 95. C. S. Chen, J. C. Doloff, and D. J. Waxman, “Intermittent metronomic drug schedule is essential for activating antitumor innate immunity and tumor xenograft regression,” *Neoplasia* (2014) [doi:10.1593/neo.131910].
 96. J. Schindelin et al., “Fiji: An open-source platform for biological-image analysis,” *Nature Methods* (2012) [doi:10.1038/nmeth.2019].
 97. D. Roblyer et al., “Comparison of multispectral wide-field optical imaging modalities to maximize image contrast for objective discrimination of oral neoplasia,” *Journal of Biomedical Optics* (2010) [doi:10.1117/1.3516593].
 98. D. M. de Bruin et al., “Assesment of apoptosis induced changes in scattering using optical coherence tomography,” *Journal of Biophotonics* (2016) [doi:10.1002/jbio.201500198].
 99. G. Farhat et al., “Optical coherence tomography spectral analysis for detecting apoptosis in vitro and in vivo ,” *Journal of Biomedical Optics* (2015) [doi:10.1117/1.jbo.20.12.126001].
 100. S. Srinivasan et al., “Near-infrared characterization of breast tumors in vivo using spectrally-constrained reconstruction,” *Technology in Cancer Research & Treatment* (2005) [doi:10.1177/153303460500400505].

101. Q. Zhu et al., "Utilizing optical tomography with ultrasound localization to image heterogeneous hemoglobin distribution in large breast cancers," *Neoplasia* (2005) [doi:10.1593/neo.04526].
102. A. J. Sankoh, M. F. Huque, and S. D. Dubey, "Some comments on frequently used multiple endpoint adjustment methods in clinical trials," *Statistics in Medicine* (1997) [doi:10.1002/(SICI)1097-0258(19971130)16:22<2529::AID-SIM692>3.0.CO;2-J].
103. S. J. Vinnicombe et al., "Primary breast cancer: Mammographic changes after neoadjuvant chemotherapy, with pathologic correlation," *Radiology* (1996) [doi:10.1148/radiology.198.2.8596827].
104. L. D. Feldman et al., "Pathological Assessment of Response to Induction Chemotherapy in Breast Cancer," *Cancer Research* **46**(5): 2578–2581 (1986).
105. M. A. Helvie et al., "Locally advanced breast carcinoma: Accuracy of mammography versus clinical examination in the prediction of residual disease after chemotherapy," *Radiology* (1996) [doi:10.1148/radiology.198.2.8596826].
106. N. M. Hylton et al., "Locally advanced breast cancer: MR imaging for prediction of response to neoadjuvant chemotherapy - Results from ACRIN 6657/I-SPY TRIAL," *Radiology* (2012) [doi:10.1148/radiol.12110748].
107. T. L. Chenevert, "Diffusion Magnetic Resonance Imaging: an Early Surrogate Marker of Therapeutic Efficacy in Brain Tumors," *Journal of the National Cancer Institute* (2000) [doi:10.1093/jnci/92.24.2029].
108. S. Meisamy et al., "Neoadjuvant chemotherapy of locally advanced breast cancer: Predicting response with in vivo 1H MR spectroscopy - A pilot study at 4 T," *Radiology* (2004) [doi:10.1148/radiol.2332031285].
109. D. A. Mankoff et al., "Changes in blood flow and metabolism in locally advanced breast cancer treated with neoadjuvant chemotherapy," *Journal of Nuclear Medicine* **44**(1): 1806–1814 (2003).
110. G. M. McDermott et al., "Monitoring primary breast cancer throughout chemotherapy using FDG-PET," *Breast Cancer Research and Treatment* (2007) [doi:10.1007/s10549-006-9316-7].
111. N. S. Vasudev and A. R. Reynolds, "Anti-angiogenic therapy for cancer: Current progress, unresolved questions and future directions," in *Angiogenesis* (2014) [doi:10.1007/s10456-014-9420-y].

112. R. E. Cocco and D. S. Ucker, "Distinct modes of macrophage recognition for apoptotic and necrotic cells are not specified exclusively by phosphatidylserine exposure," *Molecular Biology of the Cell* (2001) [doi:10.1091/mbc.12.4.919].
113. R. K. Jain, "Normalization of tumor vasculature: An emerging concept in antiangiogenic therapy," in *Science* (2005) [doi:10.1126/science.1104819].
114. J. Wang et al., "Near-infrared tomography of breast cancer hemoglobin, water, lipid, and scattering using combined frequency domain and cw measurement," *Optics Letters* (2010) [doi:10.1364/ol.35.000082].
115. C. G. Filippi et al., "Appearance of meningiomas on diffusion-weighted images: Correlating diffusion constants with histopathologic findings," *American Journal of Neuroradiology* (2001).
116. K. Kono et al., "The role of diffusion-weighted imaging in patients with brain tumors," *American Journal of Neuroradiology* (2001) [doi:10.18535/jmscr/v6i2.95].
117. M. A. Thomas et al., "Two-dimensional MR spectroscopic characterization of breast cancer in vivo," *Technology in Cancer Research & Treatment* (2005) [doi:10.1177/153303460500400113].
118. A. Baur, O. Dietrich, and M. Reiser, "Diffusion-weighted imaging of bone marrow: Current status," *European Radiology* (2003) [doi:10.1007/s00330-003-1873-0].
119. Y. Paran et al., "Water diffusion in the different microenvironments of breast cancer," *NMR in Biomedicine* (2004) [doi:10.1002/nbm.882].
120. H. Lyng, O. Haraldseth, and E. K. Rofstad, "Measurement of cell density and necrotic fraction in human melanoma xenografts by diffusion weighted magnetic resonance imaging," *Magnetic Resonance in Medicine* (2000) [doi:10.1002/1522-2594(200006)43:6<828::AID-MRM8>3.0.CO;2-P].
121. M. Zhao et al., "Early detection of treatment response by diffusion-weighted ¹H-NMR spectroscopy in a murine tumour in vivo," *British Journal of Cancer* (1996) [doi:10.1038/bjc.1996.11].
122. M. Brauer, "In vivo monitoring of apoptosis," in *Progress in Neuro-Psychopharmacology and Biological Psychiatry* (2003) [doi:10.1016/S0278-5846(03)00026-5].
123. M. C. Papadopoulos et al., "Molecular mechanisms of brain tumor edema," *Neuroscience* (2004) [doi:10.1016/j.neuroscience.2004.05.044].

124. T. J. Allen et al., "Spectroscopic photoacoustic imaging of lipid-rich plaques in the human aorta in the 740 to 1400 nm wavelength range," *Journal of Biomedical Optics* (2012) [doi:10.1117/1.jbo.17.6.061209].
125. J. P. Angelo et al., "Review of structured light in diffuse optical imaging," *Journal of Biomedical Optics* (2018) [doi:10.1117/1.jbo.24.7.071602].
126. S. Gioux, A. Mazhar, and D. J. Cuccia, "Spatial frequency domain imaging in 2019: principles, applications, and perspectives," *Journal of Biomedical Optics* (2019) [doi:10.1117/1.jbo.24.7.071613].
127. R. H. Wilson et al., "Review of short-wave infrared spectroscopy and imaging methods for biological tissue characterization," *Journal of Biomedical Optics* (2015) [doi:10.1117/1.jbo.20.3.030901].
128. R. H. Wilson et al., "Quantitative short-wave infrared multispectral imaging of in vivo tissue optical properties," *Journal of Biomedical Optics* (2014) [doi:10.1117/1.jbo.19.8.086011].
129. C. C. Sahyoun et al., "Short-wave infrared spatial frequency domain imaging for non-invasive quantification of tissue water content," *Proceedings of SPIE* **10874** 2019 [doi:10.1117/12.2510537].
130. Y. Zhao et al., "Label-free, non-invasive mapping of water and lipid content in tissue with Structured Shortwave-infrared Imaging (SSI)," in *Optics InfoBase Conference Papers* (2018) [doi:10.1364/OTS.2018.OF2D.3].
131. "<https://dosi.bli.uci.edu/research/>."
132. S. T. Flock et al., "Optical properties of intralipid: A phantom medium for light propagation studies," *Lasers in Surgery and Medicine* (1992) [doi:10.1002/lsm.1900120510].
133. D. J. Segelstein, "The complex refractive index of water," M.S. Thesis, University of Missouri-Kansas City (1981).
<https://mospace.umsystem.edu/xmlui/handle/10355/11599>

CURRICULUM VITAE

SYEDA TABASSUM

tabassum@bu.edu
www.linkedin.com/in/syeda-tabassum-33720276

[1203 Boylston street](#)
[Apt # 26, Boston, MA 02215](#)
[+1-857-498-9346](#)

EDUCATION

Boston University, USA

- Ph.D. Candidate, Department of Electrical & Computer Engineering Expected Fall 2019
- M.Sc., Department of Electrical & Computer Engineering, CGPA: 3.73 2017

University of Dhaka, Bangladesh

- M.Sc. in Applied Physics, Electronics & Communication Engineering, CGPA: 3.7 2012
- B.Sc. in Applied Physics, Electronics & Communication Engineering, CGPA: 3.668 2010

KEY QUALIFICATIONS

- Hands on experience (6+ years) in optical and photonics instrumentation as evidenced by 6 journal articles, 1 conference proceeding, 3 poster presentations, and 4 oral presentations
- Custom design, develop and validate novel optical devices for biomedical applications
- Develop new Monte-Carlo based algorithms and validate in high performance computing cluster
- Strong experimental skills in working with small animal (mice), human volunteers and breast cancer patients
- Experience in writing Institutional Review Board protocols for experiments with small animal and human subjects
- **Software:** Python, matlab, solidworks, C++, comsol, labview, linux, graphpad prism, arduino, ImageJ, Fiji, microsoft excel, microsoft office
- **Wet chemical Process:** Fabrication of quantum dots, fabrication of nanoparticles, fabrication of diffraction grating
- **Molecular biology techniques:** Cell culture, immunohistochemistry, tissue processing, tissue embedding, tissue sectioning (cryosections, paraffin embedded sections)
- **Small animal procedures:** Experience in long term mouse handling and monitoring (wild type and transgenic mouse), subcutaneous and mammary fat pad tumor inoculation, tail vein injection, retro orbital injection, organ and tissue collection (skin, liver, intestine, tumor), isoflurane and ketamine anesthesia, *in vivo* tumor volume collection
- **Imaging and characterization tools:** Bright field microscopy, fluorescence microscopy, phase contrast microscopy, two-photon microscopy, confocal microscopy, bioluminescence imaging, Spatial Frequency Domain Imaging (SFDI), Diffuse Optical Spectroscopic Imaging (DOSI), optical components alignment, oscilloscope, 3D printing
- **Statistical data analysis:** Mann-Whitney U test, Wilcoxon signed-rank test, ANOVA, non-parametric tests, pearson's and spearman's correlations, Multiple correlations, Multivariate discriminant analysis

RESEARCH EXPERIENCE

Boston University, Boston, USA

Project: Measure tissue water content using **SFDI** 2018-present

- Optics: - Design and build an SFDI optical imaging system using DMD spatial light modulator and 970nm LED
 - Design a custom LabView code to operate the system
 - Validate the imaging system in liquid intralipid phantoms

Project: Longitudinal preclinical monitoring of chemotherapy response using **SFDI** 2014-present

- Optics: - Develop a Monte Carlo based two-layer look-up-table inverse algorithm to simulate subcutaneous tumor
 - Optimize SFDI image acquisition, image processing and image analysis strategies using ImageJ and Matlab
 - Explore depth of light penetration, long-term system and user repeatability using Matlab
- Biomedical: - Image and monitor prostate xenograft tumor model in response to cytotoxic and antiangiogenic drugs
 - *Ex vivo* immunohistochemical staining for tumor cell death, proliferation, vasculature and immune response
 - Extensive statistical data analysis to correlate *in vivo* SFDI results to *ex vivo* immunohistochemical findings

Project: Monitoring neoadjuvant chemotherapy response in breast cancer patients using **DOSI** 2014-present

- Optics: - Institutional Review Board (IRB) protocol approval at Boston Medical Center
 - Imaged affected and normal breasts with DOSI imaging system in breast cancer patients

Project: Monitoring sarcoma patients using **DOSI** 2013-2014

- Optics: - Design and build a novel bendable DOSI optical imaging probe with fiber optics connected to LASERs and APD
 - Institutional Review Board (IRB) protocol approval for imaging sarcoma locations in normal volunteers

University of Dhaka, Dhaka, Bangladesh

2009-2012

Optics: - Design and modeling of InP, GaAs and InGaAs based 2D Photonic Crystal Waveguides using OPTI™ software
 - Assess waveguide sensitivity and accuracy for sensing biochemicals, i.e., HeLa cells

TEACHING EXPERIENCE

- Volunteer for City Lab as a recipient of ‘Cross-disciplinary Training in Nanotechnology for Cancer’ fellowship, Nanotechnology innovation center, Boston University 2014-2015
- Graduate Teaching Fellow, Department of ECE, Boston University 2012-2013
 1. Signals & Systems, 2. Electromagnetism, 3. Fundamentals of Nanomaterials and Nanotechnology

JOURNAL PUBLICATIONS (SELECTED)

- K. Karrobi, A. Tank, S. Tabassum, V. Pera, and D. Roblyer, “Diffuse and nonlinear imaging of multiscale vascular parameters for in vivo monitoring of preclinical mammary tumors,” Journal of Biophotonics, e201800379 (2019)
- S. Tabassum, V. Pera, G. Greening, T. J. Muldoon, D. Roblyer, “Two-layer inverse model for improved longitudinal preclinical tumor imaging in the spatial frequency domain,” J. of Biomedical Optics, 23(7), 076011 (2018)
- S. Tabassum, Y. Zhao, R. Istfan, J. Wu, D. J. Waxman, and D. Roblyer, “Feasibility of spatial frequency domain imaging (SFDI) for optically characterizing a preclinical oncology model,” Biomed. Optic. Express., 7(10), pp 4154-70 (2016)
- Y. Zhao, S. Tabassum, S. Piracha, M. S. Nandhu, M. Viapiano, D. Roblyer, “Angle correction for small animal tumor imaging with spatial frequency domain imaging (SFDI),” Biomed. Optic. Express., 7(6), pp 2373-2384 (2016)

CONFERENCE PUBLICATIONS/PRESENTATIONS (SELECTED)**Oral Presentations**

- S. Tabassum, “Exploring the relationships between optical and molecular biomarkers of cancer treatment response in the preclinical setting using Spatial Frequency Domain Imaging (SFDI),” 10856-10, SPIE Photonics West BIOS (2019)
- S. Tabassum, “Long-term longitudinal monitoring of chemotherapy response using Spatial Frequency Domain Imaging using an improved two-layer Monte Carlo based inverse model,” 10472-08, SPIE Photonics West BIOS (2018)

Poster Presentations

- S. Tabassum, R. Istfan, and D. Roblyer, “Longitudinal Monitoring of Therapy Response in a Preclinical Model using Spatial Frequency Domain Imaging,” Cancer Imaging and Therapy (OSA), Fort Lauderdale, Florida United States (2016)
- S. Tabassum, R. Istfan, and D. Roblyer, “Preclinical Monitoring of Chemotherapy Response with Spatial Frequency Domain Imaging (SFDI),” Laser in Medicine and Biology, Gordon Research Conference, New Jersey, USA (2014)

HONORS & AWARDS (SELECTED)

- Boston University Photonics Center travel grant for SPIE Photonics West BIOS conference 2019
- Best student paper runner up at SPIE Photonics West BIOS conference 2018
- BU ECE travel grant for attending Society of Women Engineers annual conference 2017
- ‘Cross-disciplinary Training in Nanotechnology for Cancer’ Fellowship, NCI & Boston University 2014-2015
- Distinction in Ph.D. qualifying examination, Boston University 2013
- ‘South Asian Physics Foundation’ travel grant for attending IWPSD workshop in India 2011

TUTORIAL/WORKSHOP ATTENDED (SELECTED)

- Short Course in Computational Biophotonics, UC Irvine, California 2016
- ‘Critical Issues in Tumor Microenvironment: Angiogenesis, Metastasis and immunology’ 29th annual workshop, Massachusetts General Hospital, Harvard Medical School 2014
- Nanomanufacturing and characterization workshops, Boston University 2014-2015

COMMUNICATION & LEADERSHIP ROLES

Communication roles: Review multiple peer-reviewed journals in collaboration with research adviser, interaction with breast cancer patients for research in Boston Medican Center, highly developed written skills for IRB protocols and student fellowship grants, strong interpersonal skills through presentations in international conferences

Leadership roles: Lab safety coordinator (2013-present), high school RISE intern supervision at BU (summer 2014), undergraduate students supervision (summer 2017, 2018), American Cancer Society Relay for Life at BU organizer